Universidade de Aveiro Departamento de Física
2013

Ana Luísa Monteiro da Silva

Desenvolvimento de detetores para imagiologia baseados em MPGDs e suas aplicações

MPGDs based radiation imaging devices and applications

Universidade de Aveiro Departamento de Física
2013

Ana Luísa Monteiro da Silva

Desenvolvimento de detetores para imagiologia baseados em MPGDs e suas aplicações

MPGDs based radiation imaging devices and applications

Universidade de Aveiro Departamento de Física
2013

Ana Luísa Monteiro da Silva

Desenvolvimento de detetores para imagiologia baseados em MPGDs e suas aplicações

MPGDs based radiation imaging devices and applications

Dissertação apresentada à Universidade de Aveiro para cumprimento dos requisitos necessários à obtenção do grau de Doutor em Física, realizada sob a orientação científica do Doutor João Filipe Calapez de Albuquerque Veloso, Professor Auxiliar do Departamento de Física da Universidade de Aveiro e co-orientação da Doutora Maria Luísa Carvalho Leonardo, Professora Associada da Faculdade de Ciências da Universidade de Lisboa.

Apoio financeiro da FCT (Bolsa de Doutoramento com a referência SFRH / BD / 61862 / 2009) e do FSE/FEDER no âmbito do QREN através dos programas COMPETE e Adl. Projecto CERN/FP/109283/2009 e PTDC/FIS/110925/2009.

Aos meus pais e ao meu irmão.
Aos meus avós.
Ao Samuel pelo carinho, compreensão e incansável apoio.

o júri / the jury

presidente / president

Prof. Doutor João Manuel Nunes Torrão
Professor Catedrático do Departamento de Línguas e Culturas da Universidade de Aveiro

vogais / examiners committee

Prof. Doutor Pedro Manuel Ferreira Amorim
Professor Auxiliar do Departamento de Física da Faculdade de Ciências da Universidade de Lisboa

Doutor Miguel Adrião Reis
Investigador Auxiliar do Instituto Tecnológico e Nuclear/Instituto Superior Técnico da Universidade Técnica de Lisboa

Prof. Doutor Armando José Trindade das Neves
Professor Associado do Departamento de Física da Universidade de Aveiro

Prof. Doutora Maria Luísa Leonardo de Carvalho
Professora Associada com Agregação do Departamento de Física da Faculdade de Ciências da Universidade de Lisboa

Prof. Doutor João Filipe Calapez de Albuquerque Veloso
Professor Auxiliar do Departamento de Física da Universidade de Aveiro

agradecimentos /
acknowledgements

"Caminhante, não há caminho. Faz-se o caminho ao andar..."

(António Machado)

Foi sempre assim que entendi a vida, a ciência e a investigação. Não são mais que projetos desenvolvidos a cada dia, a cada instante. O caminho, esse, não é para ser feito sozinho. Ao longo dos últimos quatro anos muitos foram aqueles que, de um modo ou de outro, contribuíram para o desenrolar deste trabalho. A todos eles o meu sincero Muito Obrigada!

- Em especial, agradeço ao Prof. Doutor João Veloso, orientador deste trabalho, toda a disponibilidade que sempre manifestou para comigo, bem como as valiosas sugestões e orientações científicas, que, com generosidade, sempre me deu. Também não posso deixar de agradecer a oportunidade de fazer parte da sua equipa de investigação, carinhosamente apelidada de DRIM *team*, e sublinhar a amizade com que sempre me presenteou.
- Agradeço também à Prof. Doutora Maria Luísa Carvalho pela coorientação deste trabalho, pela cedência de amostras e revisão dos trabalhos publicados, pelo apoio, disponibilidade e amizade que sempre demonstrou para comigo.
- Ao Centro de Física Atómica da Universidade de Lisboa, em especial à Prof. Doutora Maria Isabel Cabaço pela cedência do tubo de raios X PW1830 da Philips, o qual se mostrou muito útil na realização das análises. Agradeço ao Prof. Doutor Koen Janssens da Universidade de Antuérpia, Bélgica, a gentil cedência da amostra correspondente a um Manuscrito Iluminado do século XV-XVI, para análise com os sistemas desenvolvidos.
- Ao Sr. Miguel Rocha e Sr. Ivo Mateus pela dedicação na produção de peças na oficina, necessárias ao desenvolvimento do trabalho. Agradeço também ao Sr. Júlio Gonçalves as soluções ao nível da eletrónica, muito importantes no decorrer do mesmo.
- Os maiores agradecimentos aos membros da DRIM *team* pelo fantástico ambiente de trabalho, entreajuda, companheirismo nos momentos científicos e de convívio. À Andrêa, ao Arouca (Carlos Azevedo), ao Cacia (Carlos Oliveira), ao Carlitos, ao Daniel, ao Fábio, ao Hugo, à Lara, ao Lipe, ao Luís Moutinho, ao Pedro e ao Tiago.
- Especial agradecimento ao Doutor Carlos Azevedo pela partilha de conhecimento, colaboração e realização das simulações que vieram completar este trabalho, bem como a revisão da dissertação. Ao Doutor Carlos Oliveira pela disponibilidade constante (mesmo estando fora), pela preciosa ajuda na revisão científica da tese. Ao Lipe, Stella, Manel e Margarida pela revisão linguística do documento.
- Ao Samuel, pela força e compreensão nos momentos menos bons. Pelo carinho, pelo abraço forte e pelo sorriso amigo, mesmo quando não pude estar presente.
- Agradeço aos meus Amigos o carinho e apoio em todos os momentos. Aos meus pais e família, porque sempre acreditaram (mesmo mais que eu) em mim!

palavras-chave

Imagiologia por fluorescência de raios X de energia dispersiva; Distribuição espacial de elementos químicos; detetores gasosos baseados em microestruturas

resumo

Este trabalho descreve o desenvolvimento e aplicação de sistemas baseados em detetores gasosos microestruturados, para imagiologia de fluorescência de raios-X por dispersão em energia (EDXRF).

A técnica de imagiologia por fluorescência de raios-X assume-se como uma técnica poderosa, não-destrutiva, em análises da distribuição espacial de elementos em materiais.

Os sistemas para imagiologia de EDXRF desenvolvidos são constituídos por: um tubo de raios-X, usado para excitar os elementos da amostra; um detetor gasoso microestruturado; e uma lente *pinhole* que foca a radiação de fluorescência no plano do detetor formando assim a imagem e permitindo a sua ampliação. Por outro lado é estudada a influência do diâmetro da abertura do *pinhole* bem como do fator de ampliação obtido para a imagem, na resolução em posição do sistema.

Foram usados dois conceitos diferentes de detetores gasosos microestruturados. O primeiro, baseado na microestrutura designada por 2D-*Micro-Hole* $\&$ *Strip Plate* (2D-MHSP) com uma área ativa de 3×3 cm^2, enquanto que o segundo, baseado na estrutura 2D-*Thick-COBRA* (2D-THCOBRA) apresenta uma área ativa de deteção de 10×10 cm^2.

Estes detetores de raios-X de baixo custo têm a particularidade de funcionar em regime de fotão único permitindo a determinação da energia e posição de interação de cada fotão que chega ao detetor. Deste modo permitem detetar a energia dos fotões X de fluorescência, bem como obter imagens 2D da distribuição desses fotões X para o intervalo de energias desejado. São por isso adequados a aplicações de imagiologia de EDXRF.

Os detetores desenvolvidos mostraram resoluções em energia de 17% e 22% para fotões incidentes com uma energia de 5.9 keV, respectivamente para o detetor 2D-MHSP e 2D-THCOBRA e resoluções em posição adequadas para um vasto número de aplicações.

Ao longo deste trabalho é detalhado o desenvolvimento, o estudo das características e do desempenho de cada um dos detetores, e sua influência na performance final de cada sistema proposto. Numa fase mais avançada apresentam-se os resultados correspondentes à aplicação dos dois sistemas a diversas amostras, incluindo algumas do nosso património cultural e também uma amostra biológica.

keywords

Energy dispersive X-ray fluorescence imaging; Elemental spatial distribution; Micropattern Gaseous Detectors

abstract

The present document describes the development and application of two energy dispersive X-ray fluorescence (EDXRF) imaging systems based on micropattern gaseous detectors.

The X-ray fluorescence imaging technique is assumed as a powerful technique, non-destructive, on analysis of the spatial distribution of elements in materials.

The imaging systems developed for EDXRF imaging consist of: an X-ray tube, acting as the external source to excite the sample; a micropattern gas detector; and a pinhole which directs the fluorescence radiation to the detector. On the other hand, the influence of the pinhole aperture diameter and the magnification factor obtained for the image in the position resolution of the system, is studied.

Two different concepts of micropattern gaseous detectors were used. The first one is based on the 2D Micro-Hole $\&$ Strip Plate (2D-MHSP) microstructure with an active area of 3×3 cm^2, while the second is based on the 2D Thick-COBRA (2D-THCOBRA) with a sensitive detection area of about 10×10 cm^2. These X-ray detectors are single photon counting detectors, allowing the determination of the interaction position and energy of each photon reaching the detector. Therefore they can work as low cost energy dispersive detectors as well as obtain 2D images of the distribution of X photons for a range of energies required, which makes them suitable for EDXRF imaging applications.

The detectors have shown an energy resolution of about 17% and 22% for 5.9 keV X-ray photons, for the 2D-MHSP detector and 2D THCOBRA, respectively, and apropriate spatial resolutions for a wide range of applications.

Throughout this work, the development and study of the characteristics and the performance of each of the detectors used as well as their influence in the final performance of each proposed system is shown in detail.

Results concerning the application of the two systems to several samples, including some cultural heritage samples and also a biological sample are shown.

PUBLICATIONS AND COMMUNICATIONS IN THE CONTEXT OF THIS THESIS

The work done under this doctoral program resulted in several publications in referred scientific journals and presentations at international conferences.

Publications

Papers in international scientific periodicals with referees

- J.F.C.A. Veloso, **A.L.M. Silva**, C. Oliveira, A.L. Gouvêa, C.D.R. Azevedo, L. Carramate, H. Natal da Luz and J.M.F. dos Santos;
  "Energy resolved X-ray fluorescence imaging based on a micropattern gas detector".
  Spectrochimica Acta B, vol. 65, pp. 241-247, 2010.
  DOI: 10.1016/j.sab.2010.03.006

- **A.L.M. Silva**, J.F.C.A. Veloso, C.A.B. Oliveira, A.L. Gouvêa, J.M.F. dos Santos and M.L. Carvalho;
  "EDXRF imaging of Pb in glazed ceramics using a micropattern gas detector".
  Analytical and Bioanalytical Chemistry, vol. 395, pp. 2073-2080, 2009.
  DOI: 10.1007/s00216-009-3196-8

- C.A.B. Oliveira, C.A. Santos, **A.L.M. Silva**, J.M.F. Dos Santos, J.F.C.A. Veloso;
  "Energy Weighting in a 2D-MHSP X-ray Single Photon Detector".
  IEEE Transactions on Nuclear Science, vol. 57, pp. 938-943, 2009.
  DOI: 10.1109/TNS.2010.2044806

- L.F.N.D. Carramate, C.A.B. Oliveira, **A.L.M. Silva**, A.M. da Silva, J.M.F. dos Santos, and J.F.C.A. Veloso;

"Energy Weighting Technique in Quantum Computed Tomography using a MPGD".
JINST, vol.6, pp C02002, 2011. DOI: 10.1088/1748-0221/6/02/C02002

- **A.L.M. Silva**, C.D.R. Azevedo, C.A.B. Oliveira, J.M.F. Dos Santos, M.L. Carvalho, J.F.C.A. Veloso;
  "Characterization of an energy dispersive X-ray fluorescence imaging system based on a Micropattern Gaseous Detector".
  Spectrochimica Acta B, vol. 66, pp. 308-313, 2010.
  DOI:10.1016/j.sab.2011.03.002

- **A.L.M. Silva**, R. Figueroa, A. Jaramillo, M.L. Carvalho and J.F.C.A. Veloso;
  "Performance of a gaseous detector based Energy Dispersive X-Ray Fluorescence imaging system: analysis of human teeth treated with dental amalgam".
  In press, Spectrochimica Acta B, 2013.
  DOI: 10.1016/j.sab.2013.03.005

- **A.L.M. Silva**, C.D.R. Azevedo, L.F.N.D. Carramate, T. Lopes, R. de Oliveira, J.F.C.A. Veloso;
  "X-ray Imaging Detector Based on a 2D Sensitive THCOBRA with Resistive Line".
  JINST, vol.8 pp. P05016, 2013.
  DOI: 10.1088/1748-0221/8/05/P05016

- R.G. Figueroa, E. Lozano, F. Belmar, D. Alcaman, A. von Bohlen, C.A.B. Oliveira, **A.L.M. Silva** and J.F.C.A. Veloso;
  "Characteristics of low cost and portable large area XRF imaging system".
  Submitted to X-ray Spectrometry.

Papers in conference proceedings with referees

- C.A.B. Oliveira, C.A. Santos, **A.L.M. Silva**, J.M.F. Dos Santos, J.F.C.A. Veloso;
  "Energy Weighting in a 2D-MHSP X-ray Single Photon Detector".
  IEEE Nuclear Science Symposium / Medical Imaging Conference Record, pp. 3986-3990,
  October 19-25, 2008.
  DOI: 0.1109/TNS.2010.2044806

- A.L. Gouvêa, H. Natal da Luz, C.A. Santos, C.A.B. Oliveira, **A.L.M. Silva**, C.D.R. Azevedo, J.M.F. dos Santos, J.F.C.A. Veloso;
  "Quantum X-Ray Imaging with the 2D - Micro Hole and Strip Plate".
  World Congress on Medical Physics and Biomedical Engineering, IFMBE Proceedings 25/II, pp. 890-893, 2009.
  DOI: 10.1007/978-3-642-03879-2_249

- **A.L.M. Silva**, C.D.R. Azevedo, L.F.N.D. Carramate, T. Lopes, R. de Oliveira, J.F.C. Veloso;
  "X-ray imaging detector based on a 2D sensitive THCOBRA".
  IEEE Nuclear Science Symposium / Medical Imaging Conference Record, 2012.

Comunications

Invited Talks

- **A.L.M. Silva**, C.D.R. Azevedo, L.F.N.D. Carramate and J.F.C.A. Veloso;
  "EDXRF imaging with new gaseous detectors: examples of qualitative analysis".
  To be presented on IBER2013,XII Iberian Meeting on Atomic and Molecular Physics, 9-11 September, Seville, Spain.

Oral Communications

- J.F.C.A. Veloso, **A.L.M. Silva**, C.A.B. Oliveira, A. Gouvêa, H. Natal da Luz and J.M.F. dos Santos;
  "Energy Resolved X-ray fluorescence imaging based on a micropattern gas detector".
  IEEE Nuclear Science Symposium and Medical Imaging, Special focus Workshop on X-Ray Micro Imaging of Materials, Devices, and Organisms, October 19-25 2008, Dresden, Germany.

- **A.L.M. Silva**, J.F.C.A. Veloso, C.A.B. Oliveira, A.L. Gouvêa, J.M.F. dos Santos and M.L.Carvalho;
  "EDXF imaging of Pb depth penetration in glazed ceramics using a micropattern gas detector".
  TECHNART 2009 - Non-destructive and Microanalytical Techniques in Art and Cultural Heritage, April 27-30 2009, Athens, Greece.

- A.L. Gouvêa , H Natal da Luz, C.A. Santos, C.A.B. Oliveira, **A.L.M. Silva**, C.D.R. Azevedo, J.M.F. dos Santos and J.F.C.A. Veloso;
  "Quantum X-ray imaging with the 2D-Micro Hole and Strip Plate".
  World Congress 2009 on Medical Physics and Biomedical Engineering, 7-12 of September, 2009, Munich, Germany.

- **A.L.M. Silva**, C.D.R. Azevedo, C.A.B. Oliveira, J.M.F. Dos Santos, J.F.C.A. Veloso;
  "Characterization of an EDXRF imaging system based on a MPGD".
  European Conference on X-Ray Spectrometry, 20-25 June 2010, Figueira da Foz, Coimbra, Portugal.

- L.F.N.D. Carramate, C.A.B. Oliveira, **A.L.M. Silva**, A.M. da Silva, J.M.F. dos Santos, J.F.C.A. Veloso;
  "Energy Weighting Technique in Quantum Computed Tomography using a MPGD".
  12th International Workshops on Radiation Imaging Detectors, 11-15 July, 2010. Cambridge, United Kingdom.

- **A.L.M. Silva**, C.D.R. Azevedo, C.A.B. Oliveira, J.M.F. Dos Santos, M.L. Carvalho and J.F.C.A. Veloso;
  "EDXRF imaging system based on a MPGD: characterization and applications".
  11th Rio Symposium on Atomic Spectrometry, 24-29 October, 2010, Mar del Plata, Argentina.

- **A.L.M. Silva**, C.D.R. Azevedo, C.A.B. Oliveira, J.M.F. Dos Santos, M.L. Carvalho and J.F.C.A. Veloso;
  "EDXRF imaging analysis with a gaseous detector".
  Colloquium Spectroscopicum Internationale XXXVII, 28 August - 2 September, 2011, Buzios, Brazil.

- **A.L.M. Silva**, C.D.R. Azevedo, C.A.B. Oliveira, J.M.F. Dos Santos, M.L. Carvalho and J.F.C.A. Veloso;
  "Performance of a gas counter based EDXRF imaging system in the analysis of different sample types".
  IMA 2011-Instrumental Methods of Analysis-Modern Trends and Applications conference, 18-22 September 2011, Chania, Crete, Greece.

- **A.L.M. Silva**, M.L. Carvalho, J.F.C.A. Veloso;
  "Elemental imaging analysis with a full-field Micropattern Gaseous Detector".
  European Conference on X-Ray Spectrometry, 18-22 June 2012, Vienna, Austria

- **A.L.M. Silva**, M.L. Carvalho and J.F.C.A. Veloso;
  "Elemental distribution in biological and art heritage samples by using an imaging gaseous detector based system".
  Denver X-ray Conference, 6-10 August 2012, Denver, Colorado, USA

- J.F.C.A. Veloso, **A.L.M. Silva**, R. Figueroa, A. Jaramillo, and M.L. Carvalho; *"New generation of gaseous detectors for EDXRF imaging: elemental distribution in biological and heritage samples".*
  12th Rio Symposium on Atomic Spectrometry, 17-21 September, 2012, Foz do Iguaçu, Brasil.

- L.F.N.D. Carramate; **A.L.M Silva**, A.M. da Silva and J.F.C.A. Veloso;
  "CT System With Energy Resolving Capability Using A THCOBRA Based Detector".

IWORID 2013 - International Workshops on Radiation Imaging Detectors,Paris, France, 23-27 June 2013

- **A.L.M. Silva**, M.L. Carvalho, J.M.F. dos Santos, J.F.C.A. Veloso;
  "Further developments of an energy- and position-sensitive XRF imaging system based on a THCOBRA detector".
  CSI 2013 - XXXVIII Colloquium Spectroscopicum Internationalein Troms, Norway, June 16 - 20, 2013

- J.F.C.A. Veloso, **A.L.M. Silva**, C.D.R. Azevedo, L. Carramate, R. de Oliveira;
  "The μDot-THCOBRA: a new gaseous electron multiplier concept".
  MPGD 2013 - 3rd Conference on Micro-Pattern Gaseous Detectors, Zaragoza, Spain, July 1-4, 2013.

- **A.L.M.Silva**, C.D.R. Azevedo, L.F.N.D. Carramate, T. Lopes, J.F.C. Veloso;
  "Further studies on the position-sensitive THCOBRA for imaging purposes".
  RD51 Collaboration meeting on July 5-6 , Zaragoza, Spain, 2013.

Poster Communications

- A.L. Gouvêa, H. Natal da Luz, C.A. Santos, C.A.B. Oliveira, **A.L.M. Silva**, C.D.R. Azevedo, J.M.F. dos Santos and J.F.C.A. Veloso.
  "Quantum X-ray imaging with the 2D - Micro Hole and Strip Plate".
  World Congress 2009 on Medical Physics and Biomedical Engineering, Munich, Germany, 7-12 of September, 2009

- R.G. Figueroa, C. Parra, **A.L.M. Silva**, J.F.C.A. Veloso;
  "Experimental study of an optical XRF imaging system using a 2D gaseous detector".
  European Conference on X-Ray Spectrometry, Figueira da Foz, Coimbra, Portugal, 20-25 June 2010

- C.E. Bottaini, **A.L.M. Silva**, D.S. Covita, J.F.C.A. Veloso;
  "EDXRF analysis of archaeological metal artefacts from the Bronze Age" . European Conference on X-Ray Spectrometry, 20-25 June, 2010, Figueira da Foz, Coimbra, Portugal.

- C.E. Bottaini, **A.L.M. Silva**, D.S. Covita, J.F.C.A. Veloso;
  "Elemental studies of archaeological metal artefacts from the Bronze Age based on EDXRF analysis".
  11th Rio Symposium on Atomic Spectrometry, 24-29 October, 2010, Mar del Plata, Argentina

- **A.L.M. Silva**, C.D.R. Azevedo, C.A.B. Oliveira, J.M.F. Dos Santos, M.L. Carvalho and J.F.C.A. Veloso;
  "Characterization and applications of an EDXRF imaging system based on a MPGD".
  XVII Simposio Chileno de Física, 10-12 November 2010, Púcon, Chile

- **A.L.M. Silva**, C.D.R. Azevedo, L.F.N.D. Carramate, T. Lopes, R. de Oliveira and J.F.C.A. Veloso;
  "X-ray imaging detector based on a 2D sensitive THCOBRA with resistive line readout".
  IEEE Nuclear Science Symposium and Medical Imaging Conference 2012, October 29 - November 3, 2012, Anaheim, CA, EUA.

- R.G. Figueroa, E. Lozanoa , F. Belmar, D. Alcaman, A. von Bohlen, C.A.B. Oliveira, **A.L.M. Silva**, J. F.C.A. Veloso;
  "Characteristics of low cost and portable large area XRF imaging system".
  12th Rio Symposium on Atomic Spectrometry, 17-21 September, 2012, Foz do Iguaçu, Brasil.

- **A.L.M. Silva**, M.L. Carvalho, J.F.C.A. Veloso;
  "Full-Field large area XRF system based on a gaseous detector for elemental analysis in cultural heritage samples"
  Accepted for presentation at Technart 2013, Amsterdam, Netherlands, 23-27 September 2013

- T. Lopes, C.D.R. Azevedo, **A.L.M. Silva**, D.S. Covita, F.A. Pereira, C.A. Santos, J.F.C.A. Veloso;
  "VUV sensitive gaseous photomultiplier with position capability based on thick multipliers".
  MPGD 2013 - 3rd Conference on Micro-Pattern Gaseous Detectors, Zaragoza, Spain, July 1-4, 2013.

- **A.L.M.Silva**, C.D.R. Azevedo, L. Carramate, T. Lopes, J.F.C. Veloso;
  "Further studies on the position-sensitive THCOBRA for imaging purposes".
  MPGD 2013 - 3rd Conference on Micro-Pattern Gaseous Detectors, Zaragoza, Spain, July 1-4, 2013.

Other Communications

- J.F.C.A. Veloso, C.D.R. Azevedo, C.A.B. Oliveira, **A.L.M. Silva**, L.F.N.D. Carramate, C.A. Santos, I.F. Castro, H. Natal da Luz, D.S. Covita, A.L.F. Ferreira, F.A. Pereira, L.M. Moutinho, P. Correia, C. Amorim;

"X-ray and γ-ray imaging detectors based on microstructures".
Physics for Health Summer School, 26-28 July 2010, Covilhã, Portugal

- **A.L.M.Silva**;
  "EDXRF imaging system based on a MPGD:characterization and applications".
  MAP-fis Conference, 2011, Porto, Portugal

- **A.L.M. Silva**;
  "Elemental distribution of metals in biological and art heritage samples using a gaseous detector based system".
  Workshop Heavy Metals, from the environment to man, 12th December 2011, Lisbon, Portugal

- **A.L.M. Silva**;
  "X-ray imaging detector based on a 2D sensitive THCOBRA with resistive line readout".
  MAP-fis Conference, 2013, Aveiro, Portugal

CONTENTS

LIST OF ABBREVIATIONS AND SYMBOLS

IUPAC	International Union of Pure and Applied Chemistry
EDXRF	Energy Dispersive X-Ray Fluorescence
ER-XRF	Energy resolved X-Ray fluorescence
XRF	X-ray fluorescence
μXRF	Micro X-Ray fluorescence
FF-XRF	Full-Field X-Ray Fluorescence
CCD	Charge Coupled Device
PCB	Printed Circuit Board
MPGD	Micropattern Gas Detector
GPC	Gas Proportional Counter
MWPC	Multiwire Proportional Chamber
MSGC	Micro-Strip Gas Chamber
MSP	Micro-Strip Plate
GEM	Gas Electron Multiplier
MHSP	Micro-Hole & Strip Plate
THGEM	Thick-Gas Electron Multiplier
THCOBRA	Thick-COBRA
FWHM	Full Width at Half Maximum
ROI	Region of Interest
SNR	Signal-to-Noise Ratio
PSF	Point Spread Function
LSF	Line Spread Function
ESF	Edge Spread Function
MTF	Modular Transfer Function

LIST OF FIGURES

LIST OF TABLES

INTRODUCTION

In the last century several major inventions in the field of gaseous detectors were introduced. We can mention the Geiger-Müller Counter, the Gas Proportional Counter and the Multiwire Proportional Chamber (MWPC), with the last one combining gas multiplication with position resolution.

During the R&D of gaseous detectors, there have always been many small scale efforts in the development of detectors with higher granularity. The use of microelectronic techniques for the manufacturing of gaseous detectors, like printing circuit board techniques (PCB), made possible the development of a new generation of gaseous detectors with very small amplification cells: the Micropttterned Gas Detectors (MPGDs).

This important breakthrough, allowed the development of gaseous detectors with very good spatial resolution, high-rate capability and large sensitive area. A large number of research groups all over the world are developing MPGDs for future experiments at particle accelerators, for experiments in nuclear, astroparticle and high energy physics, as well as for industrial applications such as medical imaging and material science.

The Micro-Hole & Strip Plate (MHSP) is a MPGD with high performance in terms of gain and high rate capability. It consists of a hybrid microstructure that combines in a single element two different MPGD patterns, the Gas Electron Multiplier (GEM) and the Micro-Strip Plate (MSP), presenting two charge multiplication stages and thus, achieving higher gains, when compared to other MPGDs concepts.

In applications requiring larger areas with adequate spatial resolutions, more coarse micro-patterned detectors, e.g. Thick-COBRA (THCOBRA) device, could offer an interesting and economic solution. The THCOBRA can be considered as a thick-version of the MHSP, where features of the Thick-Gas Electron Multiplier (THGEM) and of the MHSP are combined.

The MHSP and THCOBRA detectors have an intrinsic imaging capability and can be used as position sensitive detectors by using a very simple readout system based on resistive

lines, in a 2D-MHSP and 2D-THCOBRA concept, respectively. Together with the accurately determination of the interaction position of each X-ray photon in the sensitive area of the detector, they carried also the information about the energy of the incoming radiation.

Energy resolved X-Ray fluorescence (ER-XRF) imaging technique requires collection of elemental and spatial-resolved information in a non-destructive way of the constituents of a variety of materials. Thus, due to the excellent properties for single photon counting with intrinsic imaging capability combined with the energy information of each event, of the 2D-MHSP and the 2D-THCOBRA detectors, it is possible to say that they offer unique characteristics and are very promising devices for ER-XRF imaging applications.

The experiments described in this work were made aiming the development of two systems to be used for ER-XRF imaging applications. They are based on the two different position sensitive MPGD concepts mentioned before, the 2D-MHSP and the 2D-THCOBRA. These systems present good position and energy resolution, and sensitive areas of about 2.8×2.8 cm^2 and 10×10 cm^2, respectively.

Elemental imaging can be used in geology, cultural heritage, art history and biomedical, among other fields of science. The Full-Field X-Ray Fluorescence (FF-XRF) systems proposed in this work can be used to examine larger samples, with a reasonable resolution, since they allow to obtain elemental map distributions of samples surface by combining image and energy information.

The present document is divided in five chapters and organized as follows:

The first chapter aims to introduce the physical concepts and principles associated with Energy Dispersive X-Ray Fluorescence (EDXRF) technique. The short background review is an introduction to the technique allowing any reader to better understand the work presented here. The first section concerns to the interaction of the X- radiation with matter, together with a number of other concepts crucial to the understanding of the work. Secondly a historical review, including the State of the Art of EDXRF imaging systems, is presented.

Second chapter is concerned to the gas ionization chambers. It sketches the characteristics of X-ray detection with these devices, together with some basic topics on this field. An outlook of the past and present of the gas filled detectors for X-ray detection is also presented.

The EDXRF imaging systems developed are composed by three main components: the X-ray tube, the energy and position sensitive detector and a pinhole camera. To better understand the overall system performance, we found to be important to describe in detail, in the chapter 3, the operation principle characteristics of the gaseous detectors used in the proposed systems. In fact they are the major novelty in this kind of systems for EDXRF imaging applications. For that reason, studies concerning their detection efficiency for the energy range used, gain, intrinsic energy and spatial resolution are shown.

In what regards to the pinhole camera, a discussion about it influence on the system performance in terms of spatial resolution is presented in the second section of the chapter

3. In these studies known samples were used which were very useful to validate the system results. The first elemental map distribution images obtained with the systems are shown.

The first applications and results of both the proposed systems, are presented in the fourth chapter. The chapter is divided in three sections. Section 4.1 and 4.2 describe first the systems as a whole as well as their components alignment/geometry therein. Then, applications and results obtained with each system are presented. Applications in samples of two different fields of science were held. The first relates to the field of cultural heritage. Analysis of a Portuguese glazed tile from the XVII century were performed using the EDXRF system based on the MHSP detector. An illuminated parchment, from the 15th-16th century, was analysed using the system based on the THCOBRA detector. The EDXRF imaging system based on the MHSP was also used to analyse human teeth treated with metallic amalgam, in a biomedical application.

Section 4.3 aims to provide a discussion of the advantages/disadvantages of one system relative to the other and of both developed systems compared to those existing for the same purposes.

In the chapter 5, the general conclusions, showing the most relevant results achieved during this work, and the future work to be done in the sequence of this work, are presented.

CHAPTER 1

ENERGY DISPERSIVE X-RAY FLUORESCENCE ANALYSIS

The potential use of X-rays for qualitative and quantitative elemental assay is well appreciated since their discovery.

Energy Dispersive X-ray Fluorescence (EDXRF) analysis has strongly assumed a place among instrumental analytical methods, showing a phenomenal development and application, during the last decades. The method is based on the fact that the X-rays emitted from an ionized atom have characteristic energies, acting like a fingerprint of the elements involved in the study. The resulting X-ray intensity is proportional both to the elemental concentration and to the strength of the ionizing source.

X-ray fluorescence can be induced using either X-rays (produced by an X-ray tube or by synchrotron radiation), γ-rays (radioisotope source) or charged particles (e.g. electrons, protons, α-particles) with sufficient energy to induce ionization of inner shell electrons during collisions.

EDXRF analysis is a analytical technique that allows the determination of the multi-elements present in a given sample. In addition, the analysis is, in principle, non-destructive, has high precision and accuracy, requires short irradiation time and the associated costs are low. The technique is extremely versatile for applications in many fields of science, research and industry.

This chapter deals with the X-ray physics behind EDXRF analysis. Topics as X-ray absorption, characteristic X-ray spectra, Auger effect and fluorescent yields are discussed. A general description of the X-ray sources and applications for this kind of analysis method is also presented.

1.1 Physical fundamentals

The aim of this section is introducing several properties of X-rays that are considered relevant for the development and interpretation of this work. However, it is not intended covering all the physical concepts associated with X-ray spectrometry, but only those with particular significance in EDXRF analysis.

1.1.1 X-ray absorption

When a monochromatic and perfectly collinear X-ray beam of intensity I_0 passes through a homogeneous absorber medium of thickness x, is attenuated by a certain amount which depends mainly on the thickness (x), and density (ρ) of the absorbing medium [1–3]. The emergent beam will have an intensity I, which is always less than I_0, since part of the incident X-rays suffer attenuation or absorption by passing through matter.

The emerging intensity follows the Beer-Lambert law (Eq. 1.1) and can be written as follows:

$$I = I_0 \exp(-\mu_x x) \tag{1.1}$$

The coefficient μ_x is called the linear absorption coefficient yielding the energy absorption per unit of thickness, and is expressed in cm^{-1}. However, it is common to use the mass absorption coefficient μ_m, which is, sometimes, also called total cross-section for X-ray absorption at a specific energy E [4], and is related with the linear absorption coefficient by $\mu_m = \frac{\mu_x}{\rho}$. It units are expressed in cm^2/g. Thus, μ_m is a characteristic of the material, a property of each element and dependent of the incident X-ray energy. Equation 1.1 may be rewritten in terms of μ_m, as follows:

$$I = I_0 \exp(-\mu_m \rho x) \tag{1.2}$$

The exponential decrease of the beam intensity as it passes through the matter, is mainly due to three different phenomena: photoelectric absorption, scattering processes and pair-production (Figure 1.1).

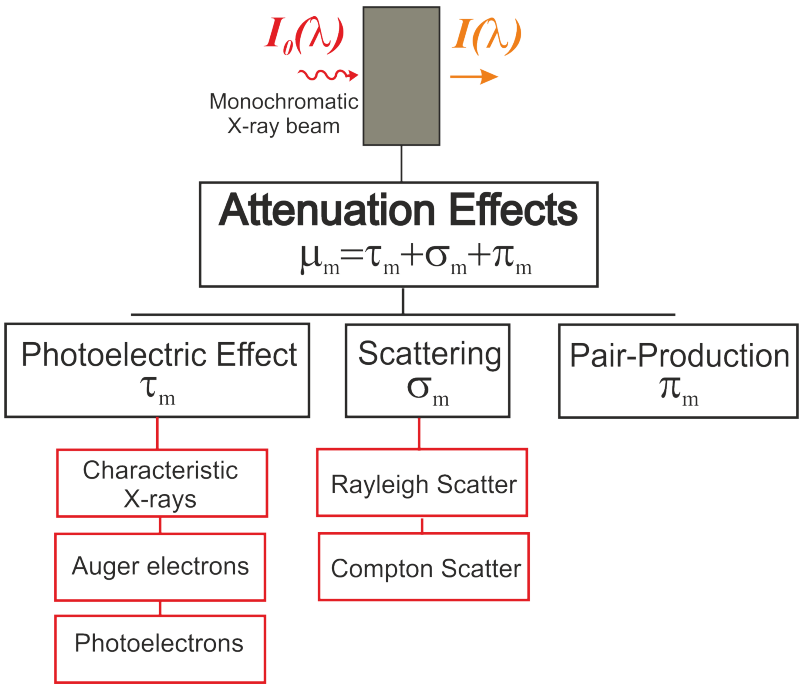

Figure 1.1: Illustrative scheme of the absorption processes occurring at the interaction of X-rays with matter.

In photoelectric absorption, the energy of the X-ray photon is completely absorbed as it

ejects a tightly bound electron from one of the inner shells atoms. The photon's excess of energy, i.e., the amount of energy superior to the binding energy, is transferred to the ejected electron as kinetic energy [1, 4]. This process will be discussed in detail in sections 1.1.2 and 1.1.3.

In the scattering process, photons are deviated from their original path, changing its direction. If the energy of the photon is maintained after the scattering, the process is considered elastic and is called Rayleigh scattering. Alternatively, if during the collision the photon loses some of its energy, then the process is called Compton or inelastic scattering. Compton scattering occurs when the incoming X-ray photon transfers a portion of its energy to an electron, known as recoil electron. The incident X-ray photon is deflected from its original path and loses energy because of the interaction, nevertheless it continues travelling through the material [5].

Pair-production can occur when the photon energy exceeds twice the rest mass of an electron (1.02 MeV/c^2), enabling the production of an electron-positron pair.

The total mass attenuation coefficient for X-ray absorption can be written as the sum of three components as a result of the three referred separate phenomena.

$$\mu_m = \tau_m + \sigma_m + \pi_m \tag{1.3}$$

Where τ_m is the total photoelectric attenuation coefficient, σ_m the total scattering attenuation coefficient, which includes both Rayleigh and Compton scattering, and π_m the pair-production attenuation coefficient.

Figure 1.2 shows the mass attenuation coefficient for xenon (Xe) and a gas mixture of neon and methane (Ne/5%CH_4), which are the gases used during this work. At higher energies, scattering and pair production effects dominate the interactions. However, at lower energies, these effects are very small compared to the photoelectric absorption, thus less significant bellow 100 keV [2, 7]. Since both Compton scattering and pair production become relevant only for energies much above those used in the current work, they will no longer be discussed in this work. Considering the total attenuation coefficient, photons with higher energies are less absorbed in the gases than lower energy photons, a fact that played an important role on the detection efficiency considerations taken into account during the development of the detectors used in this work. It is also important to notice that for xenon, in the low energy region, there are some discontinuities in the absorption curve. These discontinuities, usually called absorption edges, appear for binding energies of electrons in the various shells of the absorber atom. For an X-ray energy slightly above the edge, the photon energy is sufficient high to ionize a new shell and hence the attenuation increases abruptly [7]. In the case of the Ne mixture, these discontinuities are not visible because the K-absorption edge, the edge

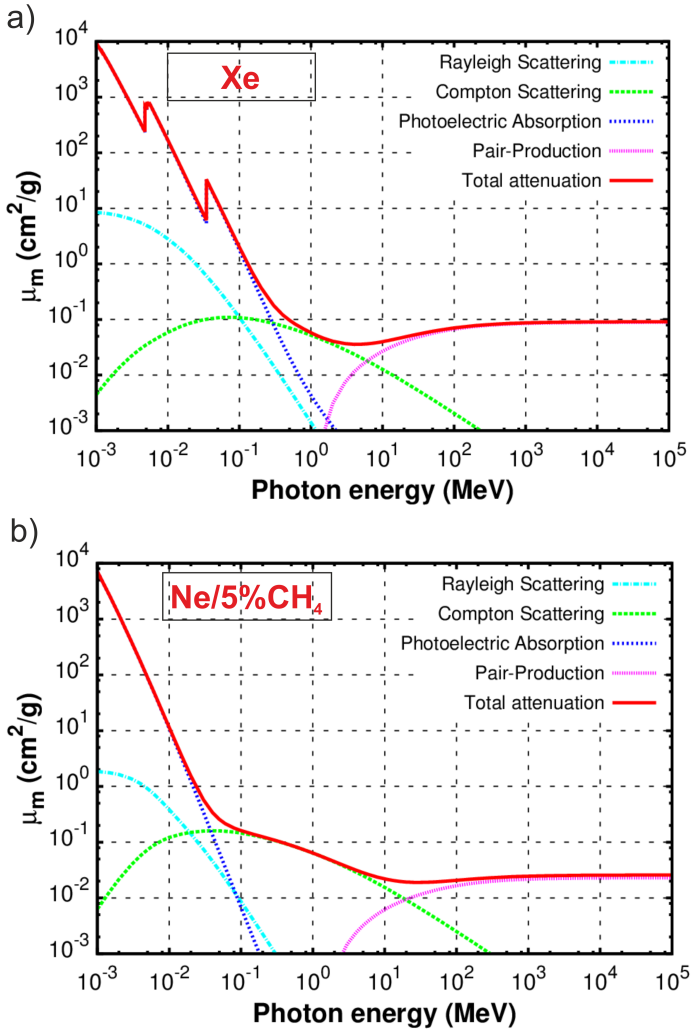

Figure 1.2: Typical X-ray absorption curves for a) Xe and b) Ne/5%CH_4. The total mass absorption coefficient and its components (photoelectric absorption; scattering (Rayleigh and Compton) and pair-production cross-sections) are shown, as a function of the incident photon energy for each gas [6].

with higher energy, corresponding to the K-shell electrons happens for X-ray energies of 866 eV and the data plotted in Figure 1.2 uses X-ray energies only above 1 keV [8]. Furthermore, energies in the order of hundreds of eV are not very important in the context of this work, since we will use only energies from a few keVs to about 30 keV.

1.1.2 Characteristic radiation production

Charles G. Barkla is credited with the discovery of characteristic X-rays, being awarded in 1917 with the Nobel Prize in Physics for his discovery [9].

In principle, any high energy photon can act as a characteristic X-ray source.

The characteristic radiation production starts with the photoelectric effect. By this process, a photon is absorbed by an atom, and an electron is ejected from an inner shell of the element. The incident photon needs to be sufficiently energetic to overcome the binding energy of the electron, ϕ, in the shell. The remaining energy is transferred to the electron in the form of kinetic energy [8, 10].

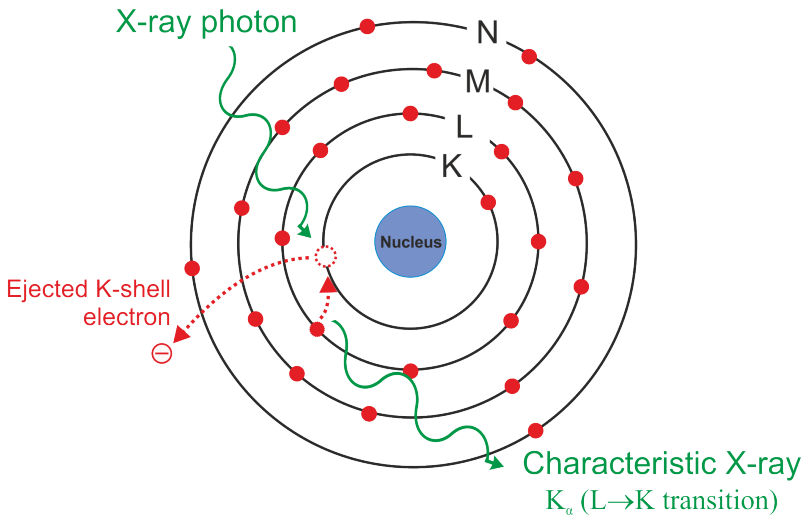

Figure 1.3: Characteristic radiation production examples. In the photoelectric interaction, the photon is absorbed by a K-shell electron binding energy. The K-shell vacancy is filled by an L-shell electron and the difference in binding energies is given as a characteristic photon (K_α).

The binding energy is an important concept in the context of EDXRF analysis and is usually denoted according to the different shells (K, L, M,...) and subshells (L(I), L(II), L(III), M(I), M(II), etc) of the atom by using subscripts, such as: ϕ_M, ϕ_L, $\phi_{L(III)}$. It is also identified as the absorption edge energy, the energy at which the mass absorption coefficient changes abruptly [3], as referred in section 1.1.1. On the other hand, the binding energy is known as the critical excitation potential, because ϕ in keV corresponds to the minimum energy (voltage, in kV, in the case of the X-ray tube), required to remove the electron from its shell and leaving the atom in an excited state[3].

After the photoelectric interaction, the atom is in a highly excited state due to the vacancy left in one of its electron orbitals. The atom tends to return immediately to a stable configuration by filling the vacancy with an outer electron shell. The transition originates the emission of an X-ray with energy equal to the difference between the initial and final states of the electron. Figure 1.3 illustrates the K_α X-ray production from a transition of an electron from the L to the K-shell. This process will continue with the hole created in the L-shell being filled by a M or higher shell electron with the emission of an L-line of energy (E_L-E_M).

The process ends only when the energy of the atom is lowered to a value corresponding to a stable configuration (ground state).

The K_α fluorescence of an element is also related with the probability that a K-shell electron will be ejected rather than an L- or M-shell electron. This probability is given by a quantity called K-shell absorption jump ratio J_K[10]:

$$J_K = (r_K - 1)/r_K \tag{1.4}$$

Here, r_K is the K-shell absorption jump, which is defined as the ratio of the photoelectric mass absorption coefficient just before and beyond the K-absorption edge [10].

In principle, to originate X-rays through this mechanism, any two levels can combine and produce a line in the X-ray spectrum, however, most level combinations can be neglected because of their low intensity, as a result of different selection rules that can reduce significantly the intensity of transitions (section 1.1.2.1).

1.1.2.1 Selection rules and characteristic lines

The original nomenclature system for X-ray wavelengths was proposed by Manne Siegbahn, in 1923, in his book "The Spectroscopy of X-rays". Siegbahn received the Nobel Prize in Physics in 1924 [11] for his discoveries and research in the field of X-ray spectroscopy. His nomenclature, now called the Siegbahn notation, was based on the relative intensity of lines from different series, but provided no information about specific origin of X-ray lines.

In the Siegbahn designation system [4, 3], the symbol of an X-ray spectral line is based on the following:

1. The lines are labelled (K, L, M,...) based on the electron shell that was ionized and subsequently filled;

2. A Greek letter is added as a subscript and is related to the shell that provided the neutralizing electron. The α lines arise from $\Delta n = 1$ transitions (where n represents the principal quantum number of a shell). β and γ lines were discriminated by Siegbhan based on their intensities and some inconsistencies arise, leading to a non-systematic notation, specially in the case of the M and N series, which were observed only after the introduction of Siegbahn notation;

3. Because of the sub-shells existence, a transition from a shell to another has not the same energy. In that case, the highest energy transition between two shells is indicated by the number 1, the second highest by the number 2, etc...

In the case of $K_{\alpha 1}$ and $K_{\alpha 2}$, and $K_{\beta 1}$ and $K_{\beta 2}$ (usually called doublets), the energy

difference between the lines in each pair is very small, which means that it is difficult to resolve them. For that reason, these lines are usually identified only by K_α and K_β [8].

Despite the inconsistencies in the Siegbahn notation, this is still the most used nomenclature for X-ray lines within the X-ray analytical community, and so, it will be the notation used during this work.

Contrary to Siegbahn's notation based on the intensities of the observed X-ray transitions, the International Union of Pure and Applied Chemistry (IUPAC)[12] proposed a new system for identifying X-ray lines. IUPAC notation is based on the designation of the energy levels by declaring the sub-shells involved in the transition. The IUPAC system labels X-rays using:

1. A level symbol for final state (K, L, M ...), i.e., based on the electron shell that was photo-ionized and subsequently filled;

2. A level symbol for initial state (K, L, M ...), i.e., the source of the neutralizing electron;

3. Arabic numbers for identifying sub-shells (L_2 and L_3, etc...)

The Table 1.1 summarizes all significant characteristic X-rays and their corresponding Siegbahn and IUPAC names, and also gives the relative line intensities to the α lines of each series.

The relationship between the atomic number of an element (Z) and the wavelength (λ) of a characteristic X-ray photon was first established by Moseley, in 1914. This relationship, known as Moseley's law, is written as [1, 10]:

$$\lambda = \frac{K}{(Z - \sigma)^2} \tag{1.5}$$

Where Z is the atomic number of the excited element, K and σ are constants, different for each line; σ is a screening constant to correct the effect of the orbital electrons in reducing the effective nuclear charge.

Each unique atom has a number of available electrons that can take part in the transfer and originate a characteristic X-ray. However, electron transitions cannot occur from any higher to any lower level. Relaxation routes are defined by a simple set of selection rules for the quantum numbers of the states involved in the transition.

Each electron in an atom can be defined by four quantum numbers. The first quantum number, called principal quantum number n, represents the shell of the atom ($n = 1$ for K level, $n = 2$ for L level, and so on). The orbital angular momentum ℓ is an integer quantum number characterizing the angular momentum state of the particle and can take all values from zero to (n - 1) . The magnetic quantum number m can take values from $-\ell$ to $+\ell$,

and the spin s quantum number can assume values of $\pm 1/2$. The total momentum J of an electron is given by the vector sum of $\ell + s$.

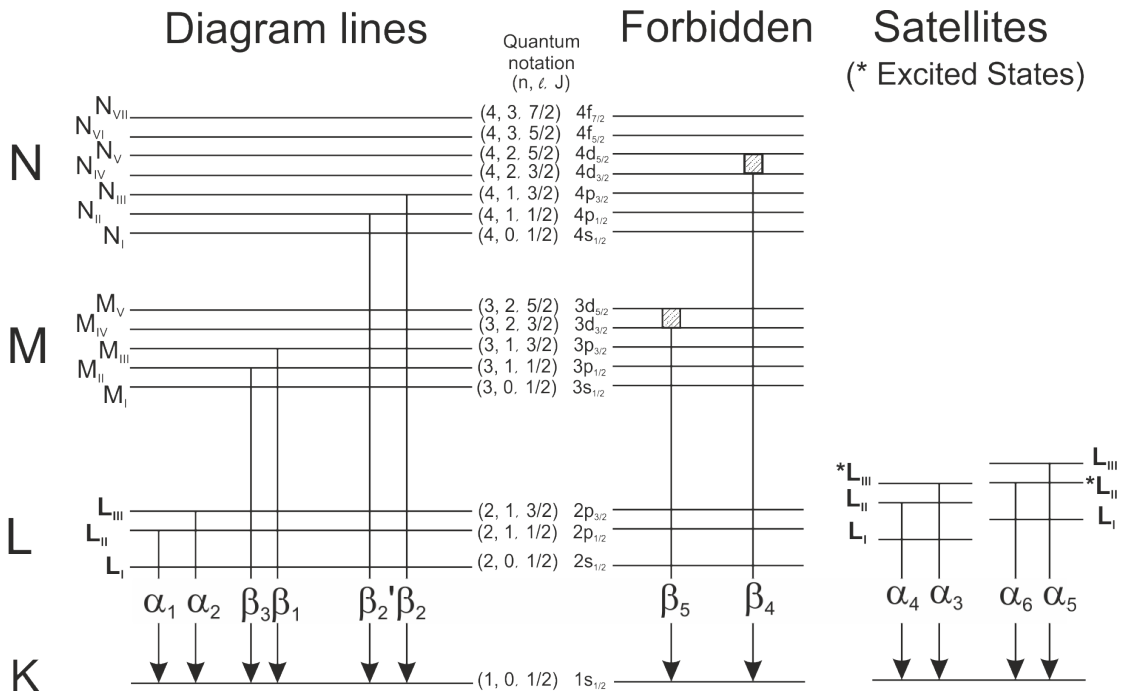

Figure 1.4: Characteristic lines observed in X-rays spectral K-series. Figure adapted from [4].

The selection rules that determine the allowed transitions are: $\Delta n \geq 1$, $\Delta \ell = \pm 1$ and $\Delta J = 0$ or ± 1 [2]. Spectral lines that obey to the selection rules are usually called diagram lines and those that violate them are known as forbidden lines. Figure 1.4 shows the diagram lines together with the forbidden and satellite lines (which will be explained later) corresponding to the K-series [4].

While most of the observed fluorescent lines follow the mentioned rules, certain lines may occur in X-ray spectra which do not obey to the basic selection rules. These lines are called forbidden lines. They usually arise from outer orbital levels where there is no sharp energy distinction between orbitals. As an example, in the transition elements, where the 3d level is only partially filled and is energetically similar to the 3p levels, a weak forbidden transition (β_5) is observed.

Table 1.1: X-ray lines - Siegbahn and IUPAC notation.

		Sub-Shell Filled													
		K		L_I		L_{II}		L_{III}		M_{III}		M_{IV}		M_V	
		Siegbahn	IUPAC	Siegbahn	IUPAC	Siegbahn	IUPAC	Siegbahn	IUPAC	Siegbahn	IUPAC	Siegbahn	IUPAC	Siegbahn	IUPAC
Source Sub-Shell	L_I														
	L_{II}	$K_{\alpha 2}$ (50)	K-L_2												
	L_{III}	$K_{\alpha 1}$ (100)	K-L_3												
	M_I					L_η (1)	L_2-M_1	L_ι (2)	L_3-M_1						
	M_{II}	$K_{\beta 3}$ (1)	K-M_2	$L_{\beta 4}$ (5)	L_1-M_2			L_t (0.01)	L_3-M_2						
	M_{III}	$K_{\beta 1}$ (20)	K-M_3	$L_{\beta 3}$ (6)	L_1-M_3	$L_{\beta 1}7$	L_2-M_3	L_s (0.01)	L_3-M_3						
	M_{IV}	$K_{\beta 5}$'	K-M_4	$L_{\beta 1}0$	L_1-M_4	$L_{\beta 1}$ (50)	L_2-M_4	$L_{\alpha 2}$(10)	L_3-M_4						
	M_V	$K_{\beta 5}$"	K-M_5	$L_{\beta 3}$	L_1-M_5		L_2-M_5	$L_{\alpha 1}$(100)	L_3-M_5						
	N_I					$L_{\gamma 5}$ (0.1)	L_2-N_1	$L_{\beta 6}$(0.1)	L_3-N_1						
	N_{II}	$K_{\beta 2}$" (5)	K-N_2	$L_{\gamma 2}$ (1)	L_1-N_2										
	N_{III}	$K_{\beta 2}$'	K-N_3	$L_{\gamma 3}$ (2)	L_1-N_3										
	N_{IV}	$K_{\beta 4}$	K-N_4			$L_{\gamma 1}$ (10)	L_2-N_4	$L_{\beta 1}5$(1)	L_3-N_4	$M_{\gamma 2}$ (1)	M_3-N_4				
	N_V	$K_{\beta 4}$	K-N_5					$L_{\beta 2}$(20)	L_3-N_5	$M_{\gamma 1}$ (1)	M_3-N_5				
	N_{VI}					L_η	L_2-N_6					$M_{\beta 1}$ (50)	M_4-N_6	$M_{\alpha 2}$ (100)	M_5-N_6
	N_{VII}													$M_{\alpha 1}$ (100)	M_5-N_7

Beside the diagram and forbidden lines, transition lines with strongly reduced intensity exist, the so called X-ray satellite lines. Satellite lines are formed by radiative electron transitions in multiple ionized atoms, a fact that causes the overall structure of the electron shells to change, resulting in the production of X-rays with other energies. These multi-ionization X-rays appear as small satellite peaks near the characteristic X-ray peaks [4, 10]. Another important source of satellite peaks is the Auger process described in section 1.1.3.

Since they are relatively weak, forbidden transitions and satellite lines haven't great significance in the studies presented in this work.

The intensity of an fluorescence X-ray line is a function of the transition probability and of the ionization rate [1]. In general, the intensity of a line series is proportional to the jump ratio of the absorption edge associated with that series (section 1.1.2). The relative intensities of the series are shown in Table 1.1.

1.1.3 X-ray spectra and the Auger effect

As explained in section 1.1.2, when an atom is ionized in one of its inner shells, it rearranges itself by filling the vacancy with an electron from an higher orbit, releasing the energy of the transition as a characteristic X-ray photon. Alternatively, an excited atom may return to a lower energy by ejecting one or more electrons from the outer shell. This radiationless transition is called Auger effect and the electron is an Auger electron [2].

In this process there are three electrons involved; the first is the photoelectron, which is emitted when the incoming X-ray photon is absorbed. In the subsequent relaxation process, an outer shell electron fills the vacancy and releases a characteristic X-ray photon. This energy can be transferred to a third electron, which is bound to the atom in an outer shell.

Similarly to the characteristic X-ray photons, the Auger electron energy is characteristic of the emitting element.

According to quantum-theoretical models, the existence of separable intermediate states during relaxation is denied and the relaxation and emission of the Auger-electron is treated as a single process. Consequently, the atom is left in a doubly ionized state, in which two electrons are missing. This atom returns to its fundamental state by single electron jump emitting diagram lines or by double electron jumps emitting satellite lines. Alternatively, another Auger electron can be ejected from a further outer shell [3].

The Auger effect is more common in elements of low atomic number, because their electrons are more weakly bound and the characteristic photons more readily absorbed.

Furthermore, another effect can take place within the L, M, and higher sub-shells: electrons can move from outer sub-shells to unoccupied states of inner sub-shells, e.g., from L_3 to L_2 after L_2 ionization or K-L_2 relaxation. This effect is called a Coster-Kronig transition and it differs from the Auger effect only by its confinement to a set of sub-shells.

1.1.4 Fluorescence Yields

The characteristic photon emission and the Auger electron emission are considered competing processes during the release of the extra energy that an atom possesses after an electron jump. Hence, this energy can be emitted as characteristic radiation or alternatively it can be used to reorganize the electron distribution within the atom itself leading to the ejection of an electron. Thus, an important consequence of the Auger effect is that the actual number of X-ray photons produced from an atom is less than expected, since a vacancy in a given shell might be filled through a non-radiative transition.

The probability of filling a vacancy in an atomic shell or sub-shell via a radiative transition, i.e., a characteristic X-ray photon emission, is given by a quantity called fluorescence yield (w). The fluorescence yield w_i, where i designates the shell involved, is given by the ratio of the number of emitted X-rays to the total number of ionizations in that shell (Eq. 1.1.4)[1].

$$w_K = \frac{\sum (n_K)_i}{N_K} = \frac{n_{K_{\alpha 1}} + n_{K_{\alpha 2}} + n_{K_{\beta 1}} + n_{K_{\beta 2}} + ...}{N_K} \tag{1.6}$$

Where w_K is the K fluorescence yield, N_K the total number of ionizations in the K-shell and $(n_K)_i$ the number of photons emitted from a spectral line i. The L and M fluorescence yields can be similarly defined.

The sum of the yields from radiative electron transitions w and from non-radiative transitions a (Auger yield) and f (Coster-Kronig transition probability) is normalized to:

$$w + a + f = 1 \tag{1.7}$$

The w value varies with atomic number and K, L, M, etc. series. Its dependence with the atomic number of the element can be written as [1]:

$$w_i = Z^4/(A_i + Z^4) \tag{1.8}$$

Where A_i is approximately 10^6 for the K-shell and 10^8 for the L-shell. According to the equation 1.8, the fluorescence yield increases with atomic number, since the probability of producing an Auger electron decreases [10]. Similarly, for a given element the fluorescence yield decreases from the K series to the L and M series, as shown in Figure 1.5.

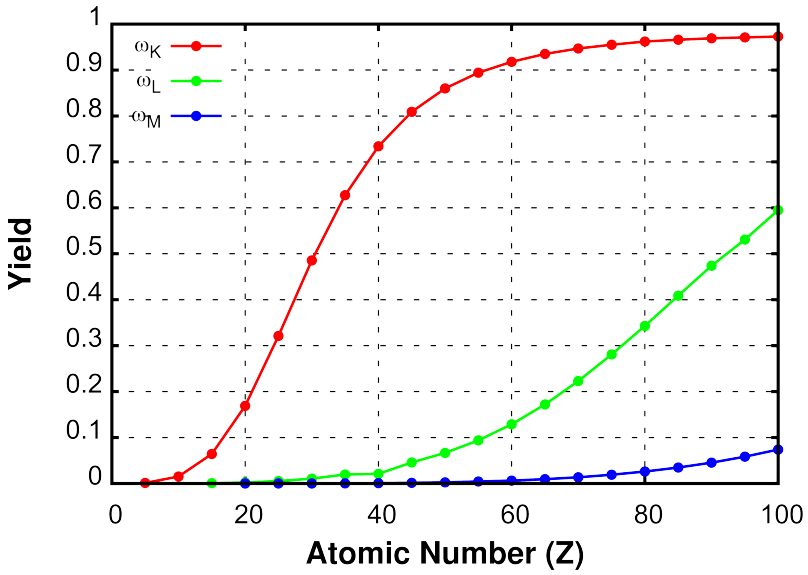

Figure 1.5: Fluorescence yield values (w_K, w_L and w_M) as a function of the atomic number. Data taken from reference [13].

1.2 State of the Art of EDXRF Imaging Systems

During the last decades, countless developments in the field of X-ray optics and detector technology associated with X-ray fluorescence techniques were made, evolving the technique from elemental analysis, without spatial information, into space-resolved elemental imaging analysis.

The energy resolved X-ray Imaging technique allows us to obtain distribution patterns of the chemical elements in multi-component samples, for instance, in biologic samples or cultural heritage materials. It is widely used for environmental, industrial, biological, bio-medicine and scientific research applications.

This kind of imaging systems are usually based on scanning systems composed by an X-ray micro-beam which scans the sample in both X and Y directions. At each irradiated point, the characteristic photons are collected by using an energy dispersive detector, providing the elemental composition of each scanned point. Another option, considered as a more efficient alternative, is to use a broader X-ray beam to irradiate the entire area of the sample to be imaged and record the fluorescence photons by using a two dimensional energy dispersive detector, without scanning measurements. These systems are known as full-field of view systems and are usually based on pixel detectors, such as Charge Coupled Devices CCDs [14–16], Medipix [17] or PILATUS detectors [18–20].

In this section, a brief review on the state-of-art of X-ray fluorescence imaging systems is presented. The systems shortly described in this section represent only a small fraction of all the work developed by the scientific community, an effort was made on showing the systems which exhibited the most significant improvement in the field over the past few years.

1.2.1 Scanning Systems

Micro X-Ray fluorescence (μXRF), associated with energy dispersive detectors is considered a powerful tool in elemental analysis.

Like conventional X-ray fluorescence (XRF) instrumentation, Micro X-Ray fluorescence uses direct X-ray excitation to induce characteristic X-ray fluorescence emission from the sample, for elemental analysis. But, unlike conventional XRF systems, μXRF uses X-ray optics in order to restrict the excitation beam size or focus the excitation beam to a small spot on the sample surface so that small features on the sample can be analysed. Thus, the evolution in μXRF imaging analysis, has been directly related with the development of technologies involved in focusing a divergent X-ray beam from an X-ray tube into a small dimension spot [21, 22].

One of the ways of doing that is through capillary optics [21, 23] which uses the principle of total reflection to focus the beam in spots as small as dozens of micrometers. The resulting increased intensity delivered to the sample in a small focal spot allows for enhanced spatial resolution in small feature analysis and enhanced performance in the measurement of trace elements [24].

The pioneer work in the development of μXRF was done during the 1980s [22]. Since then, several research groups and industrial companies have been manufacturing analytical equipment combining low-power X-ray tubes with focusing capillary lenses. A series of different X-ray spectrometers for different applications has been also designed.

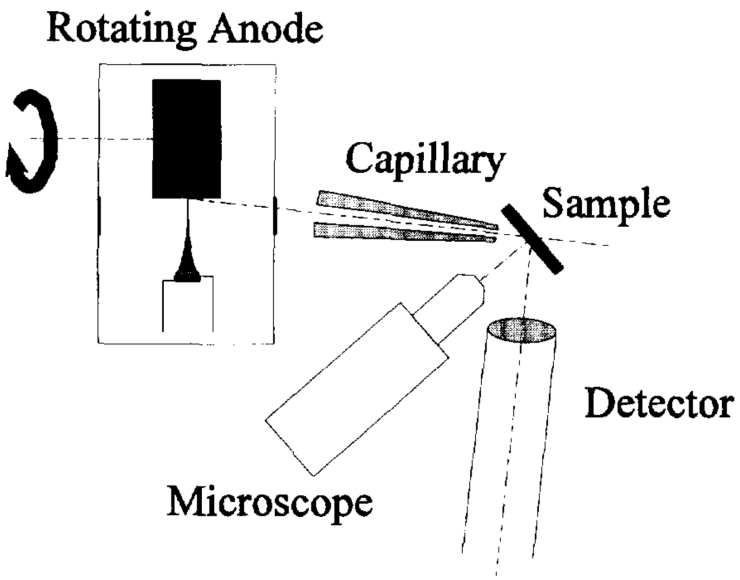

Figure 1.6: Schematic drawing of the μXRF set-up from the University of Antwerp [25].

In 1996, K. Janssens [25] and his co-workers, designed and developed a μXRF spectrometer, at their laboratory at Antwerp University. The system consists of a powerful 18 kW rotating anode X-ray tube. The samples are mounted on a XYZ stage, controlled with 1 μm precision. The fluorescence radiation is detected by a 80 mm^2 Si(Li) detector with 180 eV resolution for the Mn K_α line (5.9 keV). The detector is placed at 90° to the incoming radiation beam and at 45° to the sample. Several single capillaries, as well as policapillary lenses, were used in the experiments. Count-rates of about 0.5 MHz at 18 kW and spot sizes of about 15 μm were achieved. A schematic of the experimental setup is shown in Figure 1.6.

After some investigation about components selection for a μXRF spectrometer [26], the Eagle III μ-probe^{TM} was designed and manufactured by Roentgenanalytik Messtechnic GmbH (Taunusstein, Germany) together with EDAX^{TM} (Mahwah, NJ, USA). The EAGLE-III μ-probe^{TM} spectrometer is an instrument used for non-destructive scanning μXRF analysis. Similarly to other spectrometers, it uses capillaries and a energy dispersive detector [21, 22, 27].

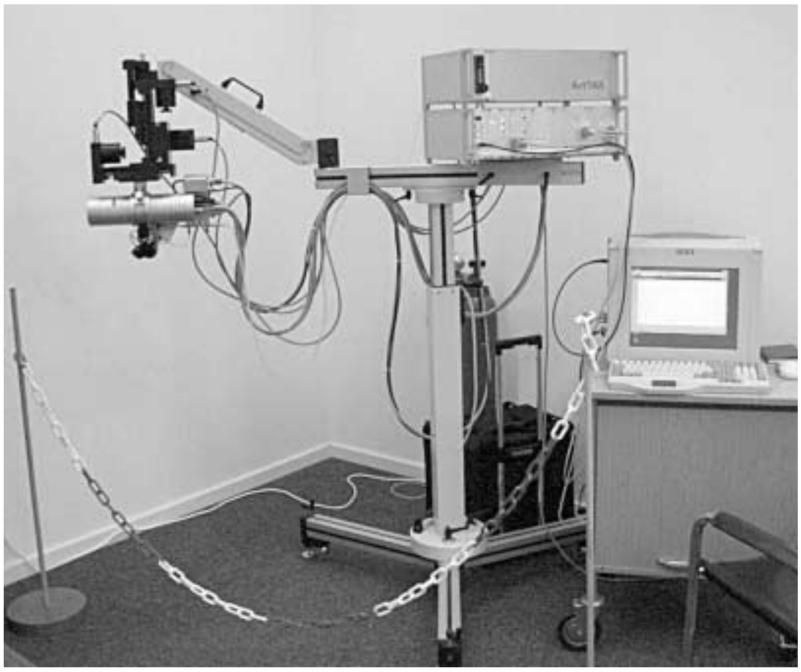

Figure 1.7: Set-up of the mobile μ-XRF spectrometer ArtTAX [28].

The X-ray source is a Rh-tube, optionally with Mo and W as possible anodes, with a maximum load of 40 W. The X-ray beam is focused by a monocapillary lens with a focus spot of 300 μm diameter or by policapillary optics with spots diameter sizes ranging from 20 to 40 μm. The X-ray detector located inside the instrument is an energy dispersive Si(Li) detector with an active surface area of 80 mm^2, cooled by liquid nitrogen. An energy

resolution of 140 eV for the Mn K_α line can be obtained when measuring at a total count rate of 5 kHz.

A sample stage is also present, which can be moved in the XYZ directions. The motor stages can move with an accuracy of 1.5 μm. The instrument can be operated under vacuum, making the detection of low energy X-rays possible, as attenuation in air is eliminated.

Bronk, *et al.*[28] introduced in 2001 the ArtTAX (Figure 1.7), a mobile spectrometer for art and archaeological objects. In order to facilitate working outside the laboratory, the system avoids vacuum conditions, which usually lead to a size-limit sample chamber. The spectrometer consists of a low-power molybdenum air-cooled tube (30 W maximum power), polycapillary X-ray optics that focuses the beam to 100 μm, a silicon drift detector without the need for liquid-nitrogen cooling, a CCD camera, and three light photodiodes for sample positioning. The motor-driven measurement head is fixed on a XYZ flexible tripod support.

In 2004, Vittiglio *et al.*[29] developed a portable version of the μXRF spectrometer for in-situ analyses of cultural heritage and forensic materials. The COPRA spectrometer is composed by a compact, air-cooled micro-focus X-ray tube with Mo anode operating at 35 kV/0.7 mA, combined with a polycapillary lens that provides a focused X-ray beam of 70-100 μm in diameter. The fluorescence radiation is detected by a silicon drift detector having a resolution of 145-160 eV at the Mn K_α line. For sample visualization, an optical zoom microscope with a field of view of 1.5-15 mm wide is used. The COPRA instrument, including the *in situ* version, is shown in Figure 1.8.

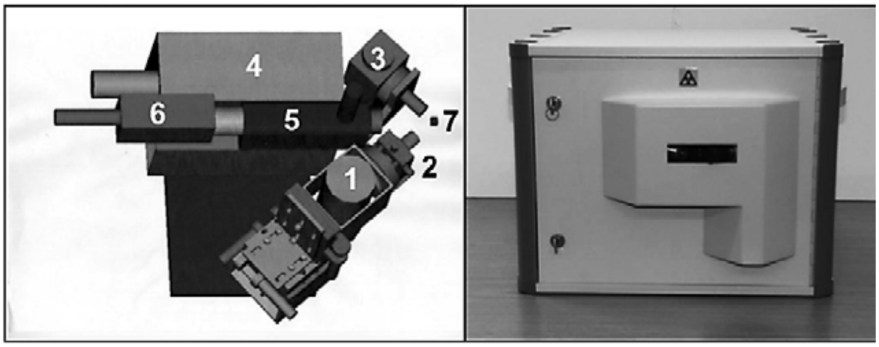

Figure 1.8: Left: Configuration of the COPRA instrument parts: (1) X-ray tube, (2) polycapillary lens, (3) drift chamber detector, (4) X-ray tube power supply, (5) microscope, (6) optical CCD camera, (7) sample position. The centre and right panels respectively show the *in situ* version of the instrument. Right: Mobile version of the instrument [29].

In 2007, an EDXRF imaging system was developed using a compact X-ray tube and an array of silicon drift detectors [30]. With this device, elemental mapping of samples was produced, covering areas of up to 100 mm^2. The X-ray beam is produced by a compact and

low power X-ray tungsten anode generator and focused by a polycapillary X-ray lens. The sample is positioned on an XY stage with micrometric resolution, which is responsible for the scanning. The detector itself is composed by an array of four independent silicon drift detectors arranged around a hole located at the centre of the chip, to maximize the photon density in the excitation spot, even if a low power X-ray generator is used. The total active area of the detector is about 60 mm^2. At rates up to 300 kcps, the resolution is below 220 eV FWHM at the Mn K_α line. Applications were found in the field of medical and biochemical sciences to exploit the capacities of the spectrometer in imaging analysis of elements present in very low concentrations. In this study, a 10×10 mm^2 area was analysed with 400 μm pitch.

More recently (2012), a low cost and portable EDXRF imaging system was proposed by Figueroa, *et al.* [31]. The system is capable of scanning large areas (up to 10×10 cm^2) in steps as small as 0.2 mm. It consists of a MiniX X-ray tube and a XR-100SDD Silicon Drift Detector (commercially available from AmpTek^{TM}), both mounted in a gantry support. The gantry is coupled to a robotic arm with two degrees of freedom (XY).

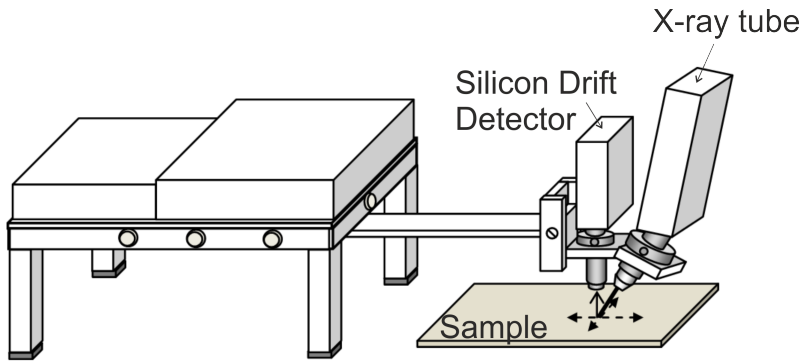

Figure 1.9: General scheme of 2D EDXRF imaging system proposed by Figueroa *et al.* The system consists of a X-ray tube and XR-100SDD Silicon Drift Detector mounted in a gantry supporting piece. The gantry is coupled to a robotic arm with two degrees of freedom (X and Y), being capable of scanning rectangular areas of up to 10x10 cm2 with steps as low as 0.2 mm [31].

The low power X-ray tube operates with a maximum voltage and current of about 40 kV and 200 μA, respectively. The energy dispersive detector presents a resolution of 136 eV at the Mn K_α line energy and allows the detection of elements between 1.5 and 40 keV. The best spatial resolution, 1.1 mm, was achieved for a pitch of about 0.2 mm and a focal spot of about 0.75 mm. The paper [31] describes possible applications of the scanner system in the biological field, namely in the study of potentially toxic elements, e.g. Cd, Hg, Pb and As, and their spatial distribution in biological samples.

This last system cannot be considered as a μXRF but as a mili-XRF system, due to the

spatial resolution offered. However, it allows large area and fast analysis, which can be very useful in some applications where the spatial resolution is not the main requirement.

The main features of the discussed scanner systems for EDXRF are summarized in Table 1.2, in an attempt to give the reader the necessary information for a comparative analysis of the systems.

1.2.2 Full-Field XRF Systems

As explained in 1.2.1, in conventional approaches, for EDXRF imaging system analysis, the sample is mapped by an X-ray beam. In each mapping position, usually called pixel, the fluorescence radiation is collected and analysed in order to determine the elemental composition of each pixel, by using a fine mechanical XYZ stage. In the past few years, an effort to cross over from compact point detectors to 2D resolving detectors has been done, specially to overcome the scanning complexity of these systems. These 2D detection systems can measure spatial information and are usually known as Full-Field X-Ray Fluorescence (FF-XRF).

Due to recent developments in pixel-detector technology, there is a number of Full-Field X-Ray Fluorescence devices becoming available for EDXRF measurements. Although these devices differ in terms of working principle and performance, the main experimental setup for such a measurement is the same. In Full-Field X-Ray Fluorescence, the entire sample is excited by a broad X-ray beam and the fluorescence radiation is detected by a 2D energy resolved pixel detector. The full-field camera detects the XRF spectra on a pixel-by-pixel basis, providing spatially resolved elemental imaging capabilities without the need of using a focused X-ray microbeam and sample scanning. An X-ray optics, e.g. polycapillary optics or a pinhole camera placed in front of the detector, provide the desired imaging properties.

In 2007, a simple energy resolved X-ray fluorescence imaging system composed by a static X-ray tube, a pinhole (collimator) and a Charge Coupled Device (CCD), acting as an X-ray detector, was proposed by Vasin *et al.* [14].

A sample (material with a complex chemical composition) is irradiated by an X-ray tube with a molybdenum anode [14]. A pinhole is used to focus the X-ray photons to the CCD camera, as illustrated in the experimental system setup - Figure 1.10. The CCD consists of a 1242×1152 matrix of discrete elements (pixels) made of silicon crystals (photodiodes) in a single chip, corresponding to an active area of detection of about 25.9×27.5 mm^2. This device is an integrated circuit in which the output charge in each pixel is proportional to the intensity of the incident light [14].

In order to record spectral information, the CCD camera operates in single photon counting mode, in order to avoid pileup events to be registered in the matrix elements of the CCD, during the acquisition, in a single frame[14].

In this mode, the charge value registered by each element of the CCD array will be

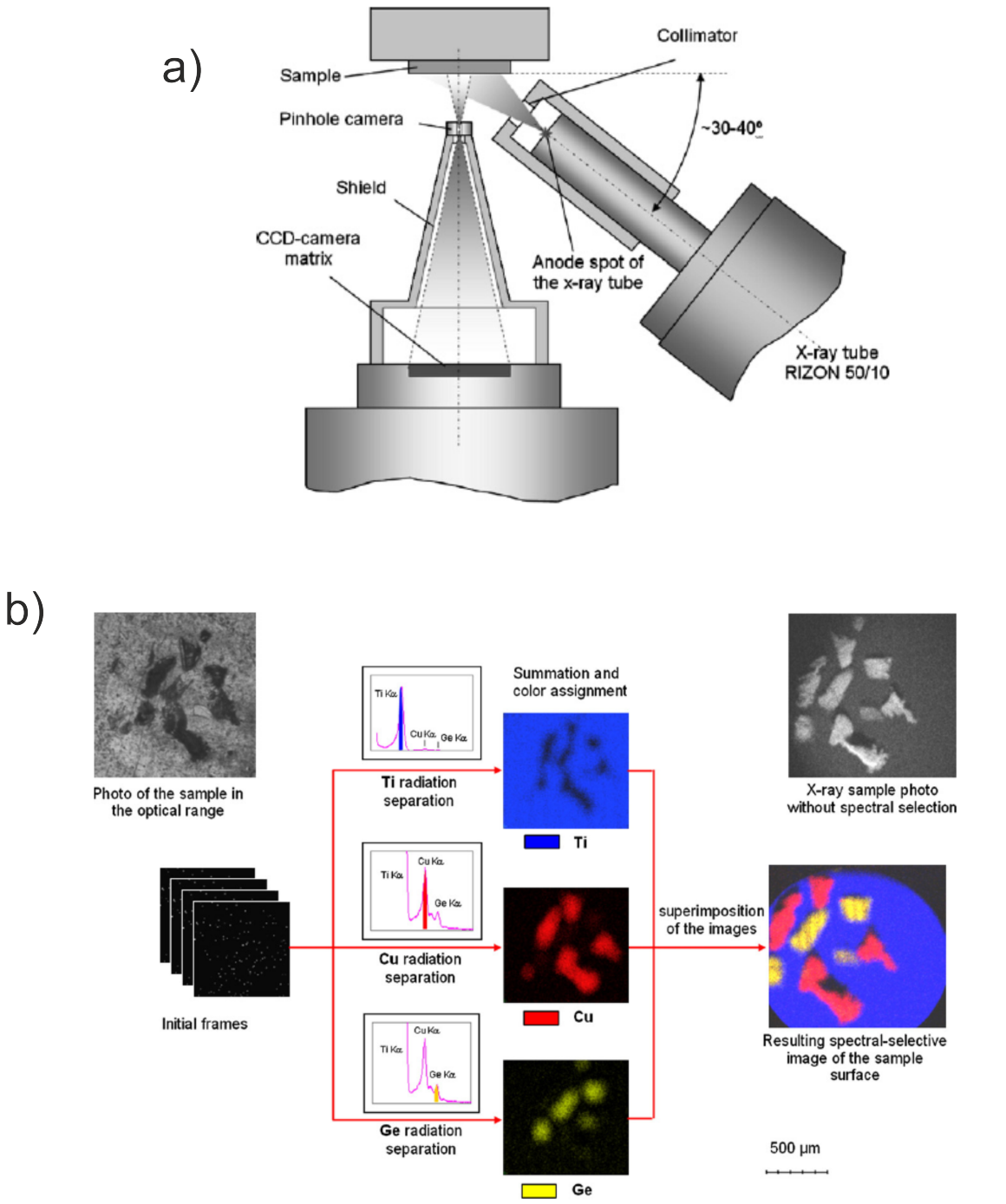

Figure 1.10: a) Scheme of the experimental system used in [14] b) The algorithm of the image generation with spectral selection.

proportional to the energy of a single photon. Thus, the amplitude distribution of charges collected in the active elements of the entire CCD array corresponds to the energy spectrum.

The disadvantage of the proposed system is that a high count rate it isn't feasible in order to maintain single-photon counting mode and a low counting rate also limits it operation due to the low signal-to-noise ratio (SNR) obtained. In each frame, that corresponds to one

acquisition during a fixed time interval, the charge that arrives at each element of the array is collected. After the collection of information, all frames are added. Selecting energy intervals in the spectrum corresponding to the characteristic energy of each chemical element present in the sample (peaks in the distribution of pulse amplitudes), it is possible to obtain an image of this element distribution in the sample. Repeating the same procedure for all the spectrum peaks it is possible to obtain images of the other elemental components, and their spatial distribution in the sample - an **EDXRF image**. Thus, correlating all the images, it is possible to obtain the surface elemental distribution map of the sample [14]. The process is outlined in Figure 1.10. Spectral resolution of the CCD-camera was determined with the K_α peak of the Cu fluorescence radiation and is equal to 400 eV. The camera is sensitive to energies between 3 and 20 keV. This enables the recording of the characteristic radiation of the K-series lines of the elements with atomic number between 19 and 42, as well as L-series lines of the elements with atomic number between 48 and 95. Another important feature of the system is related with the spatial resolution, which is limited by the hole diameter of the pinhole camera used. It could be up to 10 μm.

In 2010, Alfeld *et al.* [15] proposed a FF-XRF system for simultaneous elemental imaging. The experiments in the laboratory were done using a 200 W X-ray tube, a 75 μm pinhole, and an energy resolved CCD. The detector is composed by an array of 512×512 pixels, each one with 24×24 μm^2 area. The sensitivity of the CCD limits the detection of soft X-ray photons below 10 keV. For energies up to 14.1 keV long exposure times are needed because of the too low intensity measured, in order to determine the elemental spatial distribution. This means that the efficiency of the CCD is good for energies from 10 keV to 14.1 keV. Another problem of this kind of detectors is related with the occurrence of multi-pixel events. When the charge spreads over various pixels, fractional energies are observed in more than one pixel, instead of one photon with the correct energy. In the case of an overexposure, many photons are detected per pixel, which leads to a distortion in the energy spectrum. For this reason, overexposed pixels cannot be taken into account, thus neglected. The energy resolution of the proposed system was found to be 235 eV for the Mn K_α line. The system proposed by Alfeld *et al.* was also used in synchrotron experiments. In that case, a pinhole diameter of 25 μm was found to be the best compromise between detection efficiency and resolution (about 10 μm) [15].

Another recent example of a FF-XRF imaging system based on a CCD detector, emerged in 2011 and was introduced by Ordavo *et al.* [16]: the Color X-ray Camera (Figure 1.11 a)). The FF-XRF system is based on a pnCCD detector, coupled to a pollycapilary lens. This kind of detector can typically achieve an energy resolution of about 152 eV for Mn K_α line. The pnCCD is located inside the Color X-ray Camera at 6.2 mm behind the camera window, which consists of a 50 μm beryllium foil and can produce an image of 12.7 × 12.7 mm^2 comprising 264 × 264 pixels with a size of 48 μm each. In order to neglect the noise

due to dark current, the pnCCD is permanently cooled to a temperature below -25°C.

The Color X-ray Camera [32] uses polycapillary optics acting as photon "guides" from small regions on a sample to corresponding pixels in the detector. The spatial resolution of the system can be approximated to the pixel size of the pnCCD, since the channel diameter of the capillary optics does not exceed the pixel size. A spatial resolution of about 56 μm was estimated for the system. The camera is sensitive to photons from 3 to 40 keV and can work at a frame rate of about 400 Hz.

The pnCCD detector is capable of registering individual photons hitting separate pixels. It acts as a single-photon counting detector with photon energy discrimination, achieved by applying event reconstruction algorithms. The application of this kind of method is limited by the count rate. If the latter becomes too high, single events overlap precluding the correct determination of the energy and position information. Thus, if a proper limitation of the count rate is adopted, a single photon energy spectrum can be obtained, as shown in Figure 1.11 b). In this way an EDXRF image (Figure 1.11 c)) can be created by selecting Region of Interest (ROI) in the energy spectrum, corresponding to the elemental fluorescence lines.

As shown, energy dispersive X-ray cameras suitable for FF-XRF are being developed for several years, generally employing advanced CCDs, as in some systems described earlier in this section. An alternative to CCDs are pixel detectors such as the Medipix2/Timepix (as in the system proposed by Tichy *et al.* [17]) or the PILATUS detector [18–20].

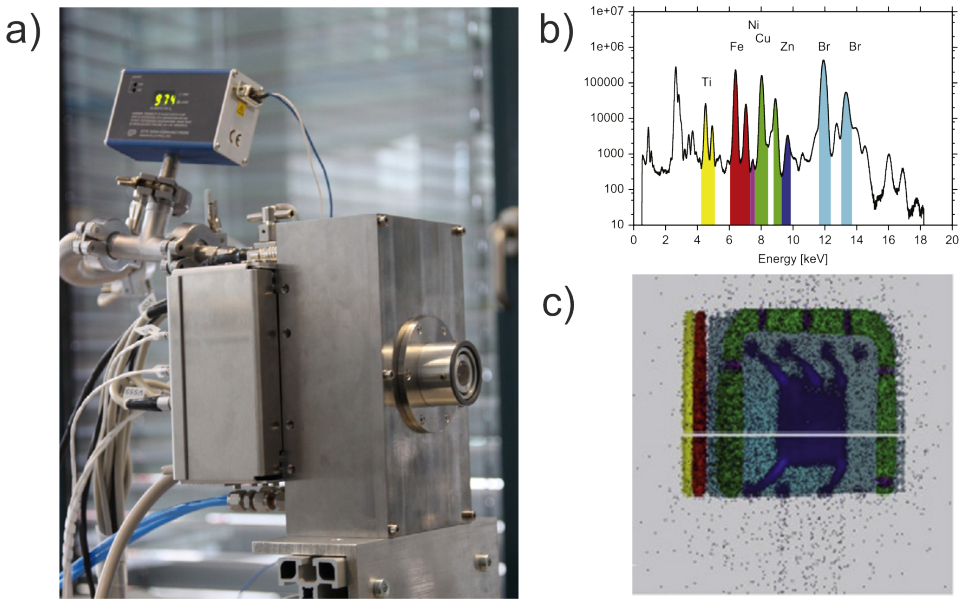

Figure 1.11: a) Photo of the experimental setup [32]. Example of a b) total spectrum of a c) back illuminated SIM card obtained with the Color X-ray Camera. This image was acquired using monochromatic synchrotron radiation as X-ray source. The color code of the image c) corresponds to the color code of the ROIs chosen in the energy spectrum c) [32].

In 2008, a system of X-ray fluorescence imaging has been proposed by Tichy *et al.* [17]. It uses single photon counting detectors, as in the case of the Medipix2, developed in an international collaboration at CERN, and Timepix Chip derived directly from the Medipix2. The Medipix2 is a silicon detector, consisting of a sensor attached to a readout chip. The sensor consists of a 256×256 array of electrodes (pixels). Each electrode has an area of 55×55 μm^2 and is connected to its own read-out channel. Each pixel is, in fact, a single channel analyser with a digital counting device, which allows to count photons individually. The Timepix uses time over threshold mode based on the measurement of the signal duration which is a function of the incoming X-ray photon. It operates in event-by-event regime, i.e., the exposure time has to be very short to avoid detection of more than one photon per pixel per frame, which strongly limits the count rate.

The experimental system developed by Tichy *et al.* consists of an X-ray tungsten tube, and a lead pinhole camera with a Medipix2/Timepix detector. The energy resolution of the Medipix2, 1.63 keV at 25.3 keV (FWHM of the Sn peak) [33] or the Timepix, 2.8 keV at 15.8 keV (K_α line of Zr) and 3.2 keV at 24.2 keV (K_α line of Indium) [34] is not sufficient to carry information about characteristic radiation in each pixel.

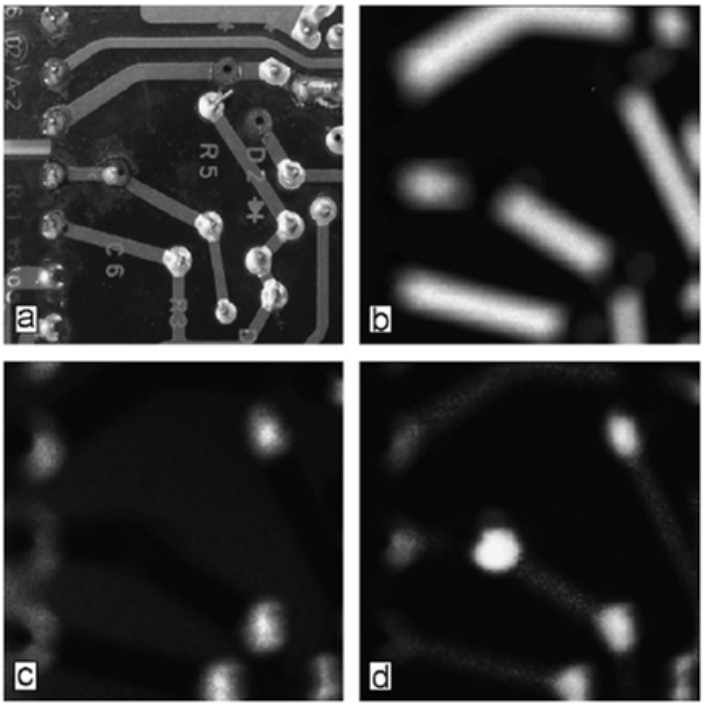

Figure 1.12: PCB: (a) PCB photo. Distribution of (b) copper; (c) tin; (d)lead obtained by decomposition technique [17].

Thus, Tichy has proposed a method to overcome this disadvantage. The method comprises two phases: in the first step (calibration) the spectroscopic response of each pixel in terms

of characteristic radiation of the individual elements in a known sample is measured. In the second stage, a complex spectrum of an unknown sample is measured and then decomposed into spectra of individual elements [17]. Using this method, distribution of elements with spacing between the characteristic lines of about 500 eV can be determined.

Although energy resolution is not sufficient to identify characteristic lines of individual elements, the method proposed for the decomposition of the spectrum allows the use of such devices in X-ray fluorescence analysis. Each pixel spectrum is a linear combination of spectra obtained for each element. It is possible to obtain EDXRF images, as illustrated on Figure 1.12. The pinhole used has a diameter of 1mm. The X-ray tube has operated with a 100 kV voltage and current of 1 mA [17].

The PILATUS detector [18, 19] is a silicon hybrid pixel detector system, developed at the Paul Scherrer Institut (PSI) in Switzerland, with 60×97 pixels, each of 172 μm size. The detector operates in single-photon counting mode. It consists of a single pixelated silicon sensor bump-bonded via microscopic Indium balls to an array of custom-designed and radiation-tolerant CMOS readout chips.

The detector was initially designed for X-ray diffraction and scattering experiments and consisted of an array of several thousand individual detectors that measure the energy of the recorded photons.

Toyokawa *et al.* [20] presents an interesting discussion about the threshold energy calibration for the PILATUS detector. Direct acquisition of an energy dispersive spectrum is not possible with this detector, however an indirect approach can be used, by which the threshold is scanned over the desired energy range.

A threshold scan curve of a pixel corresponds to the integrated energy spectrum of the X-ray source above the threshold. Hence, the derivative of a threshold scan performed with monochromatic X-rays can be seen as a spectral peak, in which the Full Width at Half

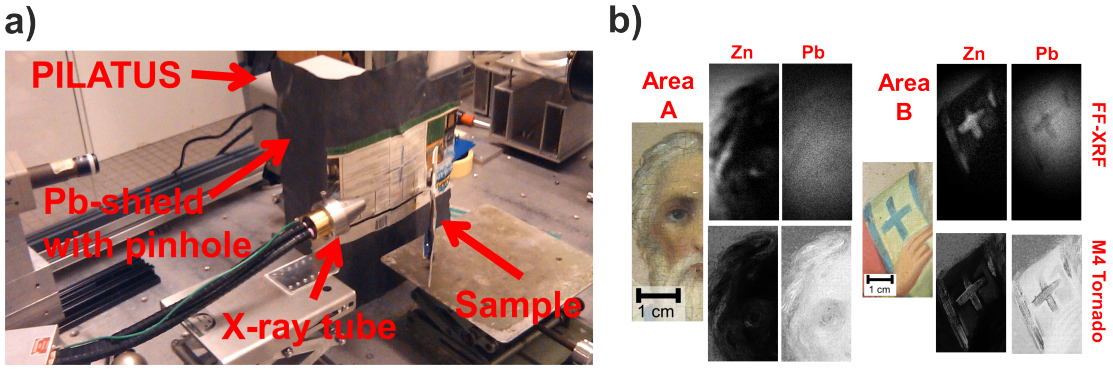

Figure 1.13: a) Apparatus experimental of the FF-XRF imaging system based on a PILATUS detector; b) Elemental distribution images of Zn and Pb acquired with the FF-XRF set-up and with a μXRF set-up, for comparison, for area A and B of the sample. Adapted from [35].

Maximum (FWHM) represents, in principle, a measure of the energy resolution of the system [18].

Alfeld *et al.* presented, in 2012, a poster communication in the conference Synchrotron Radiation in Art and Archaeology (SR2A) [35], showing for the first time the "Evaluation of a PILATUS Detector as Camera for Full-Field FF-XRF Element-Specific Imaging". In the system proposed, an uncollimated 10 W Rh-anode X-ray tube was used as an X-ray source. The set-up was also composed by a pinhole of 1 mm diameter. The energy resolution was found to be $\approx$ 1 keV.

Analysis of two areas on a 19th century icon were investigated by using the FF-XRF imaging system based on PILATUS detector. The results are shown in Figure 1.13.

In Table 1.2, an overview of the main characteristics of the state of the art EDXRF systems reported in this section, is presented. The table should be understood as a comparative summary of the systems presented, allowing the reader to quickly identify advantages and disadvantages of these systems, when compared to the system proposed and described throughout the next chapters of this work.

Table 1.2: Overview of EDXRF imaging systems described in the literature: a) Scanner Systems and b) FF-XRF Systems.

State-of-Art: EDXRF Imaging Systems														
a) Scanner Systems														
System	Ref.	Portability	X-ray source specification				2D Imaging		Detection					Low-Z Element Detection
			Anode Element	Maximum tube power (W)	Focusing lens	Focal Spot diameter on the sample (µm)	Step size (µm)	Spatial Resolution (µm)	Detector Type	Count Rate (kHz)	Detector area (mm^2)	Field of view (mm^2)	Energy Resolution (eV for Mn K_α)	
Rotating anode and capillary optics	[25]	laboratory system	Cu; Mo	18000	monocapillary; polycapillary	15	1	15	Si(Li)	500	80	n.s.	180	n.s.
Eagle III µ-Probe	[21] [22] [27]	laboratory system	Rh; Mo; W	40	monocapillary	300	1.5	variable	Si(Li)	5	80	n.s.	140	Operation in vacuum
					polycapillary	20-40								
ArtTAX	[28]	portable	Mo	30	polycapillary	100	10	108	Si(Li)	10	5	50	160	n.s.
COPRA	[29]	portable	Mo	24.5	polycapillary	70-100	n.s.	70-100	Si drift	n.s.	n.s.	1.5-15	145-160	n.s.
Ultra-fast XRF spectrometer	[30]	laboratory system	W	n.s.	polycapillary	n.s.	400	n.s.	Si drift	300	60	100	220	n.s.
Low cost and portable EDXRF spectrometer	[31]	portable	Ag	8	collimator	750; 1000; 1500; 2000	200; 400; 600; 800	1100	Si drift	n.s.	12.5	100x100	136	Z>13 (1.5 keV)

n.s. - not specified

b) FF-XRF Systems												
System	Ref.	Portability	X-ray source specification		2D Imaging and detection							Low-Z Element Detection
			Anode Element	Maximum tube power (W)	Optics	Pixel size (μm^2)	Detector Type	Detector area ($pixels^2$)	Count Rate (Single photon counting)	Spatial Resolution (µm)	Energy Resolution (eV)	
Energy resolved XRF imaging system	[14]	laboratory system	Mo	n.s.	Pinhole (ø=15, 60, 200 µm)	22.5x22.5	CCD	1242x1152	Low	up to 10	400 (Cu Kα)	Z>19
FF-XRF system for simultaneous elemental imaging	[15]	laboratory system	W	200	Pinhole (ø=25µm)	24x24	Energy ResolvedCCD	512x512	Low	10	235 (Mn Kα)	Z > 33 (10 keV)
Color X-ray Camera	[16] [32]	portable	Rh	n.s.	Polycapillary lens	48x48	pnCCD	264x264	400 Hz	56	152 (Mn Kα)	Z > 19 (3 keV)
Medipix2/ Timepix based system	[17] [33] [34]	laboratory system	W	100	Lead pinhole (ø= 1 mm)	55x55	Medipix2	256x256	Low	55	1630 (Sn Kα)	n.s.
							Timepix				2800 (Zr Kα) 3200 (In Kα)	
FF-XRF imaging system based on PILATUS detector	[18] [19] [20] [35]	laboratory system	Rh	10	Pinhole (ø=1mm)	172x172	PILATUS	60x97	n.s.	172	1000	n.s.

n.s. - not specified

CHAPTER 2

INSTRUMENTATION - GAS IONIZING DETECTORS

Gas-filled detectors are versatile detectors able to detect radiation of a wide range of energies and types. The greater mobility of electrons and ions in a gas makes it a medium of excellence for the collection of ionization from radiation. The basic configuration of a gas-filled detector is shown in Figure 2.1 and consists of a closed volume filled with an adequate gas, usually pure or based on a mixture of noble and organic gases. It consists of two electrodes, the cathode and the anode, between which a certain electrical potential is applied. When an ionizing particle comes into the detector volume, passing through the space between the electrodes, it may interact with the gas, ionizing and exciting the atoms along the path, dissipating part or all of its energy by generating electron-ion pairs, preferentially by photoelectric effect. This process was discussed in section 1.1.1 which was dedicated to the interaction of X-rays with matter. Usually, for simplicity, the electron-ion pairs are designated only as ion-pairs. For this reason and, from now on, one will adopt this term.

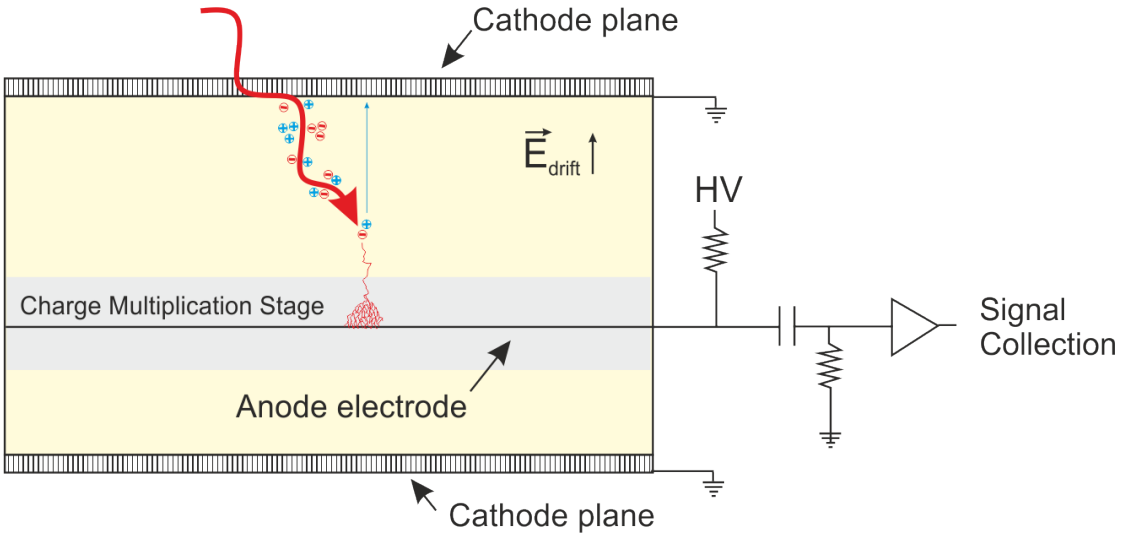

Figure 2.1: Schematic of a gas-filled detector operation.

So, as a consequence of the radiation interaction with the gas, a cloud of charge carriers, ions and electrons, is created in the gas. The bunch of electrons generated is called primary electron cloud. Compared to electrons, the ions present very low drift velocity in the gas, since they are heavier particles, as will be discussed in more detail in section 2.1.1. Therefore, the signals produced by the ions are usually very slow, which makes them not so much desirable for most applications. Because of this, in this work only the signals generated by the collection of electrons will be considered.

In the absence of electric fields, collisions between the positive ions and free electrons created during the ionization process may occur, resulting in recombination, which leads to a state of charge neutrality. Instead, if adequate electric fields are applied, the electrons and the ions drift in opposite directions (to the anode and to the cathode electrodes, respectively).

In gaseous detectors applications for X-ray detection, which is the case of the work presented here, the number of primary electrons created by the incident particle is very low and is not measurable by the electronics. In this case, the primary charge needs to be amplified. By applying a suitable drift field, sufficient to suppress recombination, the primary electrons drift towards the gas to a region where a more intense electric field is applied, as illustrated in Figure 2.1.

In this region, the electrons are highly accelerated between collisions, acquiring high kinetic energy. In every interaction their direction changes, originating a very winding path. Therefore, when the ionization threshold of the gas atoms is reached, these electrons may ionize the gas and more ion-pairs are created. The process continues with the secondary charge originating tertiary charge and so on, causing a process of charge multiplication - the Townsend avalanche. The charge multiplication process will be discussed and exploited in detail in section 2.1.2. Therefore, the final charge produced is orders of magnitude higher than the primary charge. Furthermore, the Signal-to-Noise ratio (SNR) is improved, which leads to a better energy and spatial resolution in the case of imaging aplications, as will be shown later on, in the section 3.1.1.5.

In this chapter the principles of operation of gaseous detectors are described, focusing on the most relevant mechanisms involved in the detection process, together with a brief historical review of the different types of gaseous detectors developed during the last century, until reaching the Micropattern Gas Detectors (MPGDs), which are the ones with more interest to this work.

2.1 Physical principles

Gaseous detectors can work in different modes of operation depending on the applied voltage within the detector. Figure 2.2 shows schematically a typical plot of the number of electrons collected in the anode electrode, as a function of the applied voltage.

At very low voltages (region I), the recombination of electrons and ions is high and consequently, the collected charge and the output signal is weak, so it doesn't corresponds to the number of primary electrons initially generated in the gas.

As the voltage is increased, the recombination of electrons and ions is suppressed, but no gas multiplication occurs. In this region, labelled II, most of the free electron reaches the anode. A detector in this mode is insensitive to the voltage which means that within this range the increase of the electric field does not increase the number of electrons, and the gain is the unity. This is called the region of ion saturation and corresponds to the electric field range used in ionization chambers (the simplest of all gas-filled detectors).

As the potential is further increased, gas multiplication starts. The accelerating electric field is high enough to impart to the primary electrons, an energy higher than the first

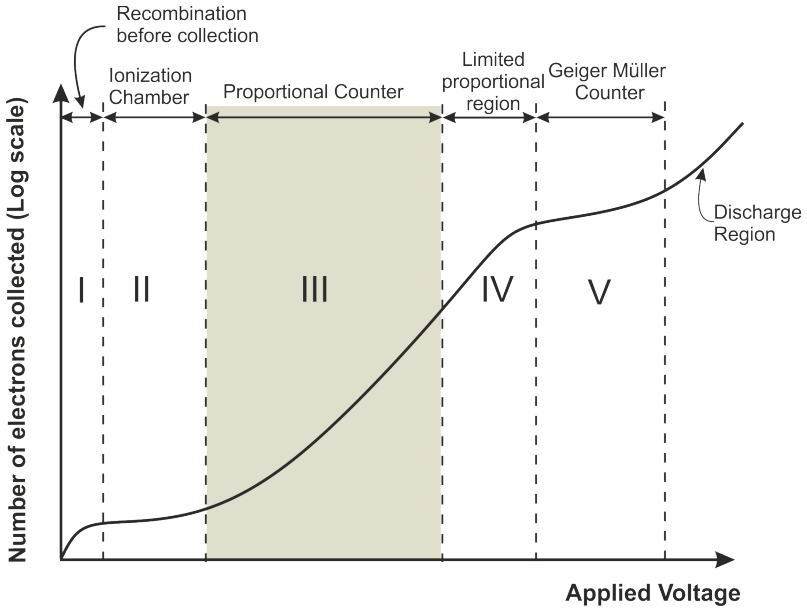

Figure 2.2: The different modes of operation of gas-filled detectors.

ionization potential of the gas. These electrons then produce ion-pairs along their path; the secondary electrons may, in turn, form further pairs, promoting charge multiplication. This is called the proportional region (III) and represents the mode of operation of proportional counters since the total number of electrons generated in the avalanche is proportional to the number of primary electrons created and thus to the energy of the incoming particle.

Strict proportionality assumes that space charge (due to the longer-lived positive ions) and induced effects remain negligible, compared to the external field. At higher electric fields, or in a high flux of charged particles, the space charge effects can alter the effective electric field, the chamber works in the mode of limited proportionality (region IV) and the number of electrons generated in the avalanche is no longer strictly proportional to the number of primary electrons.

As the voltage is further increased, the space charge inside the avalanche is strong enough to shield the external field, and the proportionality is lost. In this region, called Geiger-Müller region (region V), the whole volume of the gas detector becomes ionized with only one single interaction and each output pulse from the detector has the same amplitude (self contained amplitude), independently of the energy of the individual X-ray photons.

Despite the different behaviours of the operation of gaseous detectors, they all derive from the ion-pairs initially formed within the gas filled detector. Therefore, regarding the mechanisms involved in the detector's operation, a quantity of interest is the total number of ion-pairs created by the incoming particle.

The average energy required to produce an ion-pair in the gas medium is defined as the W-value, W. The W-value is much higher than the average ionization energy required to

eject the bound electrons from an atom in the ground state, due to the occurrence of other competitive mechanisms, such as excitation processes.

The W-value is characteristic of the gas species involved. For xenon it is assumed to be 21.9 eV, and for Ne it is 36.2 eV [7, 36]. For the Ne/5%CH_4 there is no value for W-value in the literature, therefore it was calculated by using the simulation program Magboltz/Mip [37] and found to be 29.7 eV. Details about the calculation of the W-value for the Ne/5%CH_4 are shown in section 3.1.2.4.

Since the occurrence of ionizations in the gas is a statistical process, two different X-ray photons, with the same energy, may not, produce the same number of ion-pairs. These fluctuations in the number of ion-pairs created by each X-ray photon limit the energy resolution that can be achieved by the detector, as will be explained with detail later in section 3.1.1.2.

The formation of the total number of ion-pairs in the gas is given by a Poisson distribution. Therefore, if a total number of primary electrons N_p is created on average, one should obtain a standard deviation of $\sqrt{N_p}$. However, experimental measurements have shown that the processes that originate the formation of each charge carrier are not independent. In all cases, the variance is shown to be lower than the correspondent given by Poisson statistics. Therefore it was introduced by U. Fano [38], in 1947, the Fano factor (F), which represents the relative variance of the real distribution. It is defined by the ratio between the variance in the number of ion-pairs, σ_p^2, to its measured mean value, $\overline{N_p}$:

$$F = \frac{\sigma_p^2}{\overline{N_p}} \tag{2.1}$$

Higher values of the Fano factor thus indicate a broader distribution of the number of ion-pairs created than that described by lower values of F.

2.1.1 Diffusion, drift and mobility of electrons in gases

Phenomena as diffusion and drift in gases under an electric field may influence many operating characteristics of the detector. When electrons move freely among the molecules of a gas in the absence of an electric field, they randomly change their diffusing direction between collisions within the gas molecules, originating a sinuous path. Due to these collisions, the electrons lose energy and come quickly into thermal equilibrium with the gas, after which recombination may occur.

In an ionization detector, after the creation of the primary electron cloud it is usually applied an electric field in order to force the cloud of electrons to drift along the direction of the electric field lines, avoiding recombination processes.

Due to their smaller mass, the mobility of the electrons, μ_e, in the gas medium, is much

greater than that of the ions, and between collisions they are much more accelerated than ions. Furthermore, they lose only a small fraction of energy in the elastic collisions, due to the ratio of the electron mass to the entire atom mass, which is very low.

Thus, when an electric field is applied, the electron cloud and the ions drift in opposite directions. The ions drift towards the cathode electrode and the electrons towards the anode electrode. The average velocity of all the electrons from the electron cloud is usually called drift velocity, υ, and is superimposed on the random thermal velocity.

The drift velocity depends on the mobility of the electrons in the medium and also on their mean free path. Since the mean free path is inversely proportional to the pressure, p, and the energy of the electrons depends on the reduced electric field, E/p, one can assume that the drift velocity is also a function of the reduced field strength, as shown by the equation 2.2 [7]:

$$\upsilon = \mu_e \frac{E}{p} \tag{2.2}$$

Higher drift velocity of charge carriers means faster signals to be detected, which is desirable for most detectors devices. The mobility of electrons is about 1000 times greater than that of ions, which leads to typical collection times of the order of μs [7]. On the other hand, the low drift velocity of ions can, for instance, generate space charge effects distorting the electric field inside the detector, which can leads to a deterioration of the energy resolution obtained.

After a diffusing time in the gas, and a slow drift under an uniform electric field, the distribution of charges in the gas follows a Gaussian law. From the point of creation, the charge spreads into a Gaussian-like spatial distribution with a standard deviation which depends of the time of diffusion, t. The standard deviation, σ_x, for electron diffusion along a transverse projection axis, x, is described by [7, 39]:

$$\sigma_x = \sqrt{2Dt} \tag{2.3}$$

Where D is the transverse diffusion coefficient.

The diffusion of the electrons in the gas can be of the order of a millimeter or less. In position-sensitive detectors, which is the case of the detectors presented in this work, this can affect the intrinsic position resolution.

2.1.2 Charge Multiplication process

Charge multiplication occurs when the primary electrons produced in the gas acquire, between collisions, enough energy to ionize gas molecules. This is only possible under the effect of an adequate electric field, by which the electrons are accelerated between collisions.

The resulting secondary electrons are then also accelerated and produce additional electrons during their drift, which are themselves potential creators of ion-pairs. The process of charge multiplication will continue resulting in the formation of an avalanche, known as Townsend avalanche.

The motion of the particles in an avalanche is a combination of drift and diffusion (section 2.1.1), and because of the higher mobility of electrons relatively to ions, the avalanche shape is similar to a liquid drop with ions grouped in the beginning of the drop and the electrons grouped in the tail.

The Townsend avalanche is described by the Townsend coefficient α, which is a measure of the probability of an ionization per unit path length.

Thus, if multiplication occurs, the increase in the number of electron per path dx can be written as follows:

$$dn = n\alpha dx \tag{2.4}$$

This coefficient α is determined by the excitation and ionization cross sections of the electrons that have acquired enough energy in the field. Therefore, no fundamental expression exists for α and it must be measured for every gas mixture [7]. It also depends on the electric field strength. It is zero below the ionization threshold and above this minimum it increases with the electric field strength.

For a uniform electric field, α is a constant. Therefore, the average number of electrons produced in the avalanche per primary electrons increases exponentially along the path, x:

$$n = N_p e^{\alpha x} \tag{2.5}$$

The ratio n/N_p is known as the gas multiplication factor, M.

$$M = e^{\alpha x} \tag{2.6}$$

Although eqn. 2.6 can increase without limit, there is a physical limit for the multiplication factor, after which discharges can occur. This physical limit is known as Raether limit and occurs for $M > 10^8$ and/or $\alpha x > 20$ [5].

2.1.3 Gas Selection

The choice of the gas for a gaseous detector is usually determined by the specific requirements of the detector and purpose for which the counter is to be used. It must fulfil different demands such as: proportionality between the energy of the radiation and of the detector response, a high gas multiplication, low detector working voltages and high counting rate detection capability, time resolution, drift velocity, detection efficiency.

Noble gases are commonly chosen for that purpose because they need the lowest detector voltages for avalanche formation. Attachment of electrons to the gas molecules must be avoided to make the detector work efficiently. Therefore, electronegative gases containing, for instance, oxygen are not desirable. Thus, the filling gas of the detector is usually based on a noble or hydrocarbon gas, or a mixture of both, since they are characterized by low electron attachment coefficients. To avoid contamination by impurities, the detector vessels are designed to keep the gas clean as much as possible. The detector can be designed to maintain the gas permanently sealed inside it, which is more convenient when expensive gases (for example, Kr or Xe) are used; or it can be designed to enable a circulation of the gas in a continuous flow through the detector chamber. The detectors developed during this work, that will be shown and discussed later in chapter 3 are examples of the two different possible detector configurations. In the case of sealed detectors, some additional requirements are needed to increase the lifetime of the detector. In most cases it is necessary to use a purifying material, such as, getters, which are capable of recycling the gas by removing electronegative impurities.

During the gas multiplication process, electrons induce ionization and also excitation of the atoms. Excited atoms deexcite giving rise to photons capable of ionizing the cathode and causing further avalanches - photon-feedback effect. This leads to a possible loss of proportionality and/or to the generation of spurious pulses, which have nothing to do with the incident radiation [7, 5]. These effects are more relevant when gases with higher ionization energy are used, as Ar. Furthermore, the spread of the avalanches through the detector chamber can increase the dead time of the detector, i.e., the minimum amount of time needed to record two events as two separate pulses.

To avoid this, small amounts of polyatomic gases can be added to the counting gas, acting as *quenching gases*. Polyatomic gases allow absorbing photons without further ionizations, by dissipating the energy through dissociation or elastic collisions. CH_2, CH_4, C_4H_{10} and inorganic compounds such as CO_2 and BF_3 are often used for this purposes. The increase of the number of atoms in the molecule is directly related to the *quenching* efficiency. The problem is that organic compounds tend to cause also aging effects in the detector, by the formation of solid and liquid polymers on the anode and cathode surfaces. They are also generally flammable, which requires special safety precautions.

For imaging applications, heavy rare gases such as xenon and krypton are the best choice,

although they are quite expensive. The reason is that they are much more efficient for the detection of X-rays. For Energy Dispersive X-Ray Fluorescence, Xe is the most interesting one, as will be seen in section 3.1.1.1.

Another important effect to consider is the *Penning effect*. For the *Penning effect* to happen, metastable excited states must exist in the principal gas of the mixture. If the ionization energy of the second gas is lower than the excitation energy of the principal gas, then a deexcitation may occur through a collision with an atom of the second gas, resulting in the ionization of the latter. Thus, more ion-pairs are produced per unit of energy, leading to a decrease of the W-value. This leads to a decrease of the fluctuations relative to the number of electrons produced, and to a correspondent increase of the intrinsic energy resolution of the detector. That is why *Penning* mixtures are commonly chosen for gaseous detectors developed for radiation spectroscopy.

2.2 Gas filled detectors

2.2.1 First Steps of gaseous detectors

The Geiger-Müller counter is considered the most basic and one of the oldest gaseous radiation detectors. It consists of a simple closed cylindrical tube (cathode), filled with a gas, with a thin anode wire in its center [7]. This radiation detector was introduced by Geiger and Müller in 1928 [7]. If a very high electric field is applied between the cathode and the anode wire, the primary electrons generated in the gas, are highly accelerated and can promote an avalanche near the anode, in the multiplication region. During this process, apart from ionizations within their mean free path, the created electrons can further excite the molecules of the gas, which upon relaxation emit UV photons. The UV photons are then absorbed within the gas, ionizing its molecules and creating more free electrons, elsewhere within the detector. Those can themselves promote another avalanche at a different position within the tube, triggering avalanches chains. This process ends when the space charge effect (produced by accumulation of positive ions) is intense enough to decrease the electric field bellow the point at which gas multiplication is suppressed. Therefore, a Geiger tube can only work as a counter since each output pulse from the detector has the same amplitude and doesn't reflect the properties of the incident radiation.

In the case of proportional counters, each primary electron originates only one independent avalanche. Since the number of electrons generated per avalanches is similar, the collected charge remains proportional to the number of primary electrons, and consequently proportional to the incident radiation energy.

Typical gas proportional counters are structured and constructed with an identical cylindrical geometry to the Geiger-Müller counters, as illustrated in Figure 2.3 (Left).

In the case of a Gas Proportional Counter (GPC) the applied voltage is lower than in the

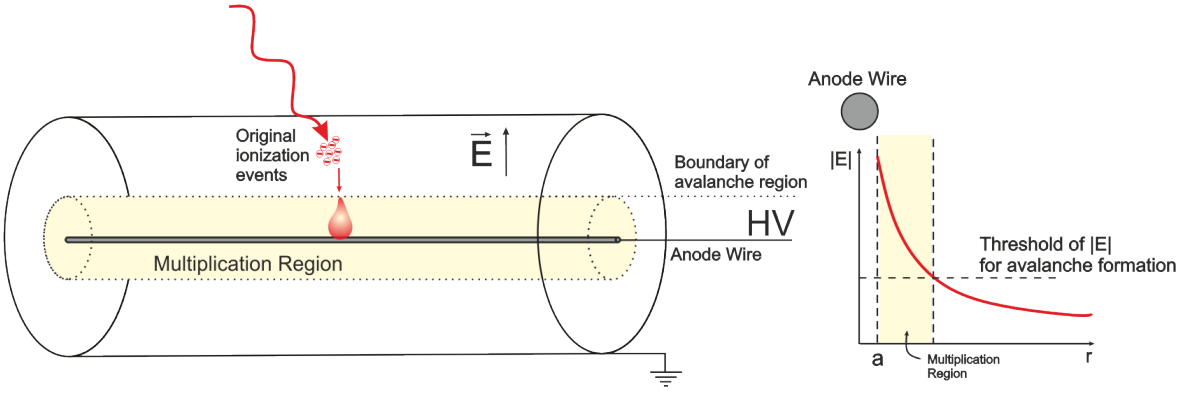

Figure 2.3: Left: Schematic of a GPC. It is possible to identify two different regions inside the device: the drift region and the multiplication region near the anode; Right: Electric field as a function of the distance r to the anode wire for a Gas Proportional Counter.

Geiger-Müller Counter but still high, in order to avoid the recombination of ion-pairs. and because gas multiplication requires a strong electric field. The electric field inside a cylinder like in a GPC, as a function of the radial distance r to the anode wire is given by [7]:

$$E(r) = \frac{V}{r \ln(b/a)} \tag{2.7}$$

Where V is the applied voltage between anode and cathode, a is the anode wire radius and b the cathode inner radius. Figure 2.3 (right) shows a plot of the behaviour of the electric field as a function of the radial distance, for a gas proportional counter with a cylindrical geometry.

In 1968, Georges Charpak developed the Multiwire Proportional Chamber (MWPC) [40], one of the most successful devices in the gaseous detectors field. The invention revolutionized particle detection and for that, Charpak, was later awarded the 1992 Nobel Prize in Physics. It consists of a gas-filled chamber with a large number of parallel detector wires, equally apart by 1 mm [40], each connected to an individual amplifier, as illustrated in Figure 2.4. The detector contains a thin film, the window, through which the particles come into the detector. The region between the window and the wire planes is called drift region. The inner part of the window has a positive applied voltage with respect to the cathodes that generates the drift field [7, 40].

An X-ray that enters in the detector through the window interacts with the gas, ionizing it. The primary electrons released during the interaction drift toward the anodes driven by the drift field applied. Close to the anode wires, where the electric field is high, an avalanche takes place. The gain has a strong dependence on the anode wires radius because the closer the avalanche can get to the anode wire centre, the higher the electric field is ($E \propto r^{-1}$) (eqn.

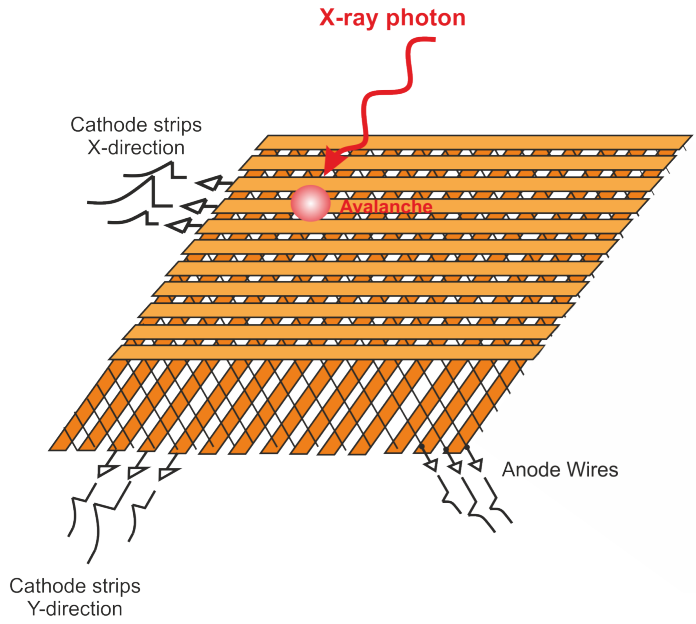

Figure 2.4: Scheme of a Multiwire Proportional Chamber. The anode plane is formed by wires placed between the other cathode planes.

2.7). The signal induced on the cathode wires can solve the arriving position of the event, as the wires of the two cathode planes are oriented orthogonally (X- and Y-direction), allowing the MWPC to act as a 2D-imaging detector.

The centroid position of the charge avalanche distribution can be roughly identified by the largest signal collected from all of the preamplifiers. In this situation, the spatial resolution is limited by the distance between the wires (between 1 and 2 mm [7]). To avoid the use of many preamplifiers, typically one for each channel, a readout system based on resistive or delay lines can also be implemented. Two resistive or delay lines are used, one for each dimension, interconnecting the cathode strips. By using charge division methods and algorithms to determine the charge distribution centroid, it is possible to achieve a better spatial resolution than the distance between the wires [5].

The MWPC simplicity regarding the geometry, working principle and operation, together with its versatility, have made it one of the most used detectors in many different applications, from medical imaging [41] to high energy physics experiments.

2.2.2 Micropattern Gas Detectors

Following the growing development in the gaseous detectors field, triggered by the evolution of the printed circuit board technology, a new concept of gaseous detectors emerged at the end of 1980s, the Micropattern Gas Detectors (MPGDs) [42–44].

A limitation of the MWPC has to do with the production of positive ions in the avalanches. They drift slowly through the gas and if the external radiation interaction rate is too high,

they accumulate in the gas volume and change the electric field. As a consequence, the proportional gain of the detectors dramatically decreases. To overcome this limitation, the drift path or the drift time of the ions has to be reduced, which means that the distance between anode and cathode have to be diminished. That is why micropattern detectors were developed with a fine granularity.

Micro-structured gas-amplification devices now open the possibility to apply the same technology as in semiconductor devices to gaseous detectors and enable a plethora of new detector concepts.

MPGDs usually present good spatial resolution, high rate capability, large sensitive area, operational stability and radiation hardness which makes them suitable for a large field of applications within particle, nuclear and astro-particle physics, etc. Typically, the new micro-pattern devices are based on a closed geometry. This geometry, contrary to the open geometry of the GPC and MWPC, avoids photon-feedback effects in which photons emitted due to the deexcitation of the atoms excited during the avalanche process can remove electrons from the walls of the detector and from the metal electrodes promoting additional and undesirable avalanches.

A great advantage of the MPGDs, is its cost when compared to the cost and size limitations of the semiconductor technology for large systems.

In this section an overview of different MPGDs with relative importance to this work, is given. Recent progress of detectors research, especially in the context of MSGC, GEM, MHSP and THCOBRA is discussed.

The CERN-RD51 collaboration is an R&D collaboration which aims to develop and optimize detector technologies related with the Micropattern Gas Detectors. The Detection Radiation and Medical Imaging Group (DRIM), from the Physics Department of the University of Aveiro, is one of the member institutes, together with other 83 institutes from 25 different countries. Part of the presented work has been developed within this collaboration.

2.2.2.1 Microstrip Gas Detector

The first approach of micropattern gas detectors was the Micro-Strip Gas Chamber (MSGC) introduced in 1988, by Oed at the Institut Laue-Langevin in Grenoble [45].

The MSGC is a position-sensitive proportional counter mounted on a substrate, with a similar operation principle to the MWPC. It consists of thin parallel metal strips alternatively disposed as anodes and cathodes, deposited on an insulating support, as illustrated in Figure 2.5. The anode is thinner (10 μm width) than the cathode electrode (100 μm width) [45]. Accurate photolithography can achieve distances between electrodes below 10 μm, allowing to improve the electrode density by more than one order of magnitude compared to the MWPC.

In this detector, the primary electrons are attracted to the anode strips according to the electric field configuration. During the avalanche a large fraction of ions are generated in the

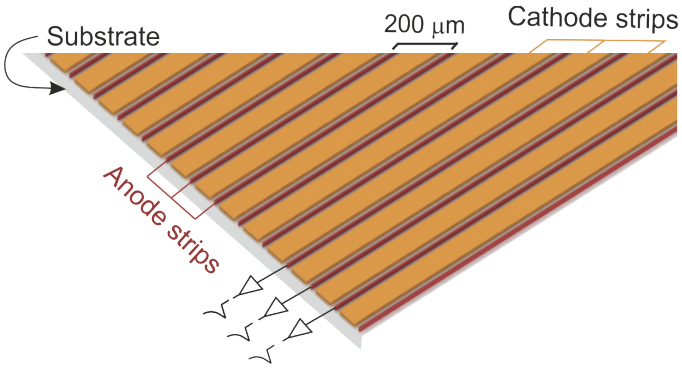

Figure 2.5: Electrode-structure of a MSGC.

vicinity of the anode strip. They drift to the cathode strips, which is much shorter distance than that ions need to drift until being collected in the case of the MWPC. This effect strongly reduces the space charge providing higher rate capability than in previous devices. Unfortunately, the thin strips proved to be very sensitive to destructive discharges, especially for highly ionizing radiation that could produce local shorts circuits between the anode and the cathode strips [42].

A great advantage of the planar structure is the possibility of fixing several microstructure patterns in the same substrate, allowing very large sensitive areas.

For 2D imaging, strips are etched on the opposite side of the MSGC, orthogonally to the anode strips of the structure, providing the second dimension. The signal collected in these strips corresponds to the induced current through the dielectric substrate of the structure.

Similarly to the MWPC, the charge can be independently collected from each strip, by connecting a preamplifier to each channel. On the other hand it is also possible to use a resistive line interconnecting all the strips for each dimension. Thus, it is possible to determine the centroid of the avalanche spectral distribution by using dedicated algorithms for that purpose.

Although the MSGC has been primarily developed for particle tracking, it also allows achieving energy information which is very useful for spectroscopic measurements. An energy resolution of about 15 % can be obtained for 5.9 keV X-rays when operating at counting rates of about 10^2 Hz/mm^2 [46]. In 2002, Bateman, *et al.*, reported spatial resolutions of about 0.1 mm (standard deviation) with readout rates of up to 400 kHz per anode for a two-dimensional X-ray detector based on gas microstrip detector using resistive division [47].

2.2.2.2 Gas Electron Multiplier

The Gas Electron Multiplier (GEM), was introduced in 1996 by Fabio Sauli [48]. This microstructure is composed of a 50 μm thick Kapton® subtract (a polymer insulator), with a 5 μm copper film deposited on both sides. Over the microstructure there are biconical

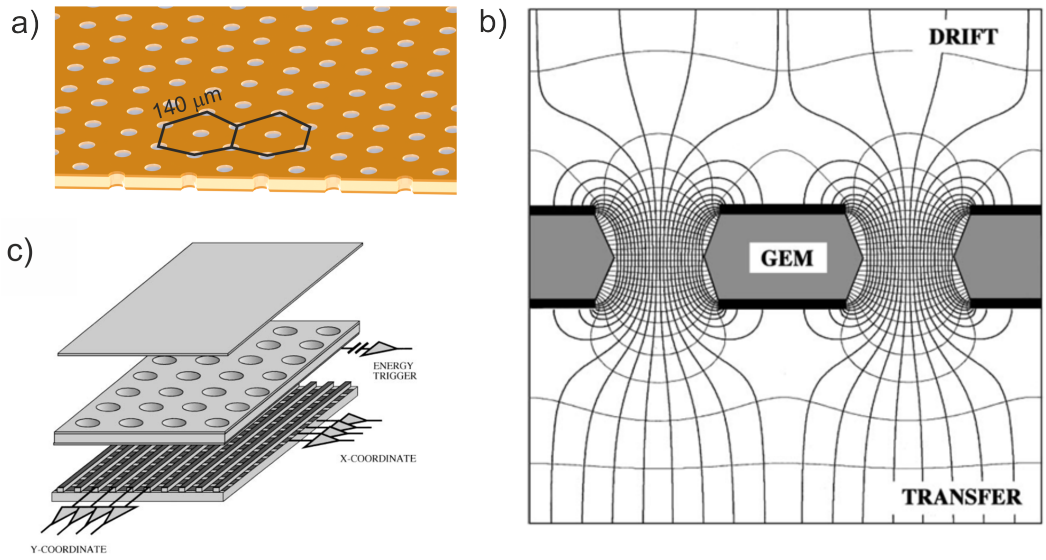

Figure 2.6: a) Electrode-structure of a GEM; b) Schematic structure of the GEM with electric field lines and equipotential lines shown [42]; c) View of a whole GEM detection system [42].

submillimeter circular holes periodically arranged in a hexagonal shape (with 140 μm long edges), across thickness, as illustrated in Figure 2.6 a). Applying a voltage between the two conductive plates, a strong electric field is generated inside the holes (see Figure 2.6b)). A readout plane is placed below the GEM amplification structure (Figure 2.6c)), for $2D$ imaging capability. Primary electrons released on the drift region are focused into the holes, where they are multiplied. Then the electrons are detected in the readout pads, that can be position sensitive charge readouts [49, 50].

Like almost all of the MPGDs, the GEM suffers from discharge problems at high gain and high rate, even if it is far less fragile than the MSGC.

Benefiting from its closed geometry, the reduction of the photon-feedback effect is even more pronounced in the GEM than in the MSGC. Since most of the excitations and ionizations happens inside the holes, most of the photons generated in the avalanche process are produced in the lower half part of the structure [51]. Thus, the photons cannot travel too long inside the detector since they are rapidly blocked by the structure itself.

GEM foils can be multi-staged allowing a distribution of the amplification over several foils (double- and triple-GEMs) and achieving safe detector operation by eliminating the risk of hazardous discharges. By using a triple-GEM it is possible to achieve gains above 10^4 in pure Xe [52], and $10^5 - 10^6$ for triple GEMs working with Ar or mixtures of Ar with Ne, Xe and CH4 [53].

Energy resolutions around 20 % (FWHM) for X-ray photons of 5.9 keV are possible. High rate capability, up to 1 MHz/mm^2 was achieved [54].

The advanced features of GEM-based detectors are: high counting rate, good spatial

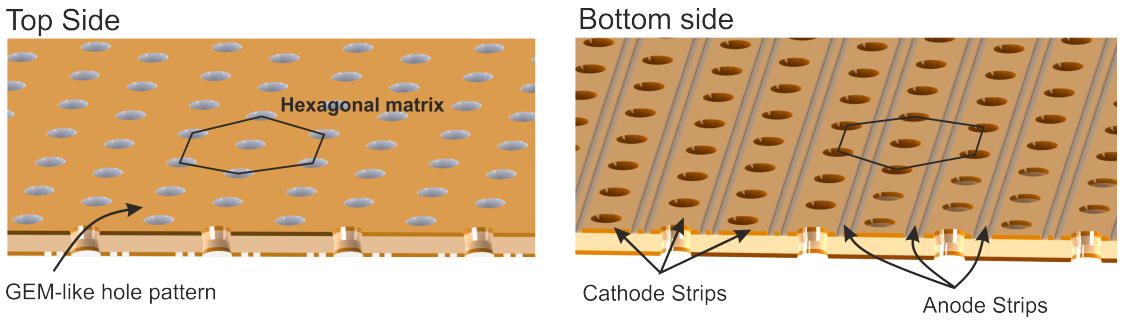

Figure 2.7: Electrode-structure of a MHSP. Left: Top view, the GEM-like side; Right: Bottom view, the MSGC-like side.

resolution (around 100 μm [50]), good imaging capability, large sensitive area (areas up to 1000 cm^2 are possible [55, 56]), flexible geometry and low cost.

2.2.2.3 Micro-Hole & Strip Plate

As stated above, MPGDs tend to be arranged in cascade with more than one amplification stage, in order to enhance the performance. This arrangement provides more stable operating devices and higher gains.

Following this development, a new and innovative device, called Micro-Hole & Strip Plate was introduced by Veloso, *et al.* in 2000 [57].

The micropattern structure of the MHSP is a hybrid structure that combines the characteristics of the GEM and the MSGC, allowing two multiplication stages, within the same device.

The standard Micro-hole & Strip Plate consists of a double-sided microstructure made of a Kapton® foil of 50 μm covered with a thin copper layer (5 μm) on both sides. On the top side, a GEM-like hole pattern is etched and, on the opposite side (bottom), a MSGC-like pattern is drawn, both produced through photolithography processes. The holes from the top side pass through the microstructure emerging in the centre of the cathode strips (100 μm width) of the MSGC-like side, as shown schematically in Figure 2.7. The cathodes are alternately disposed spaced of 40 μm with the anode strips (30 μm width).

The *modus operandi* of the MHSP is illustrated in Figure 2.8 and it is very simple and similar to MPGD devices discussed before. If a proper electric field is applied in the drift region, $\vec{E}_{drift}$, primary electrons produced by interaction of the incoming X-rays with the gas, are targeted to a region near the holes. By applying a voltage difference (higher than in the drift region) between the cathode strips and the GEM electrode of the MHSP, V_{CT}, the primary electrons are focused into the holes, where the first avalanche occurs because of the intense electric field inside them. The electrons that emerge from the holes, on the MSGC-like side, are again accelerated towards the anode strips, where the second multiplication in charge

takes place. Therefore, this device allows achieving higher charge gains because of the two multiplication stages when compared with GEM and MSGC devices operating in independent mode. The operation principle of the MHSP device is illustrated in Figure 2.8.

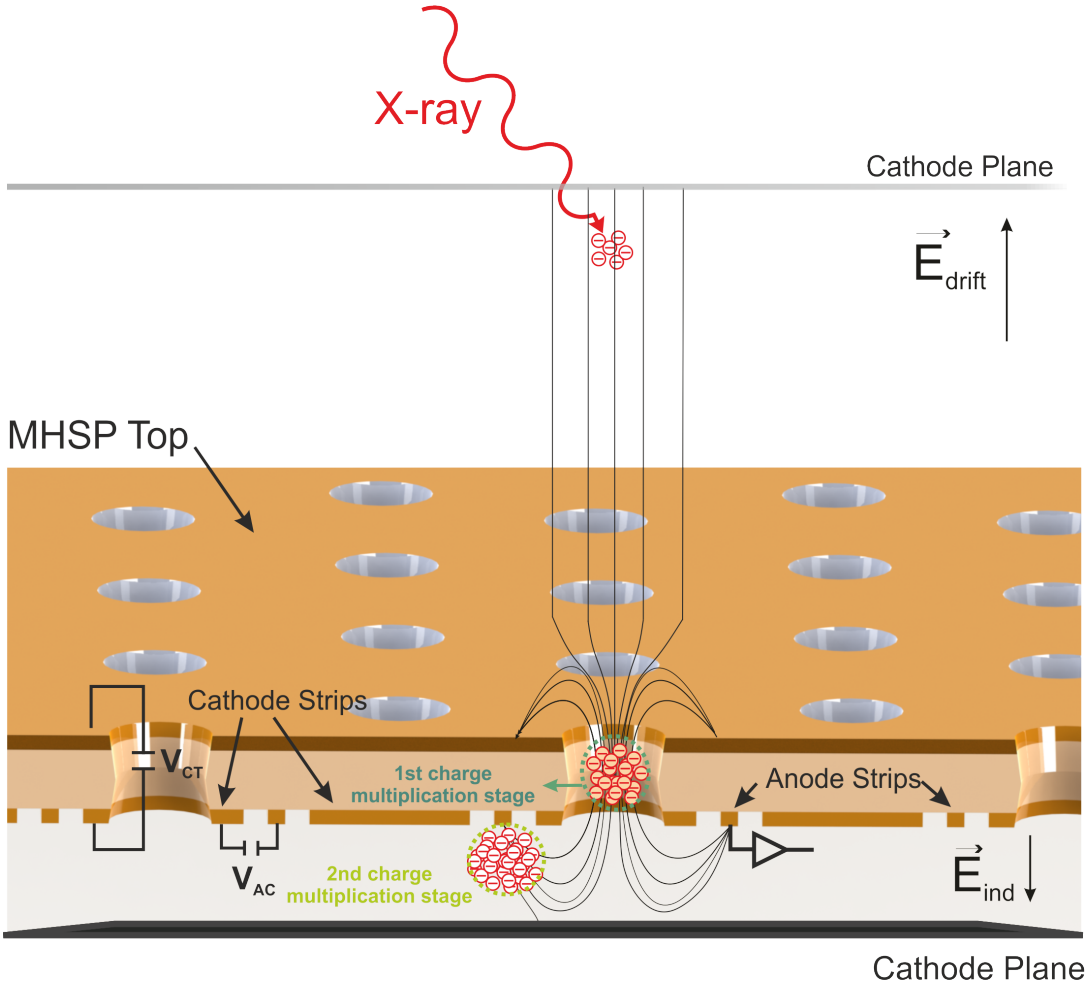

Figure 2.8: The working principle of the MHSP.

As in the GEM structure, the photon-feedback is avoided by its closed geometry. Furthermore, the ions created in the second avalanche that occurs near the anode strips are efficiently collected in the cathode strips and also in the cathode plane bellow the microstructure, under the effect of a suitable electric field, called induction field, $\vec{E}_{ind}$. The ion-backflow, i.e., the fraction of ions that travels back into the holes, including the ones that are created in the hole-avalanche and tend to go back to the drift region are trapped at the top electrode, avoiding the occurrence of space-charge effects in the drift region.

It has been shown that the MHSP presents very good stability, being capable of operate at very high charge gain ($> 10^4$) and at counting rates up to 5×10^5 Hz/mm^2 [58, 59]. An energy resolution of about 14 % at 5.9 keV was obtained in pure Xenon [59].

The standard MHSP was originally designed for X-ray and neutron detection [60, 61]. However, its versatility and interesting features as a single photon counting detector revealed other possible applications, as for example, X-ray imaging applications [62–64].

For 2D imaging some changes have to be introduced in the standard device, leading to the 2D-MHSP device [64]. In that case, one of the dimensions is achieved connecting the anode strips from the microstrip side through a thin resistive layer. To achieve the second dimension, the top electrode (GEM-like side) has to be structured in independent strips with a *zigzag*-shape perpendicular to the bottom strips on the opposite side. A resistive line is applied interconnecting those strips. The collection of the charge can be done from both ends of the resistive lines and, by using "centre of mass" algorithms, it is possible to determine the centroid of the distribution of the electron avalanche. For more details on the 2D-MHSP and on the 2D operation principle of the detector please see section 3.1.1.5.

A spatial resolution of $\sigma_y = 130$ μm and $\sigma_x = 250$ μm was achieved for 8 keV, making the MHSP based detector suitable for photon counting X-ray imaging [64].

Since the MHSP detector allows to discriminate, together with the interaction position, the energy information of each photon that interacts with the structure, it is also suitable for Imaging X-ray Fluorescence Spectroscopy applications. Studies have been performed, in 2009 in the framework of cultural heritage analysis in ceramic pieces from the XVIII century (Santa-Clara-a-Velha monastery, in Coimbra) [65].

2.2.2.4 Thick-Electron Multipliers and the Thick-COBRA

Thick-GEMs (THGEMs) are, as the name implies, thicker GEM structures. This kind of thick GEM electron multiplier was recently introduced by Chechik, *et al.*, in 2004 [66]. The substrate of the THGEM consists of a 0.4 - 1 mm thick Cu-plated G-10 Printed Circuit Board (PCB). The 0.3 - 1 mm diameter holes are produced by precision mechanical drilling in the substrate, which is covered with a thin copper layer (≈ 50 μm) on both sides. The hole pitch is usually between 0.7 - 1.2 mm. Between the edge of the drilled hole in the PCB and the edge of the holes of the etched copper, a gap of 0.1 mm is chemically produced - rim - in order to increase the stability and allow higher charge gains, reducing discharge probability [67, 68]. The rim is the main difference between the GEM and the THGEM in terms of design.

The THGEM has conquered its place among the other MPGDs quite fast, mostly due to its robustness and easiness of production. These structures can be produced in large quantities by using standard printed circuit board technology (using photolithographic masks) and are very cost effective.

Figure 2.9 shows a schematics of a THGEM structure. The holes are arranged in a honey-comb pattern, as in the standard devices (GEM and MHSP) shown before. Gains between 10^3 and 10^4 were obtained for different noble gases and gas mixtures [67]. To further increase the charge gain it is possible, as in GEM structures, to use cascade configurations

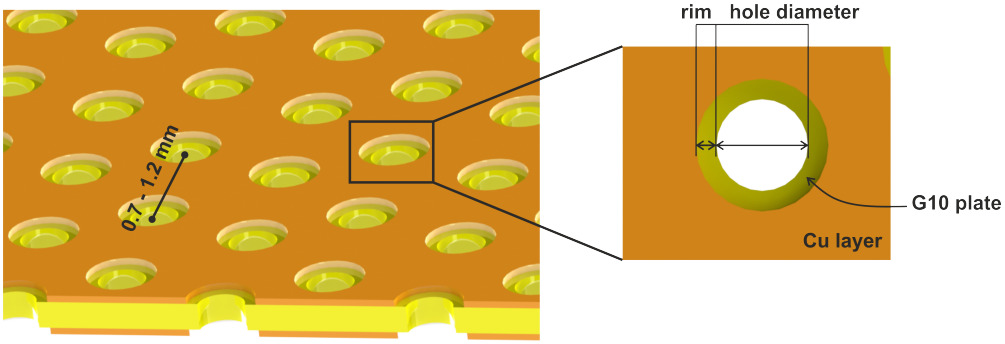

Figure 2.9: Schematics of a THGEM structure. The detail view of one of the holes shows the chemically etched rim, which is very useful for preventing discharges at high potentials.

of two or more THGEMs, which will have a positive influence in the detector stability, due to the more moderate voltages applied to each [67, 69–72]. Ref. [73] presents an interesting discussion on that, showing a study based on the comparison between a single, double and triple THGEM based detector, in terms of gain. For a triple THGEM configuration gains $> 10^5$ were achieved for Ne mixtures (at 1 atm) and a counting rate of 100 Hz/mm^2, for 9 keV X-ray photons. Active areas of about 30×30 mm^2 or 100×100 mm^2 are usually considered.

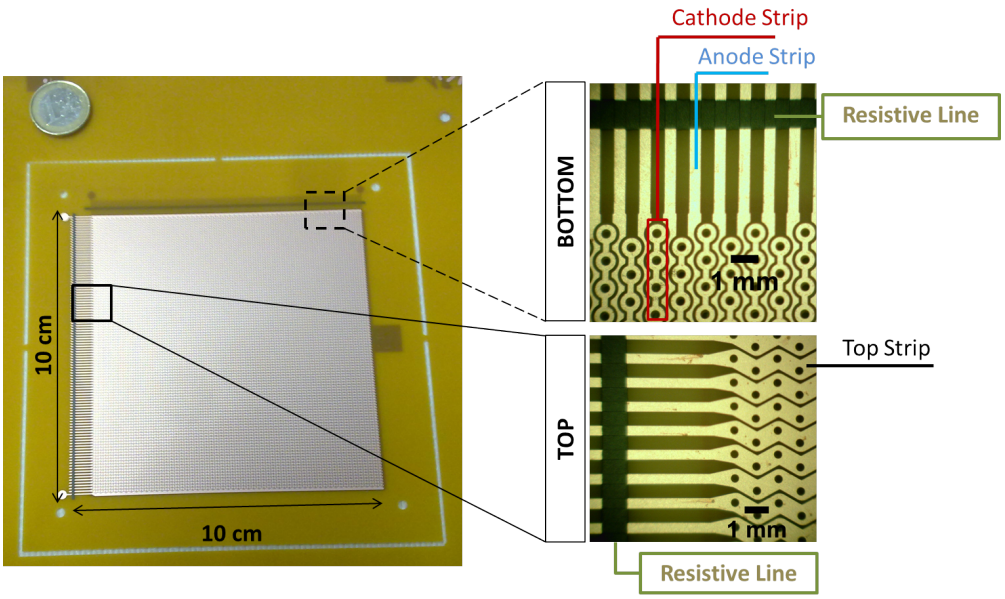

Figure 2.10: Photo of a 10×10 cm^2 position sensitive THCOBRA. Detailed view of the top and bottom side of the micro-hole structure.

Following the success of the MHSP and of the THGEM structure, a new MPGD based on a similar concept was developed. The THCOBRA was introduced by Amaro, *et al.*, in

2010 [74]. Initially, it appeared as a thicker version of the MHSP as ion-blocking structure in cascaded detectors based in THGEMs.

This thick version of the MHSP combines features of both THGEM and MHSP structures, benefiting from the robustness, simplicity and easiness of production of the first structure and from the position discrimination with ion blocking capability together with the two charge multiplication stages of the second structure.

The name THCOBRA comes from the winding shape of THCOBRA cathode electrodes along the structure, which resembles a snake (in portuguese, cobra) (please see Figure 2.10 - bottom side of the structure).

Similarly to the THGEM structure, a pattern of holes in a hexagonal configuration is produced by mechanical drilling and a set of strips, anodes and cathodes, are etched using standard PCB technology following the same procedure applied to the MHSP, as shown in Figure 2.10.

The substrate of the first THCOBRA, with an active area of 30×30 mm^2 was made of a 0.4 mm thickness G10 plate. The cathodes, i.e. the electrodes that surround the holes, had a width of 0.1 mm. The rim is usually of about 0.1 mm. The gap between the cathodes and the anodes was 0.1 mm wide. The anodes had a width of about 0.3 mm [74].

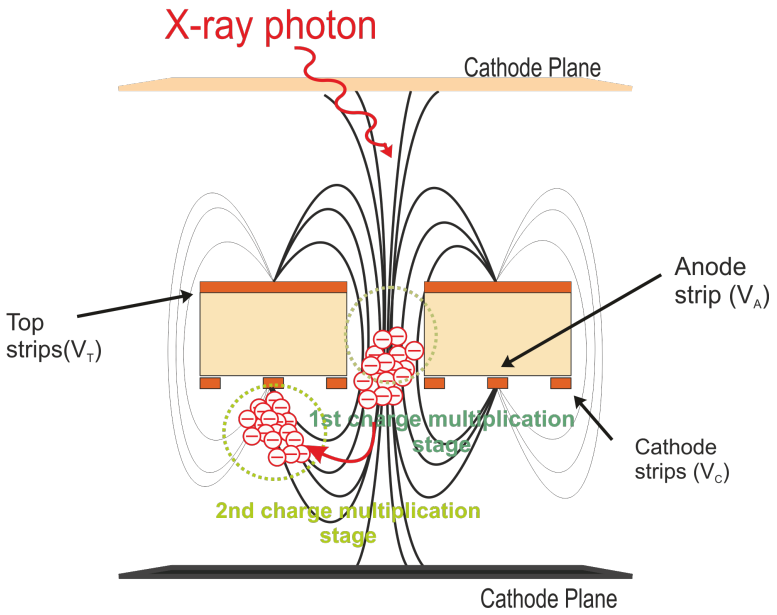

Figure 2.11: Schematics of the operation principle of the THCOBRA.

The structure was found to be very stable in terms of charge gain. Gains above 10^4 were achieved for gases such as: Ar, Ne and P10 mixture [74]. An energy resolution of 12.2 % FWHM was measured for X-ray energy photons of 22.1 keV and 19.2 % for the fluorescence K-lines of Cu, 8 keV [74].

Large area detectors are possible with these structures, up to 100×100 mm^2. Recently it was shown that this structure can be also employed for 2D-imaging by implementing some changes in the standard design. The top electrode can be structured in strips, orthogonal to the anode strips (second dimension), by using the same concept applied to the 2D-MHSP.

In this work, a THCOBRA with an active area of 10×10 cm^2 will be used for EDXRF applications (Figure 2.10). It is a double-sided structure made out of a 0.4 mm thick G10 plate, covered with 50 μm of copper on both sides. The THCOBRA has a 0.3 mm hole diameter, a pitch of 1 mm and a rim of 0.08 mm.

The operation principle of the THCOBRA detector is almost the same as that of the MHSP and is illustrated in Figure 2.11. The filling gas, Ne/5%CH_4, in the case of this work, acts as the absorption and multiplication medium. The first charge multiplication stage occurs due to the intense electric field in the holes, produced by the voltage difference between the cathode and the top strips, V_{CT}. By controlling the voltage difference between the circular-cathode strips and the anodes, a second multiplication stage can occur. The charge is collected at the anode strips V_{AC}.

CHAPTER 3

ENERGY RESOLVED X-RAY FLUORESCENCE IMAGING SYSTEM BASED ON MPGDS

As mentioned before in section 1.2.2, the Energy resolved X-Ray fluorescence (ER-XRF) imaging technique can be applied to determine the location of elements in samples, allowing to obtain elemental map distributions in materials of various natures, in a non-destructive manner, including archaeological and biologic samples, among others.

Different XRF imaging systems commonly used are based either on scanning systems or in full field-of-view systems usually based on solid state detectors. These kinds of systems were already discussed in detail in section 1.2.2. Table 1.2 presents an overview of some of the most important scanning and FF-XRF systems in the EDXRF imaging field, in an attempt to show more clearly the advantages and disadvantages of such systems.

Making a global comparison, most of the scanning systems show good position and energy resolution, although they usually need sample preparation and have some limitations of the sample size, in addition to the limitations inherent to the scanning complexity and time consuming.

On the other hand, systems based on pixel-detectors have good position and fair energy resolution although they present some limitations in the detection areas and in the complexity of the system for imaging readout.

As shown previously in chapter 2, the breakthrough of micropattern detectors related to their intrinsic position detection capability and storage of the energy information of each photon, possible in large detection areas, has shown excellent properties for single photon counting imaging [64, 75–77] and Energy Dispersive X-Ray Fluorescence (EDXRF) [77, 46] applications.

The physical operation principle of MPGDs does not allow for the excellent energy resolution presented by some other systems, but allows for fair energy resolution among a large number of features, namely:

1. Full field of view imaging operation (2D);
2. Absence of background due to the electronic noise (by setting a threshold);
3. In principle, unlimited dynamic range;
4. High rate capability (> 1 MHz/mm^2);
5. High soft X-ray (< 1 keV) detection capability, due to its high gain;
6. Room temperature operation;
7. Possibility of large detection areas ($> 10 \times 10$ cm^2);
8. Versatility and portability; and
9. Low cost

When the 2D detectors are coupled to a pinhole camera, the features of the MPGDs based systems compare favorably with other 2D based systems: feature 2, 3, 4, 6, 7, 8 and 9 with CCD based systems [14–16, 32]; 5, 7 and energy resolution with Medipix2 [17]. Although scanning based systems are different concepts from the ones based on MPGDs coupled to a pinhole, the latter, presents, in general, relative advantages in features 1, 4, 6, 7, 8 and 9 [25, 27–31].

This chapter aims to introduce the Energy Dispersive X-Ray Fluorescence imaging systems based on MPGDs developed during this work. Their main components, such as: the 2D detectors (2D-MHSP and 2D-THCOBRA) and the pinhole camera will be discussed in detail since their intrinsic characteristics are deeply related to the system performance.

Experimental Setup

As in the conventional Full-Field X-Ray Fluorescence systems, both Energy Dispersive X-Ray Fluorescence imaging systems developed during this work comprise three main components: an X-ray tube, X-ray optics (pinhole camera) and a 2D energy resolved detector (2D-MHSP and 2D-THCOBRA detectors). Figure 3.1 shows a schematics of the basic components of such a system as well as their geometric arrangement.

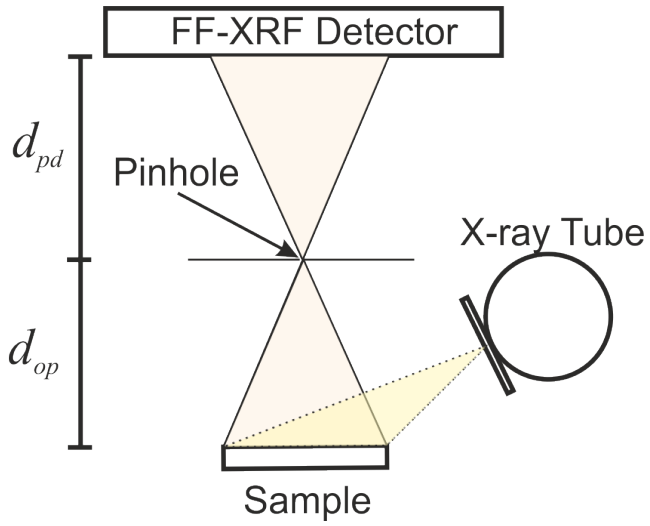

Figure 3.1: Schematic of the basic components of a FF-XRF imaging system, using a pinhole camera as X-ray optics device, as well as their geometric arrangement.

The X-ray tube must produce a broad beam, enough to irradiate a large part or the whole sample, at once. The X-rays emitted by the tube irradiate the sample surface with an angle close to 45°. The excited elements emit characteristic fluorescent X-ray photons upon relaxation, whose distribution can be imaged onto the detector via pinhole optics and detected

afterwards in the gas volume of the 2D-detector. Illustrations showing the experimental setups developed during this work are shown in the next chapter in Figures 4.1 and 4.11.

The pinhole camera is an aperture through which the fluorescence photons must pass in order to be seen by the energy dispersive detector. This device provides a cone-beam image incident into the detector with the focus point at the pinhole. This type of optical instrument combines the easy manufacturing with the possibility of image magnification, which allows, in terms of spatial resolution, overcoming the limits imposed by the intrinsic detector response. The influence and importance of the pinhole in the position resolution will be exploited in section 3.24.

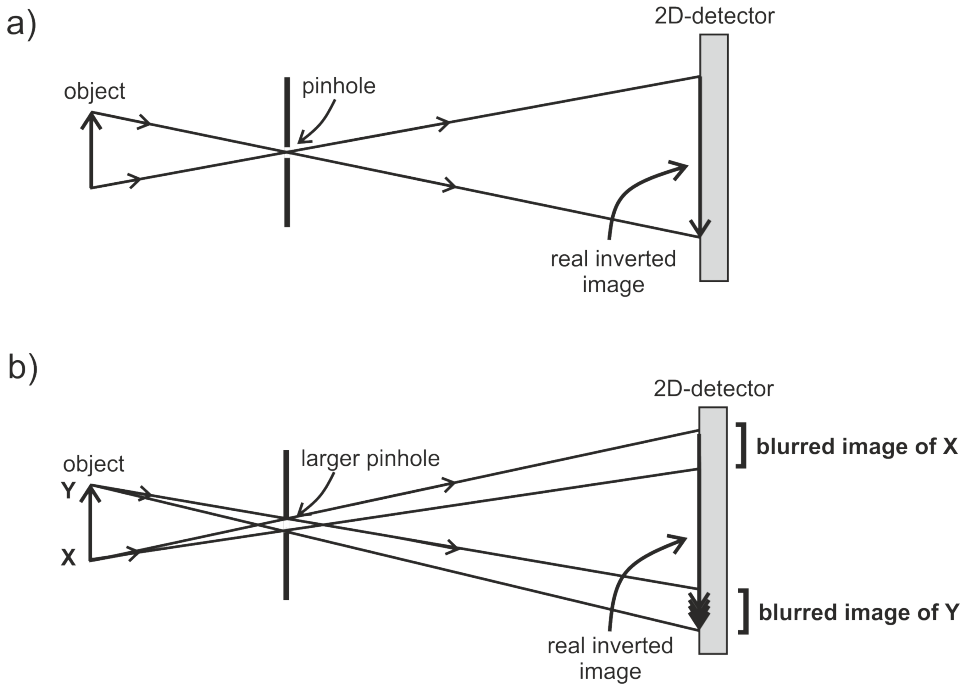

Figure 3.2: Diagram of a pinhole camera: a) Sharp image formed by a small pinhole; b) Blurred image formed by a large pinhole.

By using pinhole optics, a real inverted image is formed on the detector, as illustrated in the diagrams of Figure 3.2, with a magnification that depends on the ratio between the pinhole-to-detector (d_{pd}) and the object-to-pinhole distance (d_{op}). Thus the magnification, M, of the image is given by:

$$\mathrm{M} = \frac{d_{pd}}{d_{op}} \tag{3.1}$$

If a smaller pinhole is used, the obtained image is sharp (Figure 3.2 a)) because the projected circle at the image plane originated by a point-like X-ray source from the sample

is practically the same size as the pinhole. Instead, if the pinhole aperture is enlarged the image becomes blurred (Figure 3.2 b)) because a point-like X-ray source will produce a bigger/blurred spot in the image plane. The pinhole diameter influence in the system spatial resolution will be discussed in this chapter - section 3.24.

3.1 Detectors performance

Taking advantage of the good features in terms of gain, position and energy resolution of the MPGDs, two different systems for EDXRF imaging applications were developed, based on two different MPGD detector concepts, the 2D-MHSP and the 2D-THCOBRA.

Both detectors use a readout system based on resistive lines for position detection capability [64, 78]. Although they present a very similar operation principle (see section 2.2.2), they present very different effective detection areas (2.8×2.8 mm^2 for the 2D-MHSP and 10×10 cm^2 for the 2D-THCOBRA) and granularity, which makes them very different in terms of characteristics.

Both detectors were built and studied independently. In this section the characteristics of these detectors will be exploited since they present the major novelty in the system developed for EDXRF imaging purposes.

3.1.1 2D-MHSP detector

The 2D-MHSP detector used in this work consists of a aluminium vessel containing the 2D-MHSP structure inside, in a Xe atmosphere, at 1 bar. The microstructure was introduced previously in the section 2.2.2. The bi-conical holes are of about 50/60 μm in diameter, disposed in a hexagonal pattern. The width of the cathode and anode strips, placed in the MSGC-like side, is 100 μm and 20 μm, respectively, with a pitch of 200 μm. The top strips exhibit a *zigzag*-shape due to the hexagonal distribution of the holes, and are disposed orthogonally to the anode strips, as illustrated in Figure 3.3.

Figure 3.4 shows the detector used for the experiments described in this work. Inside of the aluminium vessel the 2D-MHSP is fixed by stainless-steel feedthroughs, which are used for the electrical biasing of the electrodes. These connectors also allow the microstructure to be stretched at a certain distance from the detector body (2 mm). The electrical connectors are glued to Macor® ceramic cylinders to isolate the high voltage needed to polarize the microstructure. The Macor® is also glued to the detector body. The insulating epoxy used has low vapor pressure - Trabond® 2116 [1]. The choice of low out-gassing materials is an essential point to keep the gas as pure as possible inside the sealed detector, which is very important to achieve better detector performance in terms of energy resolution.

[1] Hysol Tra-Bond 2116 'Low Vapor Pressure Epoxy Stalking Compound': www.henkelna.com/product-search-1554.htm?nodeid=8797850337281

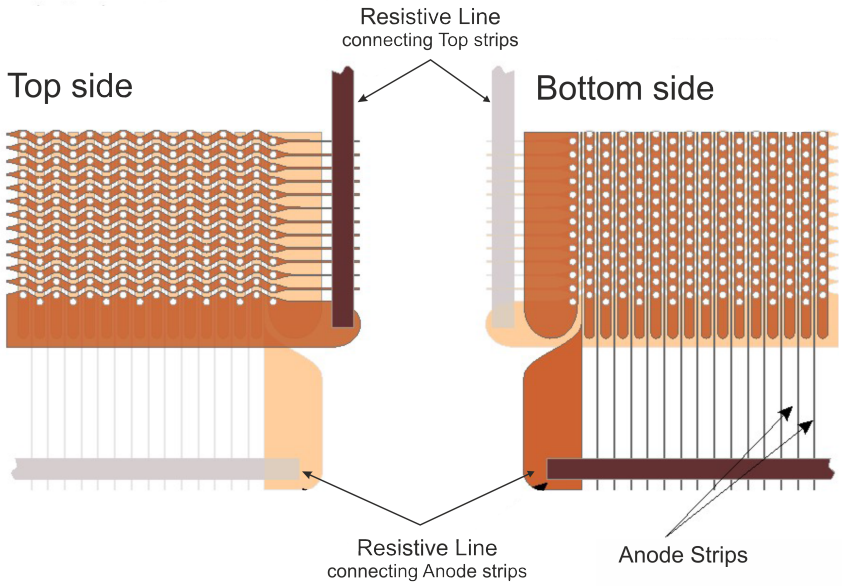

Figure 3.3: Top and bottom view of the 2D-MHSP detector. Adapted from [63, 79].

The detector window is made of a 75 μm Kapton® foil and has an area of 3×3 cm^2. On the bottom side of the window it was deposited by evaporation, of a thin layer of aluminium. The detector window serves also as the drift cathode. The drift region is 3 mm deep and the bottom of the 2D-MHSP is placed 2 mm away from the detector body, as can be seen in the schematics presented in Figure 3.4 a).

In a first approach the detector was used without any purifying system (Figure 3.4 b)). this implies that the gas inside had to be changed every two days, otherwise the energy and position resolution performance was poor, not allowing to perform measurements. Nevertheless, during these two days the detector performance was found to be very stable.

At a certain point it was decided to include a purifying system (Figure 3.4 c)) in order to continuously purify the Xe (99.999 %) after filling the detector. The purifying system was based in ST707/WASHER/833 SAES getters [2] . The non-evaporable getters are located inside a metallic container which is coupled to the detector through an *in/out* connection. The getters must be activated by temperature ($\approx 350°C$), using a heating tape, connected to a temperature controller. Then, to promote the gas circulation between the detector and the getters container by convection, it was necessary to program the temperature controller to do cycles of temperature ranging between the room temperature (around $22°C$) and $200°C$.

The inclusion of the getters in the detector system improved a lot its working conditions, increasing the operation time of the detector without changing the gas (about 15 days). Despite all of these improvements, we are aware that the purification system can be further

[2]The datasheet of the ST707/WASHER/833 SAES getters can be found at: http://psec.uchicago.edu/getters/St%20707%20Brochure.pdf

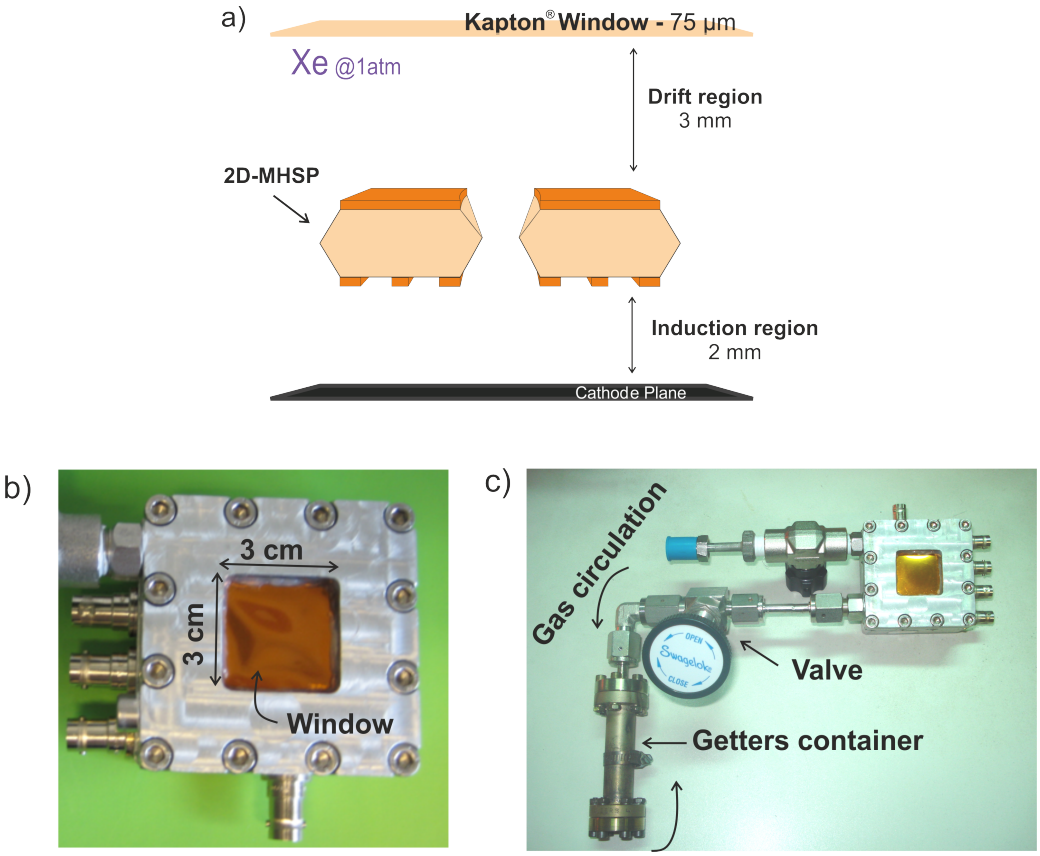

Figure 3.4: 2D-MHSP detector used in the experiments performed during this work. a) Detector layout diagram. The microstructure is placed at 3 mm from the window (drift region) and 2 mm from the detector body; b) Photo of the detector; c) Detector using a purifying system based on getters. To promote the gas circulation between the detector and the getters container by convection, a heating tape connected to a temperature controller is used to do cycles of temperature ranging between the room temperature (around 22°C) and 200°C.

improved. For example it is usual to place the getter container connected to the detector via two *in* and *out* independent connections, creating a closed circuit through which the gas circulates in only one direction by convection. In this case the getters should be continuously at a temperature close to $200°C$ to promote the gas circulation. This kind of connection should promote a more efficient purification than the one achieved with our system, but so far it does not appear to be essential to modify the system. However, it can be done in the future, as a further detector improvement.

3.1.1.1 Detection efficiency

The absorption/drift region of the detector (3 mm wide) and the Kapton® window (75 μm thick) limit the detection efficiency of the detector. In the case of this work the detector was thought for EDXRF imaging applications, thus, the detection efficiency of the detector

must be as high as possible for the characteristic energies of the elements that we are more interested in.

Figure 3.5 shows that photon energies below 2 keV are almost completely absorbed by the 75 μm Kapton® used in this detector. The thickness of the window was chosen to ensure that the depth of the absorption/drift region is as constant as possible and also due to it robustness, which is needed to withstand pressure changes, performed when the detector is placed under vacuum before filling it with the gas.

The total absorption curve was determined multiplying the energy transmission curve of the Kapton® window by the energy absorption curve for the 3 mm gap of Xe.

The highest detection efficiency region of the detector is achieved for energies between 5 and 10 keV, since the transmission in the Kapton® is very high, between 78 and 98 % and the absorption in Xe is still reasonable.

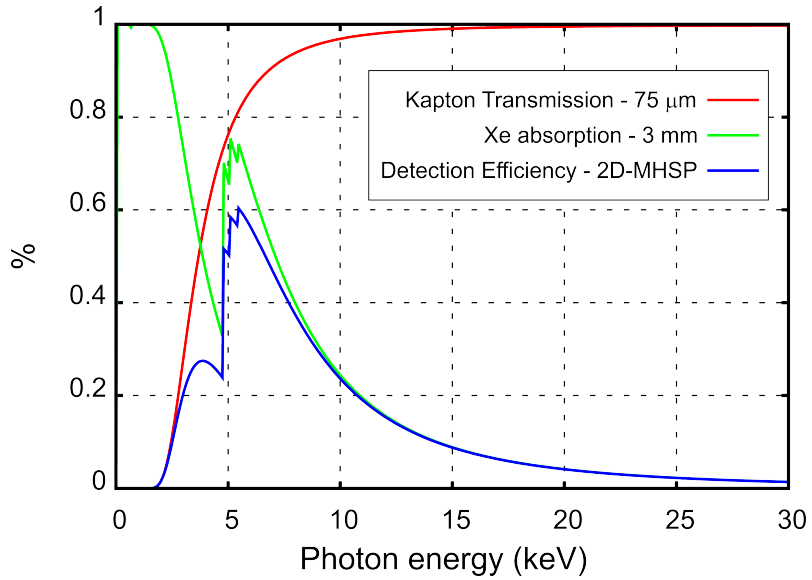

Figure 3.5: Detection efficiency curve of the detector, transmission curve of the 75 μm Kapton® window and absorption curve of Xe, for a drift region of 3 mm, as a function of the incident energy. Data used for the detection efficiency calculation was taken from [80].

The knowledge of the detection efficiency as a function of the incident energy is particularly important in X-ray fluorescence studies. The raw fluorescence spectrum obtained by irradiation of a multi-element sample does not carry any information about the ratio between the intensity of the different spectrum peaks. Therefore, by knowing the detection efficiency curve it is possible to do a correction based on the efficiency of the detector and obtain the relative intensities of the various spectrum peaks.

3.1.1.2 Energy resolution and linearity

For imaging X-Ray fluorescence spectroscopy measurements it is essential to measure the energy distribution of the incident radiation. Thus, one of the most important properties of the detector in radiation spectroscopy is the energy resolution. The energy resolution of a detector can be inferred from its response to a mono-energetic source of radiation. Due to fluctuations of different sources, the pulse height distribution obtained is not a delta function but a Gaussian distribution. The FWHM of the distribution is deeply related to the amount of fluctuations occurring, and therefore to the best energy resolution possible.

Usually, the energy resolution is measured in percentage, since it corresponds to a dimensionless fraction, defined as the FWHM divided by the peak centroid (mean value) of the Gaussian distribution.

The standard deviation, σ, of a Gaussian probability distribution is related to the FWHM through the relation: FWHM$= 2\sqrt{2ln(2)}\sigma \approxeq 2.35\sigma$.

In a MPGD, each primary electron produced by the interaction of the radiation with the gas medium undergoes a multiplication process, called avalanche, giving rise to a number of charges equal to A. The final gain M, is defined as the average multiplication factor of all of the individual avalanches (A_i) contributing to a given pulse whose amplitude is proportional to the final charge Q, as explained before in section 2.1:

$$M = \overline{A} = \frac{1}{N_p}\sum_{i=1}^{N_p} A_i \tag{3.2}$$

The final charge Q can be assumed as the sum of the charges created in each avalanche,

$$M = \frac{Q}{eN_p} \Leftrightarrow Q = N_p e M \tag{3.3}$$

Where e is the charge of the electron. This final charge is subject to fluctuations from pulse to pulse, which are due to fluctuations both in the formation of the primary electrons and also in the gain, even if the incident radiation is mono-energetic. Thus, the relative variance of the final charge $(\frac{\sigma_Q}{Q})^2$ can be written as:

$$\left(\frac{\sigma_Q}{Q}\right)^2 = \left(\frac{\sigma_{N_p}}{N_p}\right)^2 + \left(\frac{\sigma_M}{M}\right)^2 \tag{3.4}$$

Assuming each avalanche as an independent process it is possible to apply the error propagation formula to eqn. 3.2 and obtain:

$$\sigma_M^2 = \frac{1}{N_p}\sigma_A^2 \tag{3.5}$$

Where A is the typical avalanche magnitude. Thus, eqn. 3.4 can be rewritten as shown in eqn. 3.6, showing both the ion-pair fluctuations contribution plus the single electron multiplication variations:

$$\left(\frac{\sigma_Q}{Q}\right)^2 = \left(\frac{\sigma_{N_p}}{N_p}\right)^2 + \left(\frac{1}{N_p}\right)\left(\frac{\sigma_A}{\overline{A}}\right)^2 \tag{3.6}$$

The ion-pair fluctuations were already discussed previously in section 2.1, and can be expressed in terms of the Fano factor F. The relative variance is given by:

$$\left(\frac{\sigma_{N_p}}{N_p}\right)^2 = \frac{F}{N_p} \tag{3.7}$$

Concerning the single electron avalanches, the relative variance of A, which is related to the gas amplification originated by an electron, can be described as:

$$f = \left(\frac{A - \overline{A}}{\overline{A}}\right)^2 = \left(\frac{\sigma_A}{A}\right)^2 \tag{3.8}$$

Substituting eqn. 3.7 and 3.8 in eqn. 3.6, we obtain the relative standard deviation of the pulse amplitude distribution:

$$\left(\frac{\sigma_Q}{Q}\right)^2 = \frac{1}{N_p}(F + f) \tag{3.9}$$

Thus the intrinsic energy resolution R_{energy} of the detector can be obtained:

$$R_{energy} = 2.35 \times \frac{\sigma_Q}{Q} = 2.35 \times \sqrt{\frac{F + f}{N_p}} \tag{3.10}$$

Since $N_p = E/W$, where E is the energy of the incident radiation, and W the W-value of the gas (section 2.1), we can rewrite eqn. 3.10 as:

$$R_{energy} = 2.35\sqrt{W(F + f)} \times E^{-1/2} \tag{3.11}$$

The statistical limit of the energy resolution is thus inversely proportional to the square root of the incident radiation energy.

The quantity $\sqrt{W(F+f)}$ is constant for a given filling gas at a given gain. Thus, for a given energy the limiting resolution is proportional to that quantity. Fano factor is usually smaller than f, for typical operation conditions [7], which means that the energy resolution of gaseous detectors using charge multiplication is often limited by the inherently large fluctuations in the size of the avalanches created by each primary electron [7, 81]. It was found that detector geometries such as the MPGDs, that allow higher gradient of electric fields, lead to lower statistical fluctuations, compared to other proportional counters [7, 81].

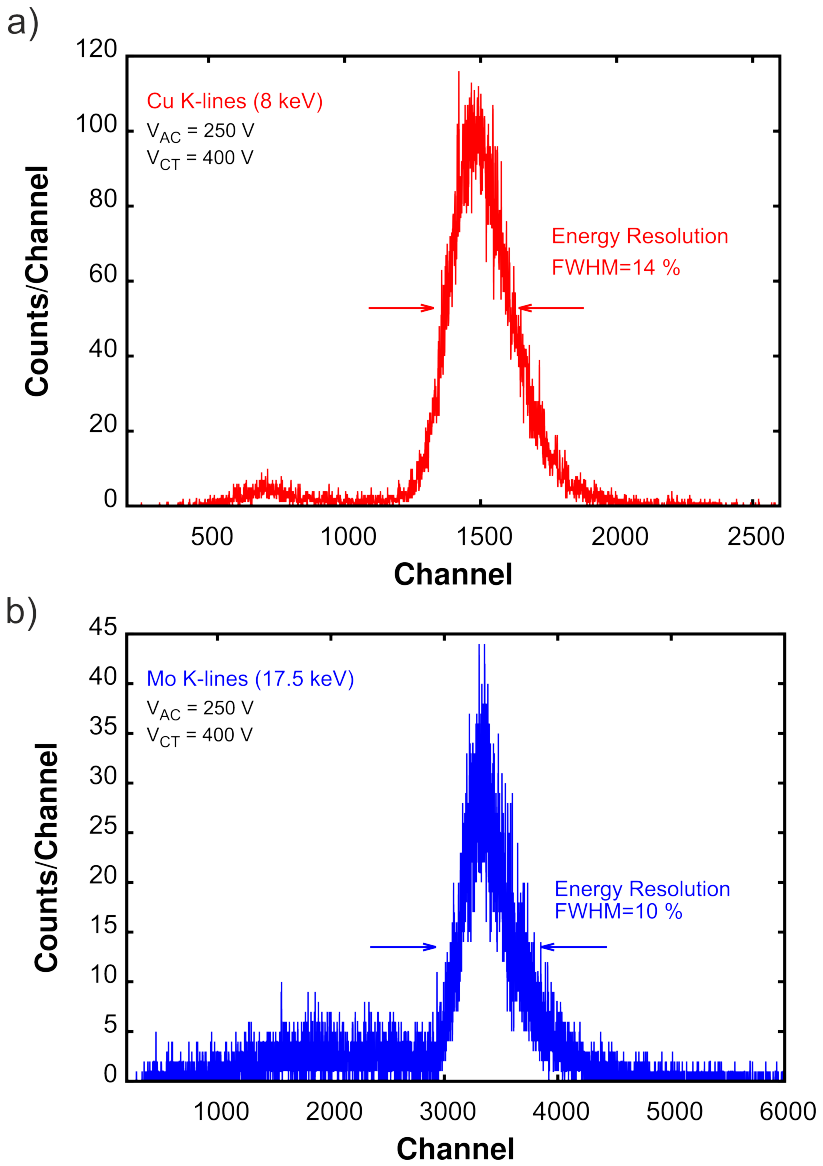

Figure 3.6: Pulse-height distributions of K-lines from: (a) Cu and (b) Mo [82].

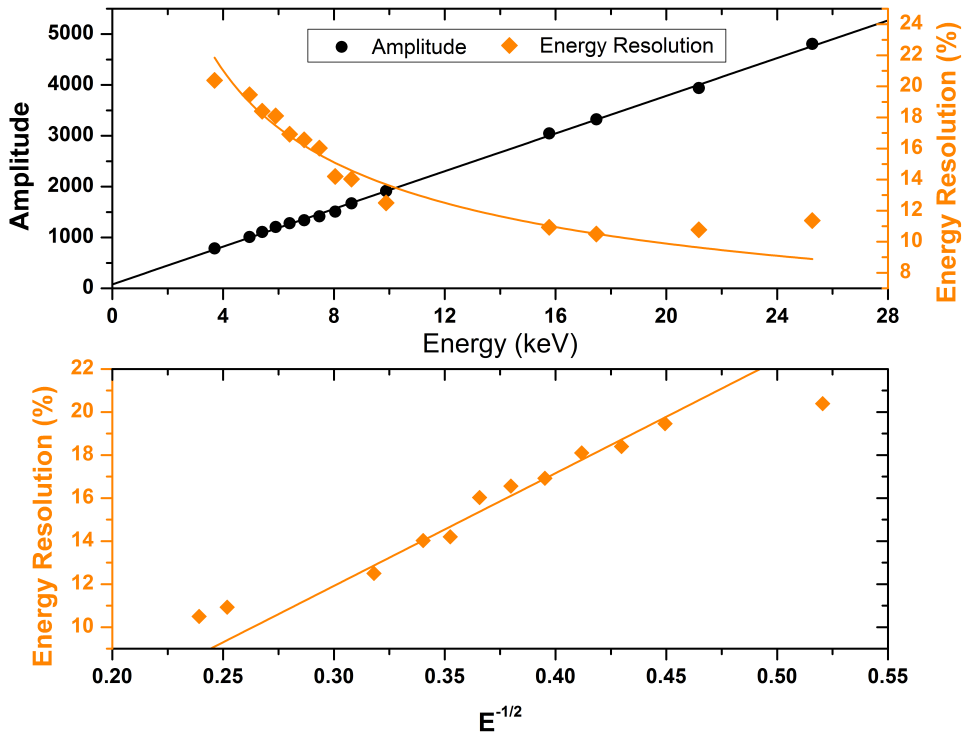

Figure 3.7: a) Pulse amplitude and energy resolution as a function of X-ray energy; b) Energy resolution as a function of the inverse of thesquare root of the energy of the incident radiation [82].

To evaluate the capabilities of the detector for X-ray spectrometry, the energy linearity of the 2D-MHSP detector was determined, for X-ray energies ranging from 3 to 25 keV. The fluorescence radiation was obtained by irradiation of different single-element targets including pure elements, oxides or salts, such as: Ca, V, Cr, Mn, Fe, Co, Ni, Cu, Zn, Ge, Zr, Mo, Pd e Sn. The time of acquisition was typically 30 s. As an example, the Cu and Mo K-lines spectra can be seen on Figure 3.6.

During acquisitions, the sample-to-detector distance was typically 20 cm. The detector window was coupled to a lead collimator with a 2 mm diameter hole drilled on it. Fluorescence radiation was induced by X-rays from an X-ray molybdenum tube from Oxford Instruments®[3] by using different currents and voltages depending on the analysed sample.

In Figure 3.7 a) the pulse amplitude (the centroid of the peak distribution) and the energy resolution values of the measured pulse-height distributions are plotted as a function of the energy of the incident radiation. As expected, good energy linearity is maintained throughout the measured energy range. The energy resolution shows also a reasonable linearity with $E^{-1/2}$, as illustrated in Figure 3.7 b). Since the points corresponding to the photon energies

[3]Oxford Instruments® - series 5000 Apogee- URL: http://www.oxford-instruments.com/

of 3.7, 21.2 and 25.3 keV are completely out of trend, it was decided not to consider them when fitting the data. The results are in agreement with the typical behaviour of the proportional counters, where R_{energy} varies linearly with $E^{-1/2}$. There is a good approximation of the straight line fit to the experimental points ($r^2 = 0.965$), which is expressed by the eqn.:

$$R_{energy} = (5.2 \pm 0.4) \times 10E^{-1/2} - (0.4 \pm 0.1) \times 10 \tag{3.12}$$

Therefore, from this equation can be inferred, within the energy (in keV) range studied, the energy resolution for any incident radiation energy.

A spectrum was also acquired by direct irradiation of the detector with a ^{241}Am γ source (Figure 3.8), using the 2 mm collimator. The energy resolution obtained for the 60 keV photons was of about 7 %.

From the ^{241}Am pulse-height distribution acquired (Figure 3.8) it is also possible to evaluate the detector energy dynamic range. The spectral features include the fluorescence L-lines from Neptunium (respectively 13.95, 17.74 and 20.78 keV), the 59.6 keV peak from ^{241}Am γ-rays and other fluorescence lines associated with the experimental setup (Pb from the collimator and Xe escape lines). The spectrum clearly shows the detector intrinsic high energy dynamic range.

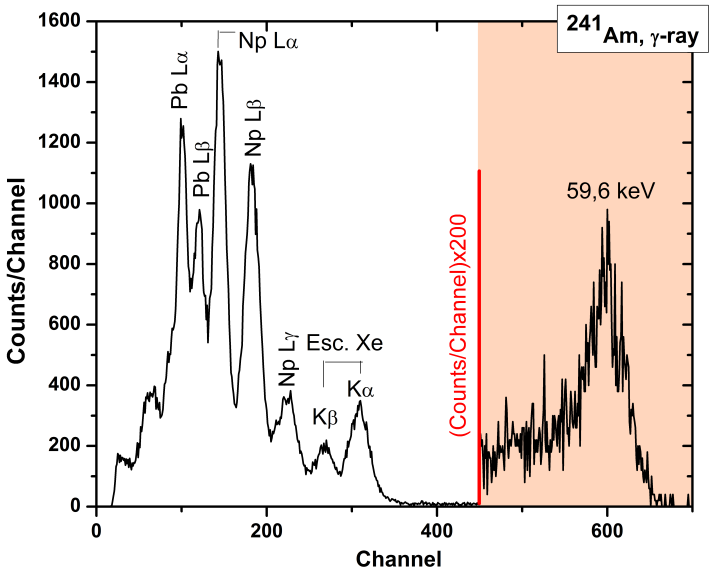

Figure 3.8: ^{241}Am pulse-height distribution [82].

Although energy resolution behaves as expected, the obtained values are still worse than the intrinsic energy resolution of the detector. It is known that the amplitude response as a function of interaction position in the detector is not a constant value for monochromatic radiation photons. This is due to the different response along the microstructure because of the non-uniformities resulting from the fabrication process which leads to a deterioration of the energy resolution. To overcome this problem an amplitude correction method was developed, which will be explained in the next section - Amplitude Correction Method.

3.1.1.3 Amplitude Correction Method

The Amplitude Correction Method was previously developed and is described in detail in ref. [83] and emerged in an attempt to minimize the deterioration of the energy resolution induced by small variations in the size of the electrodes (hole diameters and strip widths) and other small defects over the microstructure active area resulting from the photolithography during the production process. This means that if we irradiate the detector with a mono-energetic radiation, the pulse height distribution response is different from pixel to pixel causing a peak broadening in the total spectrum and thus, worsening energy resolution. This amplitude non-uniformity along the detector area can be corrected by using a flood image, produced by irradiation of the full active area of the detector with mono-energetic X-ray photons (usually, fluorescence photons). This flood image give us the intensity distribution of the detector area, but contains also information on the pulse amplitudes of the mono-energetic detected photons.

The detection area is then divided into small active sensing elements, each one corresponding to an element-area of the detector. From the pulse height distribution for each element-area, the respective peak centroid can be determined by fitting a Gaussian function to the peak.

In this way it is possible to build a P_{ij} matrix containing the peak centroid for each element-area. Taking as reference the average of all peak centroids, $R_{peak} = \sum P_{ij}/(n \times m)$, where $n \times m$ is the number of elements of the matrix P_{ij}, a correction matrix C_{ij} can be built as follows:

$$C_{ij} = \frac{R_{peak}}{P_{ij}} \tag{3.13}$$

Therefore, during data acquisition, all the amplitudes of the pulses produced in the each element-area ij are multiplied by the correction factor C_{ij}, according to the equation:

$$M_{ijE_{corr,k}} = C_{ij} \times M_{ijE_k} \tag{3.14}$$

The M_{ijE_k} matrix is related to the raw data obtained by the acquisition board and contains information about the energy of each photon (E_k) as well as its interaction position within the detector. The matrix $M_{ijE_{corr,k}}$ differs from the matrix M_{ijE_k}, because it contains the corrected energy information.

For further details about the amplitude correction method, including application examples and validation of the method please see references [83] and [84] .

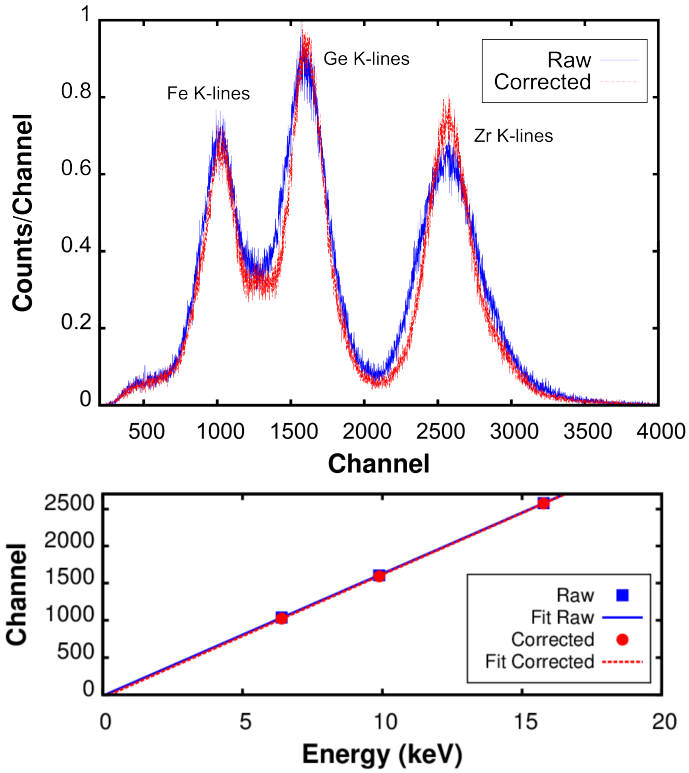

Figure 3.9: *Top*: Raw and corrected pulse-height distributions from a Fe, Ge and Zr sample; *Bottom*: Raw and corrected pulse amplitude as a function of the X-ray energy [82].

The correction method gives a clear improvement in the energy resolution, as can be seen in Figure 3.9, in the three-element sample example. For energies of 9.89 and 15.77 keV, an improvement in the energy resolution of 17% and 24%, respectively, was obtained in comparison with the non-corrected one. This spectrum was obtained irradiating the whole active area of the detector.

The ratio between the intensity of the peaks in the energy spectrum of the sample of three elements (Fe, Ge, Zr) does not match with the relative intensity of emission of the various constituting elements, since the detection efficiency of the detector varies with incident

radiation energy, as was explained before.

Concerning the energy linearity, the amplitude non-uniformity, i.e., the shift of the energy peaks from one region to another, does not affect much the detector energy linearity, as can be seen in Figure 3.9.

3.1.1.4 Gain and count rate performance

The performance of the MHSP electron multiplier, has been studied since it was developed, in 2000, by Veloso, *et al.* [57]. In 2005, Natal da Luz, *et al.* [59] published a paper reporting its operation in pure Xe at atmospheric pressure.

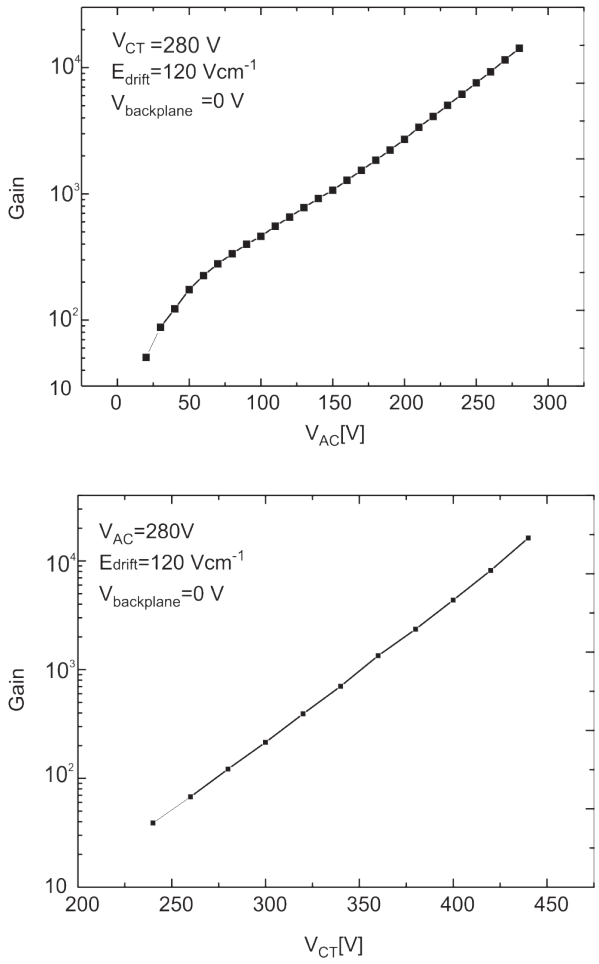

Figure 3.10: Absolute gain achieved with the MHSP detector as a function of: *Top* - V_{AC}; *Bottom* - V_{CT}. Adapted from [59].

Figure 3.10 shows the absolute gain achieved with the MHSP detector, for 5.9 keV X-ray photons, as a function of the potential difference, V_{AC}, between the anode and cathode strips, and as a function of the potential difference across the holes, V_{CT}. Gains of about 2×10^4 were obtained, which is a very good result for imaging applications. The results described in

the paper also show a stable operation in terms of gain in pure Xe atmosphere.

One of the main interests when developing radiation detectors is related to their capability to work at high counting rates, for instance, with synchrotron radiation beams. In all of the MPGDs the maximum achievable gain drops with the count rate. Besides that, for a given gain, the increase of the count rate, at high count rates, causes the gain to drop.

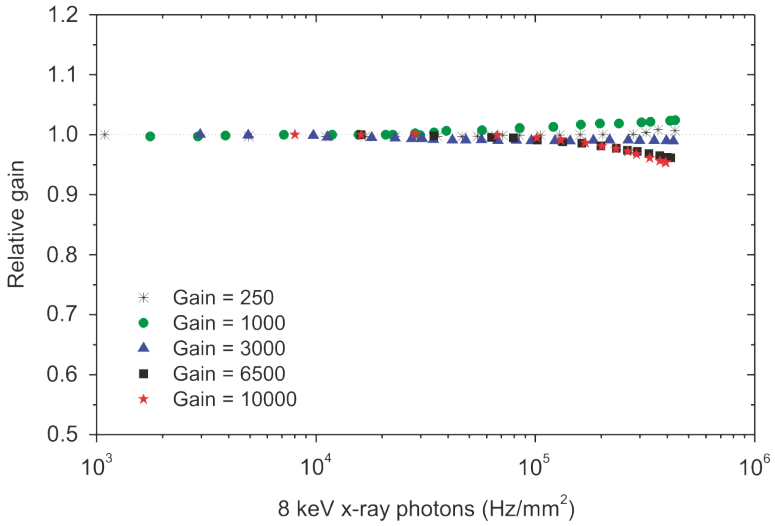

Figure 3.11: Relative gain as a function of the detector output count rate, for different absolute gains of the MHSP [58].

The performance of the MHSP operating under a high flux radiation of 8 keV X-rays was investigated in 2007 by Veloso, *et al.* [58]. The relative gain of the detector obtained as a function of the detector output count rate is presented in Figure 3.11.

The MHSP has demonstrated stable operation for count rates up to 0.5 MHz/mm^2 for gains of 10^4. For count rates up to 0.1 MHz/mm^2 the detector gain, as well as the energy resolution, were maintained. However, for count rates above 0.5 MHz/mm^2 and gains $> 10^4$ some small variations (about 5 %) on the gain were observed. In the same paper, studies of the energy resolution at high gains for high count rates were also performed. It was shown that the FWHM energy resolution of the detector degrades from 16% to 18% when increasing the count rates from 0.1 MHz/mm^2 to 0.5 MHz/mm^2.

3.1.1.5 Imaging capability and position resolution

Proof of principle

As mentioned briefly in section 2.2.2.3, for 2D-imaging, the GEM-like side (top side) of the standard MHSP is structured with anodes orthogonally disposed to the MHSP-like microstrips on the bottom side (Figure 3.12). Two thin orthogonal resistive lines simple to

apply by serigraphy connecting the top strips (top side) and the anode strips (bottom side) allow obtaining the interaction position in both X- and Y-directions of the X-ray photons.

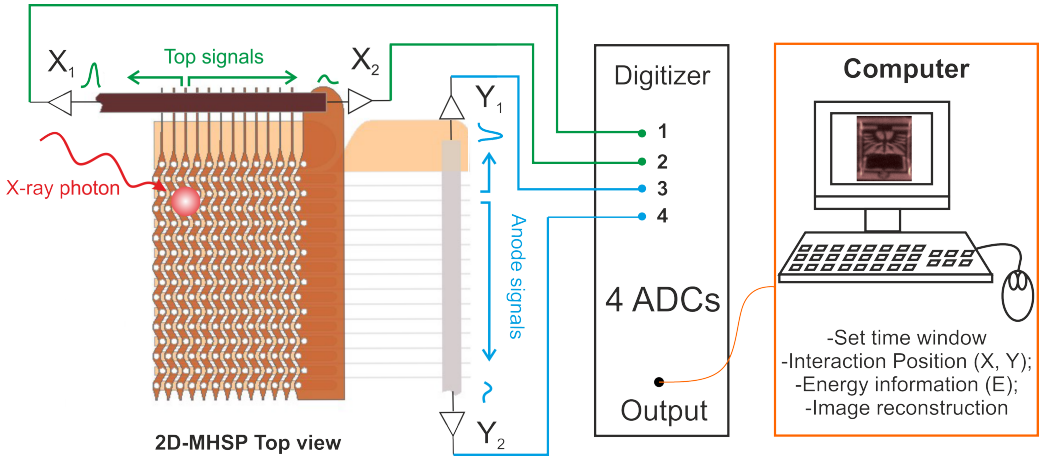

Figure 3.12: Schematic of the 2D-operation principle of the MHSP detector. Adapted from [63].

The signals collected on the top strips are induced by the charge moving towards the anode strips. Thus, the MHSP structure is usually treated as a capacitor in which the Kapton® foil is the dielectric material.

The resistance of each resistive strip depends on its length, and can be expressed as:

$$R = \frac{\rho l}{A} \tag{3.15}$$

Where l is the length of the strip, A is its the cross sectional area and ρ is the resistivity of the material.

The charge deposited on the strips from the top and from the anodes is collected from both ends of each resistive layer, being the charge division processed in accordance to the resistance between the respective microstrips and the resistive line ends [63]. Therefore, to the closest end of the resistive line will arrive a signal greater in amplitude than to the other end. Thus, through the ratio between these amplitudes is it possible to determine the centre of the electron avalanche distribution, in the cartesian coordinate system [63]:

$$X = k\frac{X_1}{X_1 + X_2} \tag{3.16}$$

$$Y = k\frac{Y_1}{Y_1 + Y_2} \tag{3.17}$$

Where X_1 and X_2 are the amplitudes of the charge signals collected in the X direction, Y_1 and Y_2 are the amplitudes of the charge signals collected in the Y direction, and k represents a calibration factor. X and Y are the measured positions of the interaction of X-rays within the 2D-MHSP detector.

The main advantage of a resistive divider is the good linearity obtained between the signal fraction measured and the position. This linearity is only limited by the uniformity of the resistive line, i.e., by the accuracy of the resistive divider. Although the position linearity is maintained, when the total resistance is higher, the capacitance of the structure introduces some phase shifts and propagation delays at high frequencies along the signal path reducing the high rate capability of the imaging system and introducing some distortions on the measured signal amplitude [85]. These distortions become larger as the charge delivery position is farther away from a given end of the resistive line [79]. To minimize such effects, the resistor values should be chosen relatively low, however low-value resistors also increase the amount of noise, leading to a deterioration of the position resolution of the detector. In our case, between consecutive electrodes (microstrips) the resistance is about 50 Ω.

By summing the amplitudes of the charge signals collected in one direction, X or Y, it is possible to assess the energy information of a photon that interacts with the detector. Usually the signals corresponding to the anodes direction (Y) are the ones used to determine the energy of the photon. This is because the amplitude of these signals is 40 % of the amplitude of the signals directly read from the anode strips [63].

This kind of readout system based on resistive lines is very simple and cost effective since it uses only four pre-amplifiers. For signal processing, a NIM module N1728 from CAEN was used, with a 4-channel, 14 bit, 100 MHz ADC card. The signals were digitally shaped and amplified by applying the Jordanov trapezoid algorithm [86] to determine the signal amplitudes. After being digitized the signals are processed with a computer, by using a program called Radix/fluoRadix (MatLab® platform), developed by our group for these purposes. Radix and fluoRadix (the last one is more dedicated to EDXRF applications), allow to filtering, organizing and manipulating data, as well as visualize the final images and spectra.

A coincidence time window is defined in the program to correlate the four signals corresponding to a single interaction, providing for each event a vector containing information about the interaction position (XY) and also the energy of the photon. In this way, an energy spectrum can be associated to each pixel. Besides that, it is possible to associate a region of interest (ROI) in the total pulse-height distribution to an X-ray image, in which only the photons within that energy region are showed [83, 84].

Position Resolution

The choice of the resistance value in the resistive line is very important, not only because we want to have fast signals to increase the high rate capability of the imaging detector, but also because we need to increase the Signal-to-Noise Ratio in order to obtain a good position resolution. It is known that low values of resistance are better to increase the rise time of the signals and avoid distortions on the final image at the edges, however, the SNR increases with the resistance, thus, it is necessary to find a compromise by choosing a resistance low enough to allow high count rate and high enough to ensure a good SNR.

Keeping in mind Figure 3.12, which illustrates the operation principle of the resistive lines used in the microstructure, and taking into account the input impedance Z of the preamplifiers (assuming they are similar), and the resistance R of the strip with length l and resistivity ρ, the ratio of the charges Q_1 and Q_2 at each end side of the strip is given by [87]:

$$\frac{Q_1}{Q_2} = \frac{(l/2 - x)\rho/A + Z}{(l/2 + x)\rho/A + Z} \tag{3.18}$$

Where x is the avalanche point relatively to the centre of the resistive strip, which can be given by:

$$x = l\left(\frac{Q_1 - Q_2}{Q_1 + Q_2}\right)\left(\frac{1}{2} + \frac{1}{R}Z\right) \tag{3.19}$$

The standard deviation of the position resolution, σ_x can be assumed as the best spatial resolution achieved by the resistive line. It can be easily determinated by using the error propagation formula. Thus, if the noise levels associated to charges at both ends of the resistive lines are identical and independent, it is possible to say that $\sigma_Q = \sigma_{Q_1} = \sigma_{Q_2}$, and the standard deviation of the position is given by:

$$\sigma_x = l\left(\frac{1}{2} + \frac{Z}{R}\right)\frac{\sqrt{Q_1^2 + Q_2^2}}{(Q_1 + Q_2)^2}\sigma_Q \tag{3.20}$$

If we consider a charge deliverying in the middle of the strips, the charge on both ends of the resistive line is equal ($Q_1 = Q_2 = Q$) and eqn. 3.20 resumes to:

$$\sigma_x = \frac{l}{\sqrt{2}}\left(\frac{1}{2} + \frac{Z}{R}\right)\frac{\sigma_Q}{Q} \tag{3.21}$$

The ratio $\frac{\sigma_Q}{Q}$ can be rewritten as $\frac{N}{S}$, where N represents the noise observed at the end

of the strip and S the charge signal. Therefore, we can conclude that the spatial resolution of the system is highly dependent on the Signal-to-Noise Ratio [87]. For higher resistance values the spatial resolution also improves.

Besides the SNR and the centroid fluctuation of the ionization cloud due to diffusion (section 2.1.1), there are other limitations to the spatial resolution of such a gaseous detector. One of the most important is the range of the photoelectrons generated during the primary interaction of the X-rays within the gas medium.

For pure Xe, in the X-ray energy range 3-45 keV, the main process of absorption is the photoelectric effect (Figure 1.2 from section 1.1.1).

Depending on the X-ray energy and on the atomic number of the absorbing medium, this process results in the emission of photoelectrons, fluorescence X-ray photons and Auger electrons, as explained in sections 1.1.2 and 1.1.3.

In the specific case of Xe and for the considered energy range, most of the L-shell and also some K-shell electrons are emitted, with empty positions left behind by the photoelectron. The atom then de-excites and the majority of its energy is released by emission of a fluorescence photon or more probably of an Auger electron. The probability of emitting Auger electrons compared to fluorescence photons increases with the atomic number of the material and from the K-series to the L and M series, as discussed before in section 1.1.4.

The photoelectron and Auger electron loose energy by collisions with surrounding gas atoms until they thermalize. The interaction position of the incident X-ray photon absorption can be defined as the centroid of the distribution corresponding to the ionization created by the emitted electrons, C_i. There is an uncertainty in the position of interaction introduced by the C_i which corresponds to the best position resolution achievable [88, 89].

The gas simulation program Degrad [90] (update of Magboltz/MIP [37] with accurate auger cascade model), developed by S. Biagi, besides the number of primary electrons and excitations together with their associated Fano Factors, allows also to calculate the spatial primary cluster distribution in pure gases or mixtures for X-rays. Thus, by using this program, the C_i originated by incident photons with energies between 3 and 45 keV (1 keV step) in Xe at 1 bar, was determined.

There were simulated 10000 events for each photon energy considering that the electrons thermalize 1 eV below the last excitation energy (8.32 eV [91]) in order to save computing time. The photons interacts in the (0,0,0) position on a 200 V/cm electric field, with the electron direction being randomly generated. For each simulated photon, of each energy, the C_i value was determined and plotted in the Figure 3.13. As can be seen, if C_i from many X-ray absorptions are considered, an approximately spherical cluster, is obtained. Based on this assumptions, we can infer that the cluster size dependence with the X-ray photon energy (Figure 3.13). It is easy to note that the greater the energy of the photoelectron/Auger electron, the higher will be its range and consequently the worse will be the spatial resolution

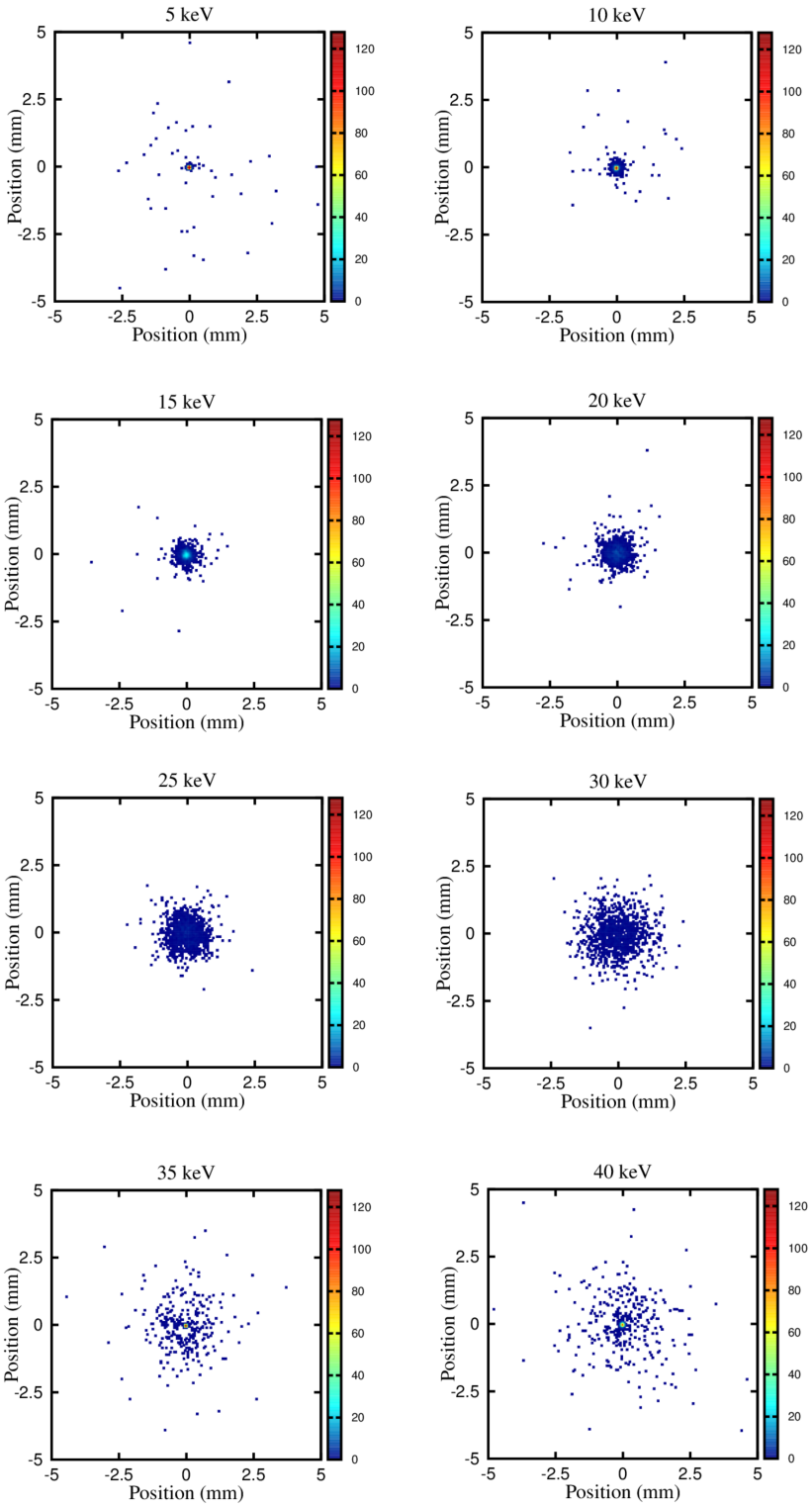

Figure 3.13: Dependence of the ionization cluster size created by 1000 photons with the X-ray energy, in Xe. Each point in the plot corresponds to the centroid of ionization of one X-ray photon absorption.

of the system. Projection of this spherical surface in one dimension gives us a gaussian distribution with a FWHM corresponding to the uncertainty in the position of interaction and therefore to the best intrinsic position resolution possibly achievable with Xe gas.

Another interesting point is that, for lower energies, 35 keV and 40 keV, a lot of additional clusters spread in the gas volume considered appear. These smaller clusters are due to the characteristic L-shell and K-shell photons produced in Xe. As the energy of the interaction photon increases, the photoelectron energy becomes dominant compared to the energy of the characteristic L-shell photon, which makes the average position of events (C_i values) closer to the photoelectron cluster.

For the case of Xe, used to fill the 2D-MHSP detector, the best FWHM and consequently position resolution that can be achieved is of about 50 μm, for a 7 keV X-ray photon energy (Figure 3.14).

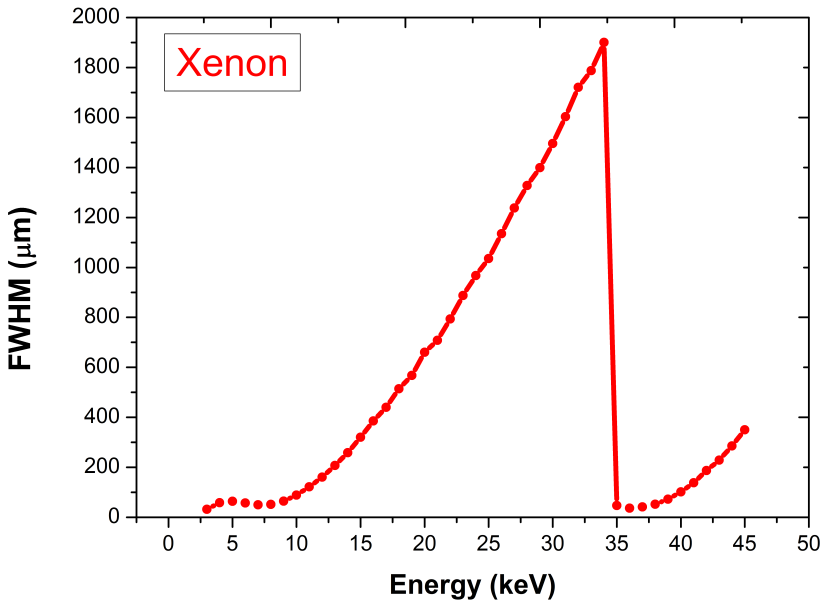

Figure 3.14: FWHM of the cluster gaussian distribution as a function of X-ray energy, for Xe.

It is also important to notice that once the X-ray energy is over the K-edge of the gas atoms ($\approx$ 35 keV), K-shell photoelectrons will predominate. This will lead to an improvement on the position resolution obtained (Figure 3.14), since the photoelectrons generated (for energies near the K-edge) will have shorter range than the L-shell photoelectrons [75].

In 2008, H. Natal da Luz reported position resolutions of 130 μm for the X dimension and 250 μm for the Y dimension achieved with the 2D-MHSP detector, for 8 keV X-rays [63]. The difference for the intrinsic value is, in this case, mainly due to the low Signal-to-Noise

Ratio in the Y dimension.

3.1.2 2D-THCOBRA detector

The detector system is composed by a aluminium vessel containing inside a metallic mesh in order to define the drift region, a THGEM and a THCOBRA disposed in a cascade configuration. These thick electron multipliers structures were previously described in section 2.2.2.4.

The 10 × 10 cm^2 THGEM used (0.4 mm thickness, 0.3 mm hole diameter, 0.1 mm rim and 1 mm pitch) performs a preamplification stage.

The 2D-THCOBRA has an active area of 10×10 cm^2. It is a double-sided structure made out of a 0.4 mm thick G10 plate, covered with 50 μm of copper on both sides. The one used in this work has a 0.3 mm hole diameter, a pitch of 1 mm and a rim of 0.08 mm.

On the bottom side a pattern of strips is etched: a circular electrode surrounding each hole with 0.2 mm width (cathode) and an anode strip about 0.2 mm wide, as shown in Figure 2.10. The strips on the top side are orthogonally disposed to the anode strips exhibiting a zigzag-shape by circumventing the holes (Figure 2.10).

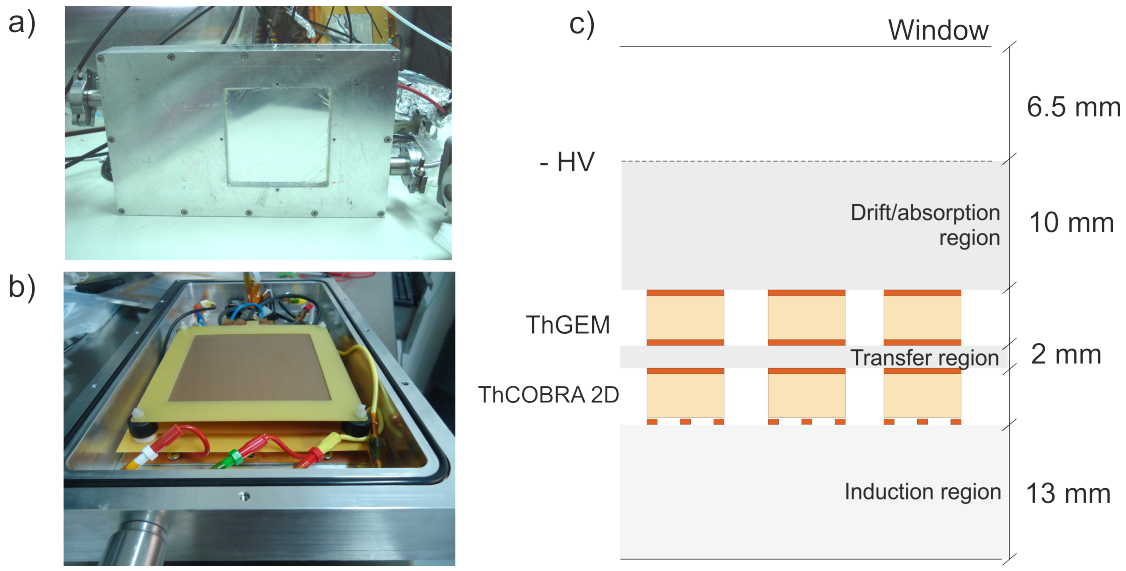

Figure 3.15: 2D-THCOBRA detector used in the experiments performed during this work. a) Photo of the detector; b) Inside view of the detector: the THGEM and the THCOBRA are disposed in a cascade configuration; and c) Detector configuration schematics.

Figure 3.15 shows the 2D-THCOBRA based detector used during the experiments performed in this work.

The thick structures and the mesh are fixed inside the detector through a nylon threaded

rod. In order to distance them from each other, Teflon® spacers were used for this task.

The electrical biasing is done through SHV panel connectors fixed to the detector body. For simplicity and ease of work, female banana jack connectors are soldered and glued with a low vapor pressure epoxy (Trabond® 2116) to the SHV connectors, allowing to easily connect/disconnect the male banana jacks from the high voltage cables soldered directly to the electrodes of the 2D-THCOBRA structure (Figure 3.15 b)). The solder used was pure tin since it is cleaner than the normal solders.

The window of the detector is made of a 55 μm aluminized Mylar® foil and has an area of 11 $\times$ 11 cm^2. The metallic mesh is 6.5 mm away from the detector window. The drift/absorption region is 10 mm deep. The distance between the THGEM and the 2D-THCOBRA is 2 mm and is usually called transfer region. The 2D-THCOBRA is placed 13 mm away from the detector body. A schematics of the 2D-THCOBRA configuration is shown in Figure 3.15 c).

The detector works with a continuous flow of Ne/5%CH_4 (27 l/h), enabling a continuous circulation of the gas through the detector chamber.

Although Ne and/or Ne mixtures are not so adequate gases for imaging applications, specially due to their low detection efficiency and long photoelectron range, as will be seen in the next chapter, when compared to other heavier noble gases, such as Xe, they present some advantages which should be exploited.

The main advantage of using Ne or Ne mixtures, as Ne/5%CH_4, in gaseous detectors, is related to the lower operation potentials compared to other noble gases traditionally used for this purposes. In Ne, the charge multiplication in the avalanche process occurs at lower electric fields due to its higher first Townsend coefficient [72].

Besides that, Ne/5%CH_4 is not so expensive as Xe or Kr, which means that it can be used in detectors working with a continuous flow of gas circulating through the chamber, which is the case of the 2D-THCOBRA developed in this work. Thus, expensive purification systems are not required [72].

3.1.2.1 Detection Efficiency

In the case of the 2D-THCOBRA detector, the detection efficiency is much lower than in the 2D-MHSP detector. This is mainly due to the used filling gas. The detection efficiency of the 2D-THCOBRA is highly limited by the absorption/drift region 10 mm wide and by the region between the window and the mesh, both filled with Ne/5%CH_4. The low absorption in a wide range of energies (specially for X-ray photon energies above 10 keV) represents the main disadvantage of Ne/5%CH_4 when used in detectors developed mainly for imaging applications. Nevertheless it can be a good solution for soft X-rays detection.

The Mylar® window has also some influence on the efficiency of the detector. In the plot of Figure 3.16 it is visible that the 55 μm Mylar® window absorbs almost completely

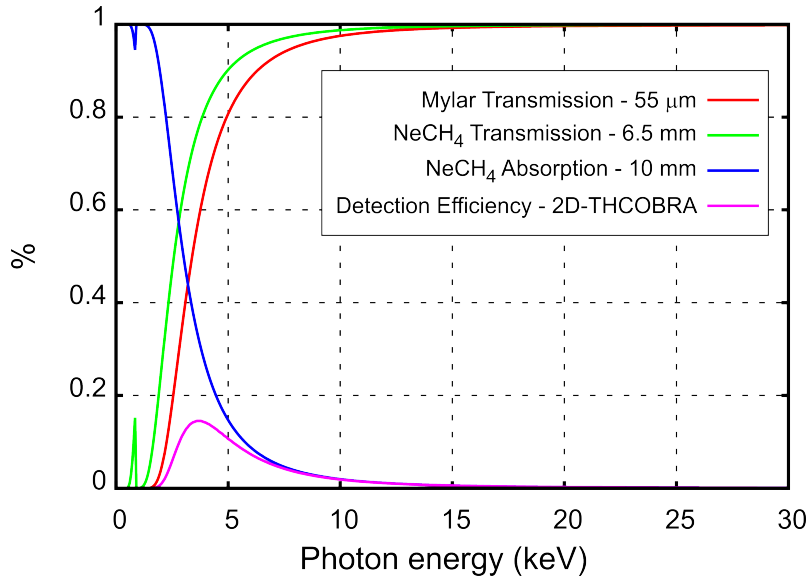

Figure 3.16: Detection efficiency curve of the 2D-THCOBRA detector, transmission curve of the 55 μm Mylar® window, transmission curve of 6.5 mm of Ne/5%CH_4 corresponding to the region between the window and the mesh, and absorption curve of Ne/5%CH_4, for a drift region of 10 mm, as a function of the incident energy. Data used for the detection efficiency calculation was taken from [80].

the photons with energies below 2 keV, similarly to what happens with the 75 μm Kapton® window used in the 2D-MHSP detector. Note that, contrary to the 2D-MHSP detector where vacuum is needed before filling the detector, the thickness of the window doesn't need to be too thick since the 2D-THCOBRA detector operates in flow mode and is not subject to large pressure variations. The detection efficiency of the detector was, in this case, calculated by multiplying the transmissions of both the window and the region from the window to the mesh, by the absorption of the drift region, which has a depth of 10 mm.

The highest detection efficiency region of the detector (above 10%) is achieved for energies between 3 and 5 keV, where the transmission in the Mylar® is between 15 and 80 %, the transmission in the region between the window and the mesh is relatively good (between 50 and 90%) and the absorption in the drift region is still reasonable (between 15 and 50 %).

The most limiting factors in the detector efficiency, specially in the low energy region, are the window thickness and region filled with Ne/5%CH_4, between the window and the mesh. Thus, if we reduce the window thickness to 5 μm and eliminate the region between the window and the mesh by using the window itself as a drift cathode it is possible to increase the detection efficiency (the maximum value obtained increased from 10 % to 65 %) for energies below 5 keV, as shown in Figure 3.17.

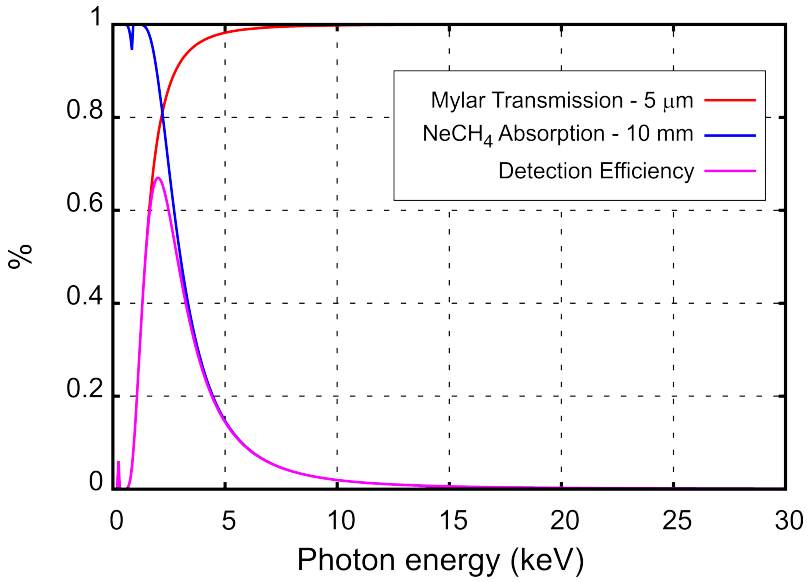

Figure 3.17: Detection efficiency curve obtained if a 5 μm Mylar® window serving also as the drift cathode is used. Data used for the detection efficiency calculation was taken from [80].

3.1.2.2 Energy Resolution and linearity

The energy resolution offered by the 2D-THCOBRA detector was inferred from its response to mono-energetic X-ray sources. In this case, the fluorescence X-ray lines from different single-element targets of Ti, Fe, Ni and Cu.

The single-element targets were placed 20 cm away from the detector window and excited through irradiation from the X-ray tube. The current and the voltage on the X-ray tube were set in accordance to the analysed target. A lead collimator with a 4 mm diameter hole was coupled to the detector window. By summing the charge collected from both ends of the resistive line, a pulse-height distribution of the characteristic X-rays of the target element was acquired. The obtained spectra can be seen in Figure 3.18 a). A good linearity was achieved for the measured amplitude as a function of the X-rays energy, as shown in Figure 3.18 b). The energy resolution was determined by fitting a Gaussian distribution to the peak of the fluorescence K-lines, and was found to be 23.8%, 21.4%, 20.4% and 20.3%, for Ti, Fe, Ni and Cu respectively, as shown in Figure 3.18 c).

The points follow a $E^{-1/2}$ dependency, as expected (section 3.1.1.2). By fitting them the following equation is achieved:

$$R = (3.1 \pm 0.2) \times 10E^{-1/2} + (9.3 \pm 0.7) \tag{3.22}$$

The values obtained for the energy resolution are different from the ones achieved with

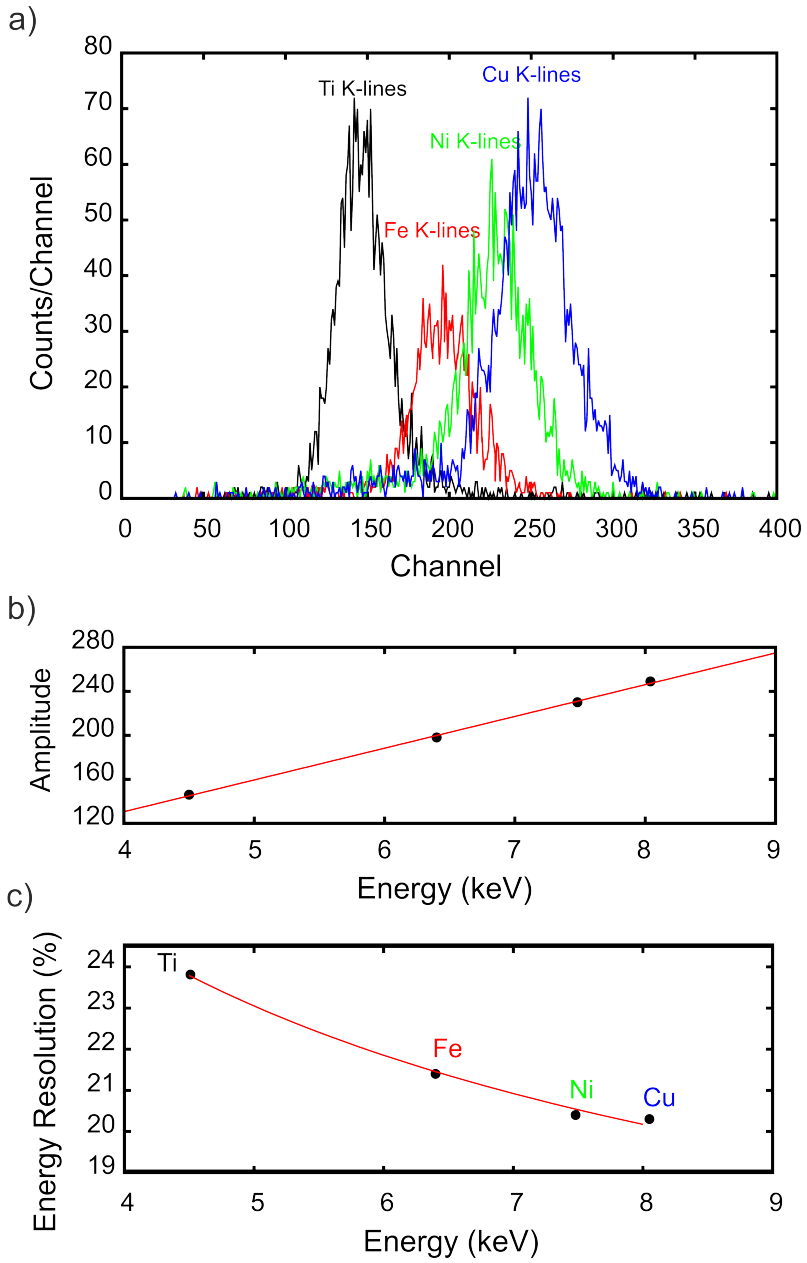

Figure 3.18: Fluorescence radiation spectra of different element targets: Ti, Fe, Ni and Cu; Both b) Pulse amplitude and c) Energy Resolution are plotted as functions of the detected energy photons [78].

the 2D-MHSP detector. This is mainly due to the different filling gases used in each case. The quantity $\sqrt{W(F+f)}$ in the equation 3.11 is higher for Ne/5%CH_4, since its W-value is higher than the W-value for Xe, as will be seen in the next section, leading to a lower value of the intrinsic energy resolution.

3.1.2.3 Gain performance

To evaluate the charge multiplication properties of the new 2D-THCOBRA detector, a study of the charge gain as a function of the V_{AC} and V_{CT} was performed.

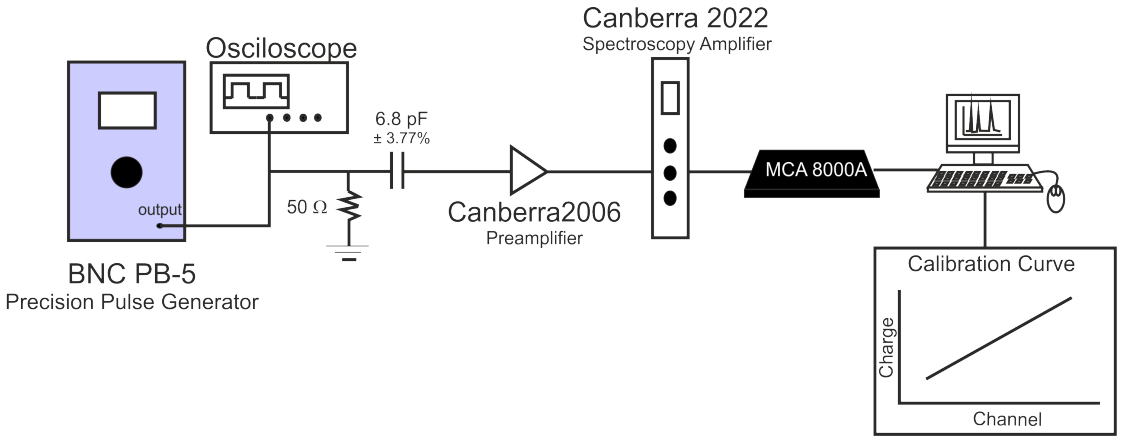

Figure 3.19: Charge calibration setup scheme [78].

The results were obtained using X-rays from Cu K lines, which produce the primary charge in the drift region of the detector.

The final charge produced by each event was collected at the anodes and tops of the THCOBRA by using a Canberra 2006 preamplifier (connected to one end of the resistive line) fed to a Canberra 2022 Spectroscopy Amplifier (shaping time of 0.5 μs). The output of the amplifier was connected to an Amptek MCA8000A multichannel analyser. The front-end electronics was calibrated by the injection of a known charge (using a calibrated 6.8 pF capacitor with a 3.8% tolerance and a BNC PB-5 Precision Pulse Generator) into the preamplifier input. The readout chain setup used for calibration is illustrated in Figure 3.19. In this way it is possible to measure the absolute charge corresponding to each ADC channel, which allows determining the collected charge for a given deposited energy.

In order to estimate the final charge produced by the 8 keV photons (Cu K-lines), a Gaussian function was fitted to the total absorption peak of the pulse-height distribution and the centroid position was determined. The gain is then given by the coefficient of the final charge over the average number of primary electrons (269.3 electrons) produced by the 8 keV in Ne/5%CH_4. Since no experimental value for the Ne/5%CH_4 W-value was found, it was calculated by using the gas simulation program Magboltz/Mip [37] and found to be 29.7 eV/ion-pair. The charge gains obtained as a function of V_{AC} and V_{CT} applied to the 2D-THCOBRA electrodes, for anode and top signals, are presented in Figure 3.20 a) and b).

The results show, as expected, that the charge gain increases exponentially with the increase of both V_{AC} and V_{CT}. It can also be seen that the charge gain increase is faster with the increase of V_{CT} than with that of V_{AC}, reflecting the larger width of the anode strips for efficient charge multiplication.

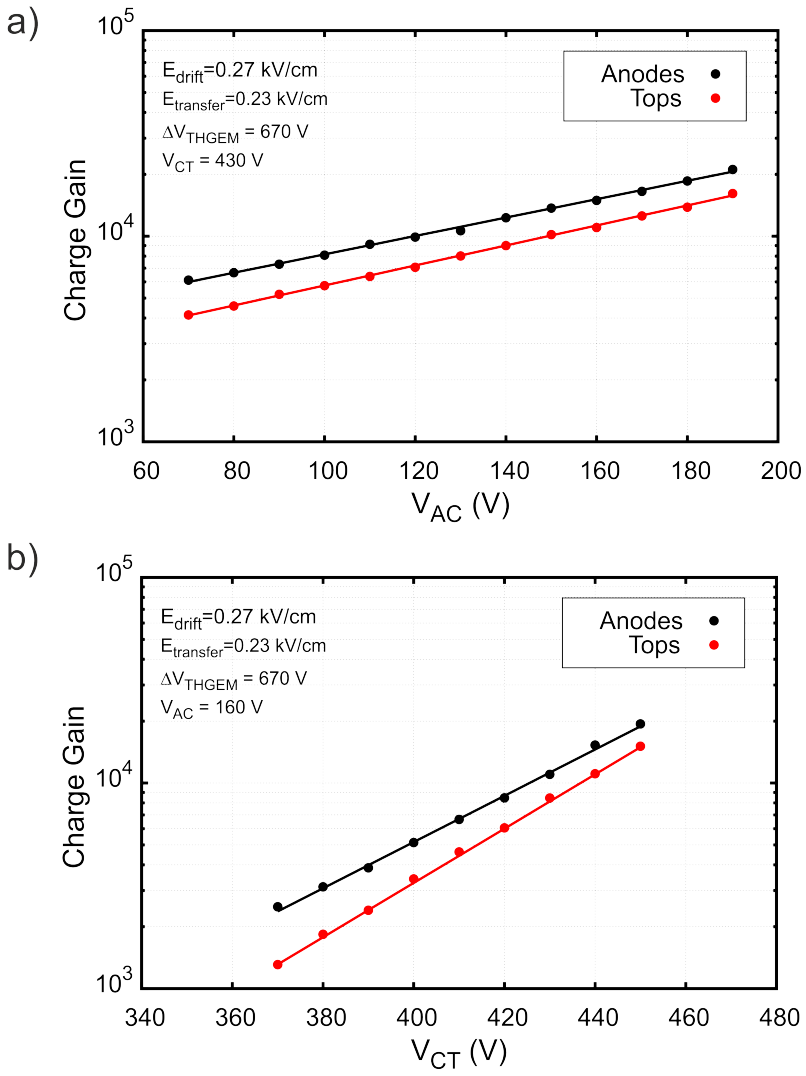

Figure 3.20: Charge gain as a function of a) V_{AC} and b) V_{CT} applied in the THCOBRA, with the detector operating in Ne/5%CH_4 at 1 bar [78].

As mentioned, for position resolution performance, it is important to evaluate the gain related to the charge collected in the anode strips, but also to the charge induced in the top strips. As it can be seen from Figure 3.20, the anode signal amplitudes always reveal slightly greater gains in both cases, about 30 % (V_{AC} and V_{CT} variation), when compared to the top signal amplitudes. This is due to the fact that the charge signals collected from the top side (top strips) are induced by the charge produced on the bottom side (anode strips),

which makes them typically 70 % of the anode signals, due to the 2D-THCOBRA substrate thickness. Nevertheless, in Figure 3.20 it is visible that as the V_{CT} increases, the gain in charge of the anodes and the tops tends to approach. With the increase of the electric field in the holes, part of the ions created in the avalanche is further collected on the tops, increasing the collected charge and therefore the charge gain. The maximum gain, before discharges, obtained by the detector operating in Ne/5%CH_4 was about 2.5×10^4, for a V_{CT} of 430 V and V_{AC} of 190 V. The detector shows very good stability, even at count rates as high as 100 kHz (per channel). The lower slope of the gain as a function of V_{AC} indicates that thinner anode strips need to be considered in the future in order to reach higher gains.

3.1.2.4 Imaging capability and position resolution

Similarly to the 2D-MHSP detector, two orthogonal resistive lines are used in the 2D-THCOBRA based detector for position readout, one connecting the anode strips and the other one connecting the top strips of the structure, as shown in Figure 3.12.

The charge collected on the anodes and the induced charge on the top strips are read from both ends of each resistive line and the interaction position is determined according to the principle of resistive charge division (Equations 3.16 and 3.17). For more details about the 2D-imaging operation of the 2D-THCOBRA detector please see section 3.1.1.5.

Image quality is a measure of the performance of an imaging system, and is directly related to the spatial resolution of the system. This quantitative parameter is usually used to compare different imaging system performances. These concepts are complex and not always sufficient to characterize all the complex and subtle aspects of imaging. Without entering too deep into detail, this section has the intention of giving the reader an introduction to how can a single parameter be used to evaluate the spatial resolution of an imaging system.

There are several approaches to assess the position resolution of an imaging system. In the case of this work it will be estimated based on the spread functions response in the image plane due to the emanating radiation of a source in the object plane. These spread functions are defined as the Point Spread Function (PSF), Line Spread Function (LSF) and the Edge Spread Function (ESF). Explanations about the ESF and its mathematical relation with the LSF will be given in section 3.24.

The PSF of the system is defined as the radiation intensity distribution in the image of an infinitely small aperture and it is a very accurate description of the system's spatial resolution.

The spatial resolution of an imaging system is commonly associated with the FWHM of the profile of the intensity map in the image plane originated by the emitted radiation from a point source in the object plane, i.e., the FWHM of the PSF.

Unfortunately, this method is not often applied because in practical systems, direct measurements of the PSF are very difficult to obtain. Firstly, it is very difficult to make a

small enough aperture relatively to the size of the PSF, in order to approximate the aperture to a point source. Secondly, measurements of the resulting intensity distribution in the image plane require that the focal spot of the X-ray tube must be exactly aligned with the centre of the aperture, which for such a small aperture and relatively long distances from the tube, is a very difficult task.

These experimental drawbacks, which cause inaccurate measurements, can be easily overcome by measuring other useful spread functions, such as the LSF or the ESF.

As the name implies, the LSF corresponds to the radiation distribution in the image of an infinitely narrow and infinitely long slit. It can be interpreted as a linear collection of a large number of PSFs. Experimentally, the LSF is easier to obtain than the PSF. To determine the LSF the circular hole is replaced by a long narrow slit, that reduces significantly the technical difficulties associated with obtaining and measuring the PSF. The slit is imaged and a 90° intensity profile distribution across the slit is measured.

Assuming that the PSF of the imaging system is space invariant and isotropic, we can approximate the FWHM of the LSF to the width of the PSF and consider it as a measure of the position resolution for the coordinate perpendicular to the slit's direction.

As for the PSF, the width of the slit must be sufficiently narrow so that its finite extent does not contribute significantly to the width of the image. That is, the spread in the imaged slit must be due almost entirely to the blurring introduced by the imaging system rather than by the width of the slit. Thus, taking into account the finite width of the slit used in the experiments, it is possible to determine the corrected spatial resolution of the imaging system by using an empirical equation introduced by Klein, *et. al.*, in 1981 [92] to determine the position resolution using a slit:

$$\mathrm{FWHM}_{\mathrm{corrected}} = w_{slit} \times \left[\frac{\mathrm{FWHM}_{\mathrm{measured}}}{w_{slit}} - 1 \right]^{1/3} \tag{3.23}$$

Where $\mathrm{FWHM}_{\mathrm{corrected}}$ is the resolution of the imaging system, w_{slit} the width of the slit used in the experiments and $\mathrm{FWHM}_{\mathrm{measured}}$ the FWHM of the intensity profile distribution measured across the slit. Note that the equation 3.23 can only be used when the slit has a width of the order of the resolution of the system.

Following the protocol described, the position resolution of the 2D-THCOBRA detector was determined by illuminating a lead slit of 1 mm, in two orthogonal directions. During the measurements, the X-ray tube has operated at 20 kV and 300 μA.

A small area of the acquired images, marked with a red rectangle in Figure 3.21 a) and Figure 3.21 b) was used to calculate the LSF originated by the slit.

Figure 3.21 a) and Figure 3.21 b) correspond to the anodes direction and top strips electrodes direction, respectively.

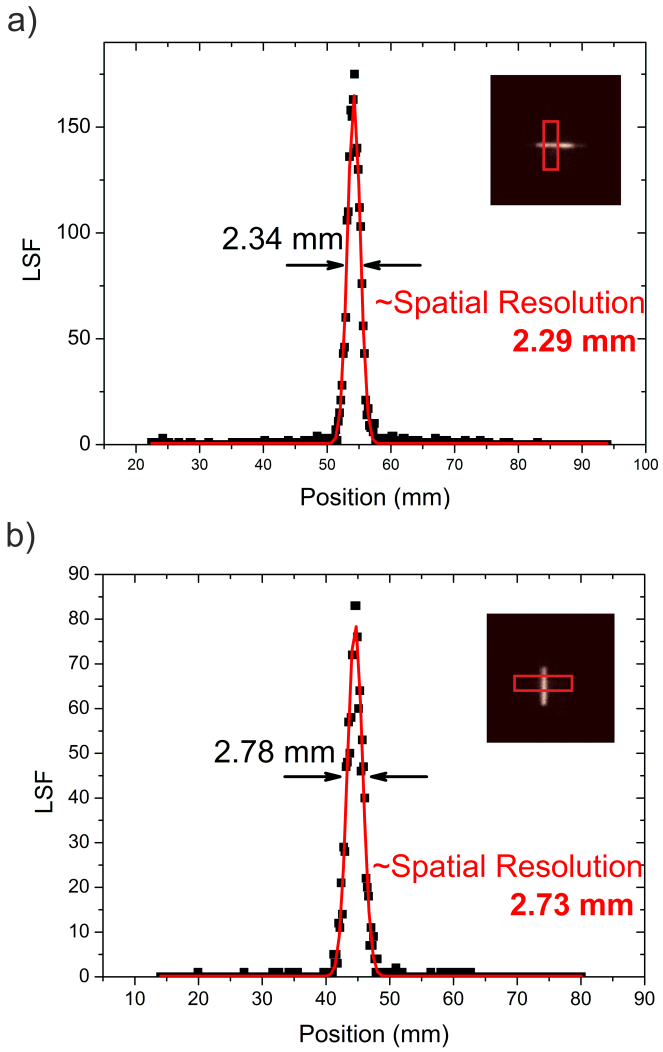

Figure 3.21: a) LSF obtained with a 1 mm slit in the horizontal position; b) LSF obtained with the slit in the vertical position [78].

A gaussian function was fitted to each LSF distribution and the correspondent FWHM was determined. The FWHM was found to be 2.34 mm for the anodes direction and 2.78 mm for the top strips direction.

By applying eqn. 3.23, it was possible to correct the FWHM resolution due to the finite width of the slit. The corrected spatial resolution was found to be 2.29 mm for the anodes direction and 2.73 mm for the top strips direction.

The slightly better results achieved for the anodes direction compared to the top strips are due to the difference in the SNR, since the charge signals collected from the top strips are typically 60% of the anode's charge signals.

However, the values for the spatial resolution obtained with this detector are not the best, position resolutions below 0.5 mm were already obtained for a position sensitive gaseous

photomultiplier with a CsI photocathode using a 2D-THCOBRA electrode readout [93]. This means that the position resolution determined is in this case strongly limited by the gas medium used, which is based on a Ne mixture, Ne/5%CH_4, not reflecting the intrinsic capabilities of the 2D-THCOBRA structure for position resolution.

In the case of the Ne/5%CH_4 the photons in the X-ray energy range 3-30 keV are absorbed by photoelectric effect in the gas (Figure 1.2 from section 1.1.1). By using the same gas simulation program as before, Degrad [90], the photoelectron range in Ne and in Ne/5%CH_4 was determined, similarly to what was done in the Xe photoelectron range study. The range of the photoelectron thermalized cloud was determined for incident photons within the energy range 3-30keV, in Ne/5%CH_4, at 1 bar.

The cluster shape and size originated for 5, 10, 15, 25 and 30 keV, is presented in figure 3.22. There is an evident cluster growth as the energy increases, since the photoelectron generated will have more energy to spend in collisions with the surrounding gas atoms until thermalizing. Therefore, for higher energies of the incident photon, worse spatial resolution will be achieved.

Following the same procedure used in the Xe case study, the FWHM of the gaussian distributions obtained by projecting the cluster sphere in one dimension were determined, as a function of the photons energy (Figure 3.23).

As can be seen in Figure 3.23, the best spatial resolution possible to achieve with this detector is strongly limited by the Ne mixture, since the best position resolution that we can have in this conditions is limited to 0.5, 1.5 and 3 mm for energies of 5, 10 and 15 keV, respectively.

In this way, it is very important to consider higher Z filling gases, in the future, for application considering detection of X-ray photons with energy above 5 keV.

3.2 Pinhole camera and system spatial resolution limitations

When designing a system for imaging X-ray emitters, a major consideration is which device the system will use to form an image of incoming photons.

In this section, the pinhole collimator characteristics are described and discussed as well as their influence on the spatial resolution of the system.

A simple model for the sensitivity of the pinhole collimator is to consider only the photons that pass through the aperture of the collimator. Mallard and Myers have proposed a formula (eqn. 3.24) to calculate the sensitivity of the pinhole obtained by geometric calculations [94, 95]:

$$g = \frac{d_p^2 \sin^3 \theta}{16h^2} \tag{3.24}$$

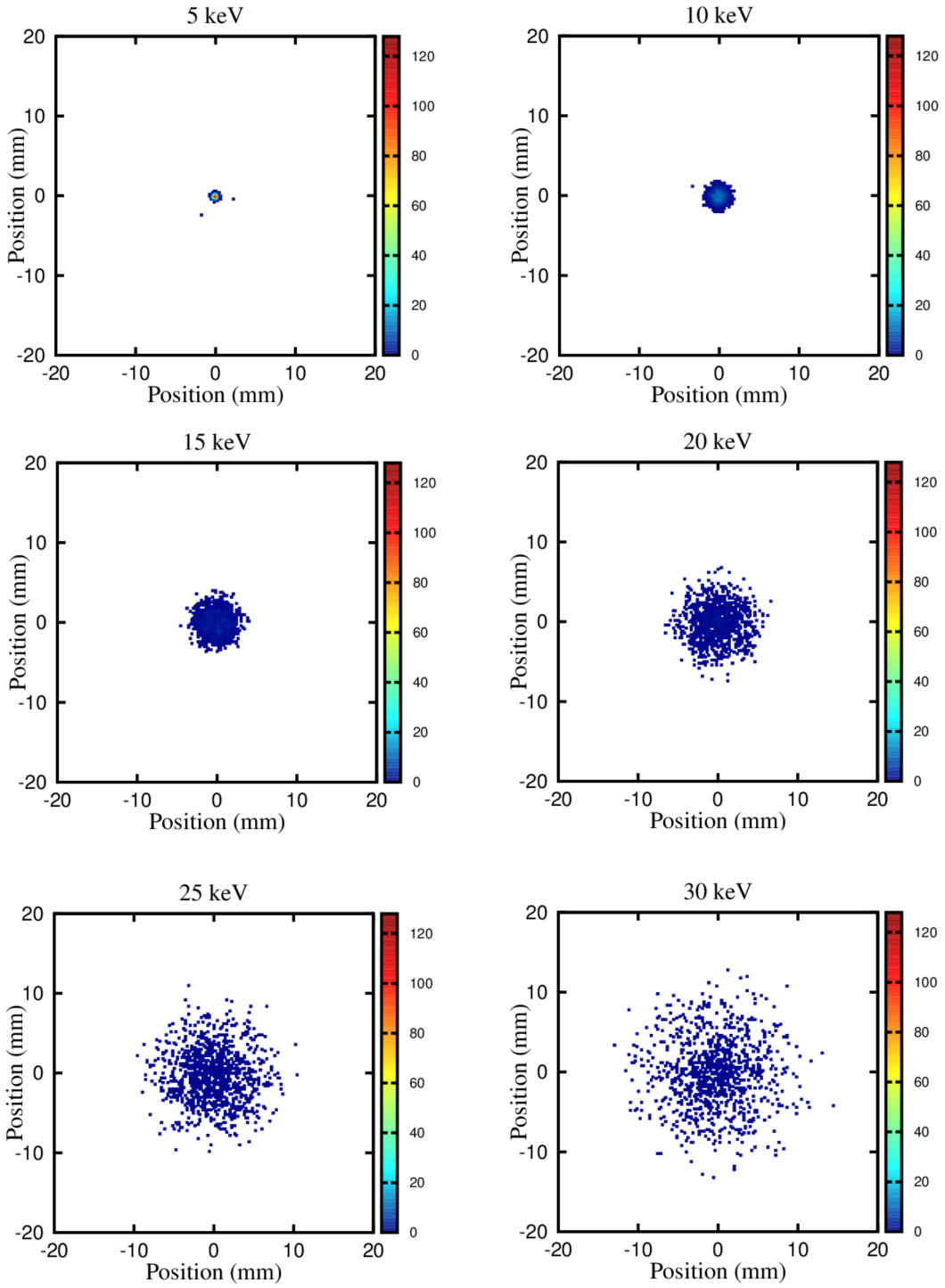

Figure 3.22: Dependence of the ionization cluster size created by 1000 photons with the X-ray energy, in Ne/5%CH_4. Each point on the plot corresponds to the centroid of ionization of one X-ray photon absorption.

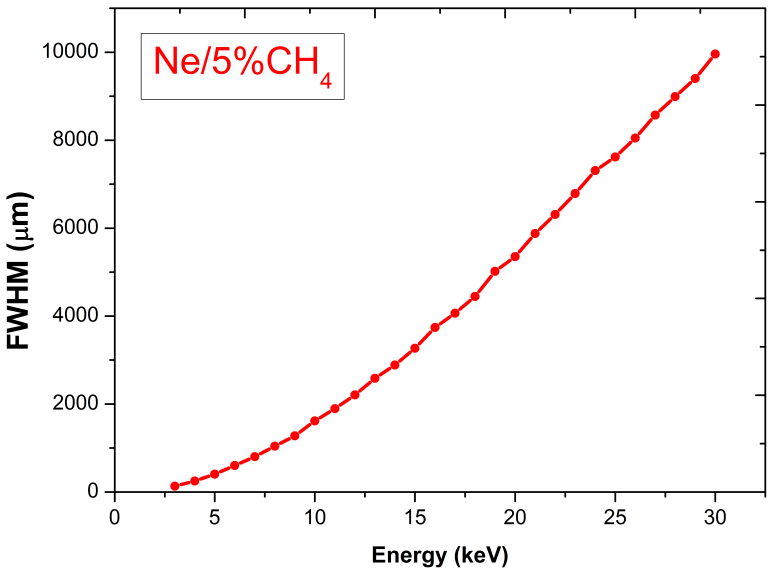

Figure 3.23: FWHM of the cluster gaussian distribution as a function of X-ray energy for Ne/5%CH_4.

where d_p is the physical diameter of the pinhole, θ is the incident angle measured as defined in Figure 3.24 and h is the distance between the point source and the pinhole plane.

The geometric resolution, λ_g, of the system can be calculated in object space simply by X-ray tracing. The expression is given by [95]:

$$\lambda_g = d_p \left(1 + \frac{1}{\mathrm{M}}\right) \tag{3.25}$$

Where M is the magnification of an ideal pinhole (please have a look at chapter 3 introduction, **Experimental Setup**).

According to the eqn. 3.25, to increase the resolution, the pinhole aperture has to be as small as possible. However, reducing the pinhole diameter to improve imaging resolution will produce a quadratic reduction of the pinhole camera efficiency because the sensitivity is proportional to the square of the pinhole diameter (see eqn. 3.24).

The system resolution, λ_s, is determined by the intrinsic resolution of the detector, λ_i, which depends on the intrinsic position resolution of the detector ($\mathrm{FWHM_i}$) and on the magnification M, and by the contribution of the pinhole λ_g which depends on its diameter and on the magnification of the imaging system (see eqn 3.26) [95].

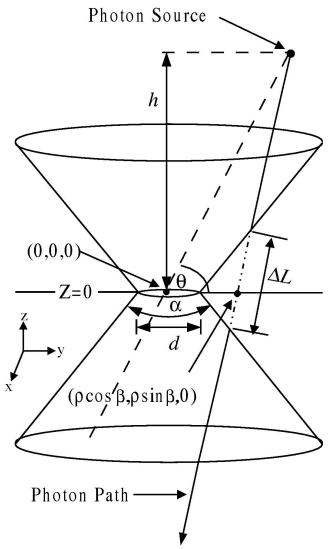

Figure 3.24: Geometry of the pinhole imaging [95].

$$\lambda_s = \sqrt{\lambda_g^2 + \lambda_i^2} = \sqrt{d_p^2(1 + \frac{1}{\mathrm{M}})^2 + \frac{\mathrm{FWHM_i}^2}{\mathrm{M}^2}} \tag{3.26}$$

Following that assumption, it was considered important, during the course of the present work, to conduct an experimental study of the system spatial resolution dependence with the magnification and pinhole diameter in order to further characterize the system we set out to develop.

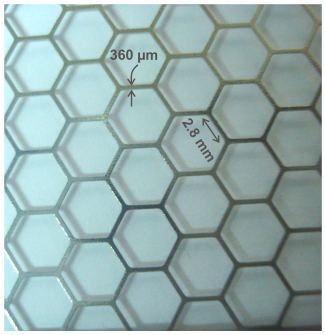

Figure 3.25: Sample photo: stainless steel hexagonal mesh.

The EDXRF imaging system based on the 2D-MHSP was used to study the system spatial resolution as a function of the magnification. The pinhole had a 200 μm diameter aperture and was made of a 50 μm thickness tungsten foil. Its transmission is, for a photon energy of 18, 21 and 25 keV, only 4×10^{-4}, 5×10^{-3} and 4×10^{-2}, respectively. The sample used in

the studies was a 360 μm stainless steel hexagonal mesh (sample), shown in Figure 3.25. The edges of the hexagons are 2.8 mm long. Distances from pinhole-to-detector (d_{pd}), and object-to-pinhole (d_{op}), were varied in order to get different image magnifications such as: 0.95, 1.25, 1.36, 1.64, 2.00, 2.46, 3.00 and 3.77. The acquisition time for each mesh image was typically 5 min.

A summary of the obtained images is presented in Figure 3.26. From this figure it is possible to infer that image quality, with respect to spatial resolution, improves with image magnification.

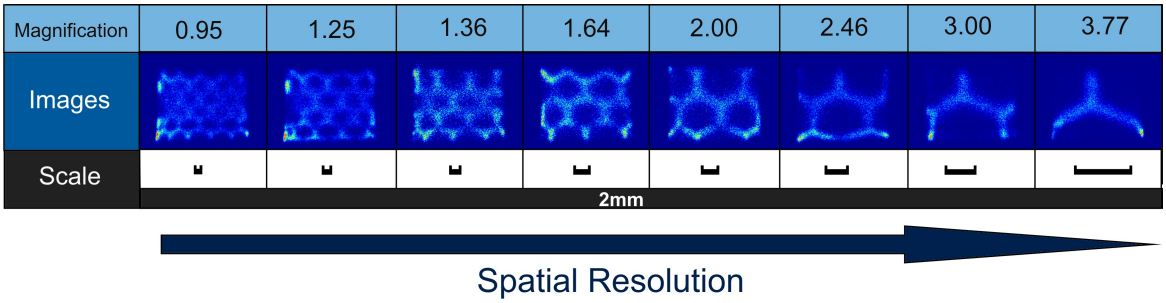

Figure 3.26: Image results for different magnifications [82].

The images of the stainless steel hexagonal mesh have enough information to define an edge response function which will allow determining the spatial resolution of the imaging system (Figure 3.27 a)). The method for spatial resolution determination of an imaging system based on the Edge Spread Function is very often used instead of the LSF or the PSF method. This is mainly because of two reasons. First, an edge response is much simpler to measure experimentally. Second, it is possible to access the LSF through the ESF.

Hence, by selecting in the acquired images a region with and without the mesh edge, an ESF is performed. In EDXRF imaging measurements, the density profile reflects the intensity of the emitted radiation by the sample object on one side of the edge and the absence of emission on the other side.

The obtained ESF distributions were fitted to sigmoid functions (Figure 3.27 b)). Then, to compute the LSF, it is only necessary to take the first derivative of the ESF. The LSF and the ESF corresponding to the selected region in the image of Figure 3.27 a) are presented in Figure 3.27 b). Knowing that the FWHM of the LSF corresponds to the spatial resolution of the imaging system we can infer that the distance required for the edge response to rise from 10-90% is directly related with the FWHM of the LSF and can also be used as a measure of the system spatial resolution [96].

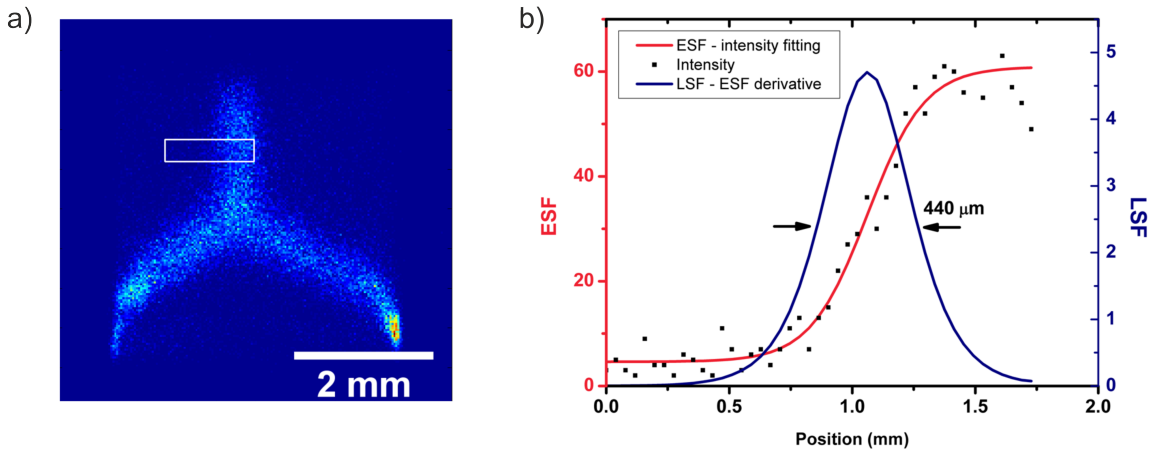

Figure 3.27: a) Fluorescence image of the hexagonal mesh with a magnification of 3.77. The selected region for spatial resolution calculations is delimited with a white rectangle. b) ESF and LSF used to determine the position resolution of the image in a) [82].

For a complete description of an imaging system's response, the LSF obtained through the ESF is not enough. Imagine that a different set of slits with different spatial frequencies is imaged. If the slits have the same width it is easy to understand that the contrast will decrease as the spatial frequency increases. Note that the contrast between two regions of an image is defined by the ratio of the amplitude intensity in the high intensity region to the average value in the low intensity region:

$$C = \frac{I' - I}{I} \tag{3.27}$$

Where I' is the mean intensity of the region with higher intensity and I is the mean intensity of the region with lower intensity.

On the other hand, if the slits have different widths but they are equally apart, then, the smaller slit will be the one with lower contrast.

This is exactly what the Modular Transfer Function (MTF) describes, the higher spatial frequencies and the smaller objects are reduced in contrast. Thus, the MTF can be seen as a quantitative parameter that describes the response of an imaging system as a function of the object size/spatial frequency.

The MTF curve is obtained through the one dimensional Fourier transform of the LSF and is nothing more than a plot of the contrast as a function of spatial frequency, which is expressed in line-pairs/mm. The spatial frequencies obtained for 3-10% of the maximum amplitude of the MTF are the most important values to be retained since they are related

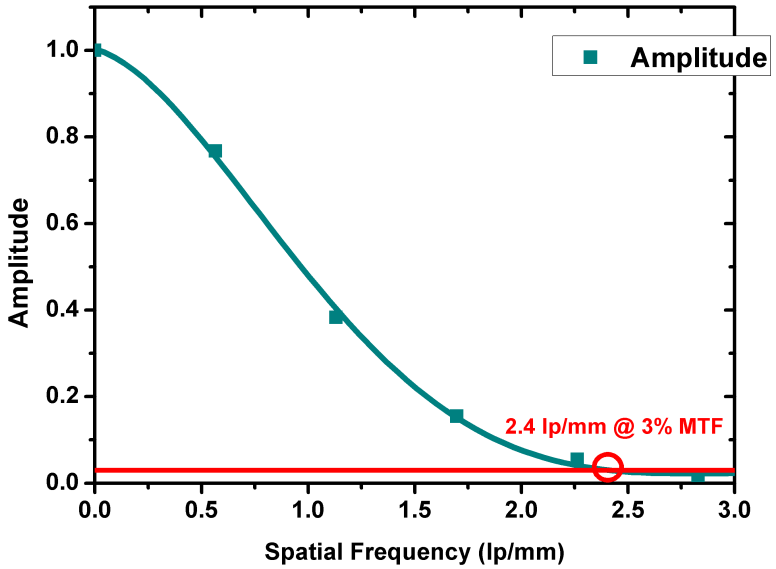

Figure 3.28: MTF of the region marked in the image of the Figure 3.27 a) [82].

to the ability of the human eye to distinguish low contrast differences [96]. Besides that, a system with a 10-90% edge response resulting in a FWHM of the LSF equal to w_x, will have a limiting resolution correspondent to 10% of contrast, about $1/w_x$ lp/mm [96].

Figure 3.28 shows the MTF curve obtained with the same data from Figure 3.27, corresponding to the image with higher magnification. A resolution of 2.4 lp/mm at an amplitude of 3% was obtained.

Figure 3.29 shows the MTF for all the acquired magnified images. As can be seen, the spatial frequency increases with the magnification, meaning that the spatial resolution of the system is better for higher magnification values, in agreement with eqn. 3.26.

For gaseous detectors such as the MPGDs, parallax error is a factor that deteriorates the precision of the detectors when measuring the position of X-ray photons incident at an oblique angle [97]. Thus, taking into account the oblique penetration and the different depth of interaction of X-rays along the detector drift region (illustrated in Figure 3.30), an uncertainty $\Delta x'$ in the position determination needs to be added as a contribution to equation 3.26, which is represented by the third term of the following equation:

$$\begin{aligned} \lambda_s &= \sqrt{\lambda_g^2 + \lambda_i^2 + \lambda_{\Delta x'}^2} \\ \Leftrightarrow \lambda_s &= \sqrt{d_p^2(1+\frac{1}{\mathrm{M}})^2 + \frac{FWHM_i^2}{\mathrm{M}^2} + \frac{(d'\Delta x/d_T)^2}{\mathrm{M}^2}(1+\frac{1}{\mathrm{M}})^2} \end{aligned} \tag{3.28}$$

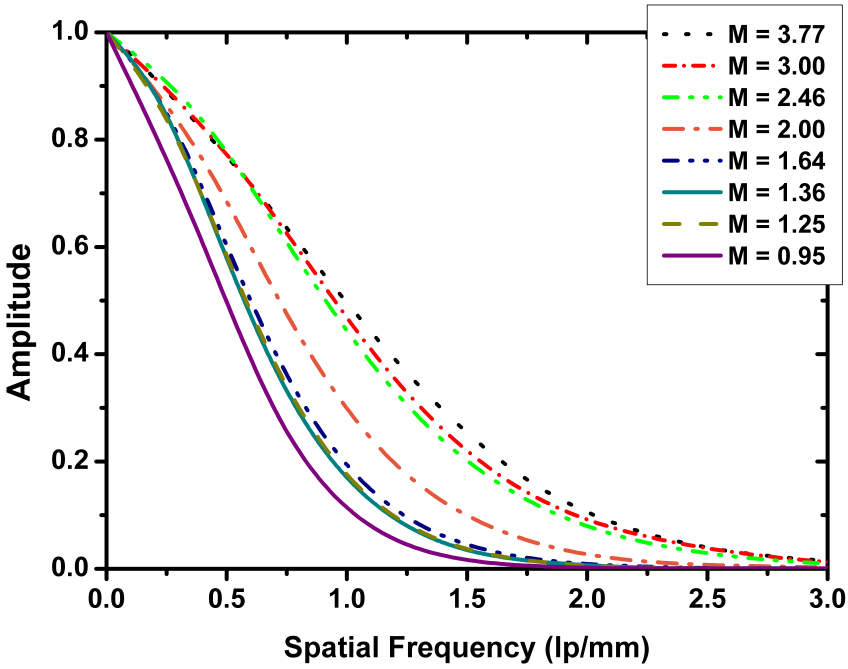

Figure 3.29: MTF for the images obtained for different magnifications [82].

In this way, the equation 3.28 takes into account not only the contribution of the intrinsic resolution of the detector, λ_i, and the contribution of the pinhole, λ_g, but also the contribution of the oblique penetration of the X-rays along the detector drift region, $\lambda_{\Delta x'}$. This dependence (Eqn. 3.28) is plotted in Figure 3.31, together with the experimental data and the predicted theoretical curve from equation 3.26. This plot shows that the contribution of the oblique penetration of X-ray photons is small and can be considered negligible for the higher magnification values.

The $\Delta x'$ depends on the incident photon X-ray energy. Smaller photon energies implies smaller photon penetration and smaller $\Delta x'$. The calculations related to the $\Delta x'$ contribution for the spatial resolution of the system were made considering that the high energy photons are uniformly absorbed along the drift, and for a value of Δx close to window limits which corresponds to the worst possible situation.

The experimental system spatial resolution (FWHM) varies between 900 and 400 μm for an image magnification between about 1 and 4. Both experimental and theoretical predictions present the same trend and the experimental curve approaches the theoretical one as M increases. Nevertheless, position resolutions obtained for the experimental data are slightly worse (about 30 %) than the theoretical values, possibly due to some non-uniformities of the sample, the pinhole, and the detector.

The spatial resolution converges to a value close to the pinhole diameter (Figure 3.31).

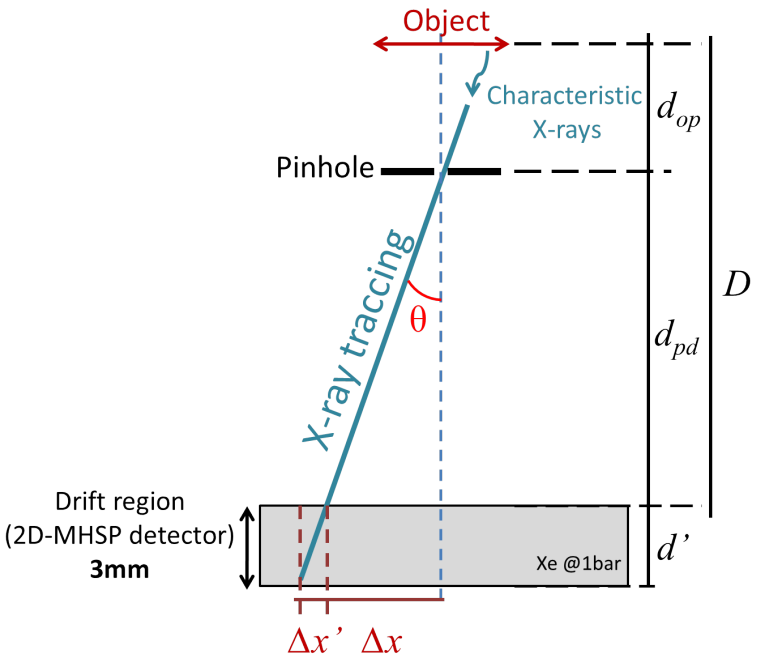

Figure 3.30: A point source at a distance D from the detector windoe emits a photon that passes through the pinhole, located at a distance d_{pd} from detector. The photon intersects the detector plane with an incident angle θ. $\Delta x'$ is the contribution of oblique penetration of x-ray photons in the gas medium. Adapted from [82].

This means that the pinhole diameter limits the spatial resolution of the system, even if we further increase the image magnification and/or the detector position resolution. To reach higher spatial resolutions, it is mandatory to use a pinhole with a smaller aperture. However, as was seen before it will produce a huge reduction of the system efficiency. Thus, it is necessary to establish a compromise between the spatial resolution and the detection efficiency for each kind of imaging system and sample used.

In reality, the diameter of the pinhole should be customized for the system in which it will be used. The larger the active area of the detector, the greater the pinhole diameter, in order to enhance the photon flux through it. Otherwise, to get some statistics on the image acquisition will get too long to acquire sufficient image statistics, thus, compromising the system's applicability.

For that reason, on the 2D-THCOBRA based EDXRF imaging system it is not so appropriate to use a pinhole with such a small diameter aperture as in the 2D-MHSP based system.

Because sometimes we need to further increase the photon flux through the pinhole aperture in order to decrease the acquisition time, we have to use a larger pinhole despite

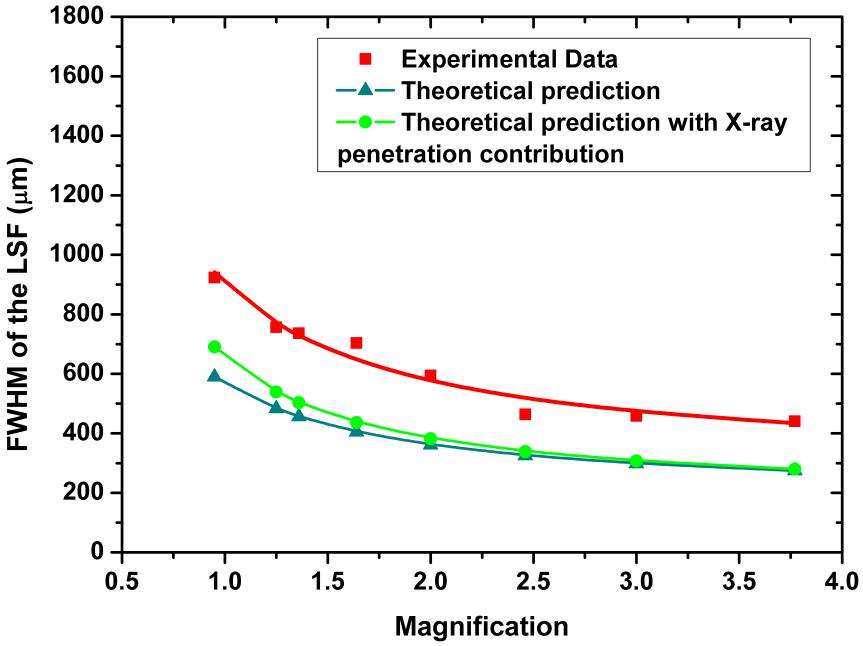

Figure 3.31: FWHM of the LSF as a function of magnification: comparison between experimental and theoretical predictions [82].

losing some resolution. Therefore, a simple experimental study was performed using the EDXRF imaging 2D-THCOBRA based system, to evaluate in a qualitative way the influence of the pinhole diameter used, in the obtained spatial resolution.

The sample used in the experiments (Figure 3.32), is a known sample purpose-built for this tests and it is composed of five different elements: Ti, Fe, Cu, Ge and Zr. The pinholes of 0.5, 1, 1.6 and 2 mm used for the measurements were produced by mechanical drilling of 1.5 mm thick lead foils. Their transmission, for photon energies up to 30 keV is negligible [80]. Distances from pinhole-to-detector and object-to-detector were set equal in order to get images without magnification, and constant for all the acquisitions. The change of pinholes between acquisitions was always carried out with great care, without changing the geometry of the system. The acquisitions were performed with the X-ray tube operating at 20 kV and 1 mA. The acquisition time was 15 min.

A summary of the obtained images is presented in Figure 3.33. By using the dedicated software fluoRADIX developed by our group, for image acquisition, processing and visualization of the results, it is possible to choose an energy ROI in the spectrum and plot the corresponding image considering only photons with energies within that ROI. Therefore, upon selecting a ROI, X-ray photons from characteristic lines can also be selected and the respective chemical elements can be mapped. Then it is possible to produce an image of the

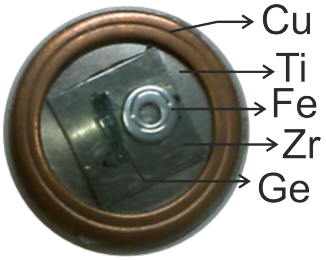

Figure 3.32: Sample photo. The know sample is composed by five different elements: Ti, Fe, Cu, Ge and Zr.

elemental distribution within the sample (an RGB image), by attributing a different primary colour (red, blue, green) to each ROI. In that case, we can also access the information about the intensity distribution in the elemental images (Figure 3.33 and Figure 3.34), which can be useful, for instance, to infer about the relative quantities of each element in the sample.

Figure 3.33 shows, as expected, that the spatial resolution and image quality offered by the imaging system is better for pinholes with smaller apertures. However, it is evident that for larger apertures, the number of photons detected per second is much higher, which resulting in images with more events for the same time of acquisition. Therefore, based on this study, the pinholes of 1 and 1.6 mm were found to be optimal for use with this system since we get a reasonable photon flux with a minimum impact on the position resolution.

Thus, if we want to promote the spatial resolution more than the efficiency of the pinhole we should use the 1 mm pinhole, but if on the contrary it is more important to increase the photon flux and the loss of spatial resolution is not critical, we must use the 1.6 mm pinhole.

Another solution which can be applied in order to increase the photons flux going through a pinhole can be the usage of a parallel multi-hole collimator. This kind of lead collimator is widely used in medical systems such as in gamma cameras.

By using a $10\times10\,\mathrm{cm}^2$ parallel multi-hole collimator with a 2 mm hole size, already existing in the laboratory for other research purposes, a fluorescence image of the same sample was acquired. The parallel multi-hole collimator was coupled to the detector window as shown in Figure 3.34.

The results are shown in Figure 3.35. As expected, considering acquisitions with the same number of events registered, the acquisition time was much shorter (≈ 2 min) than in the case of the acquisitions performed with the pinhole, even with the larger aperture one. Despite its advantages related to the higher efficiency of photons passing through the collimator, it has some disadvantages that we have to consider: the collimator projects the image of the same size as the object onto the detector, contrary to the pinhole that allows obtaining images of the objects with different magnifications, which can be a problem when is intended to see a small region of the sample with more detail; and the position resolution obtained. The low

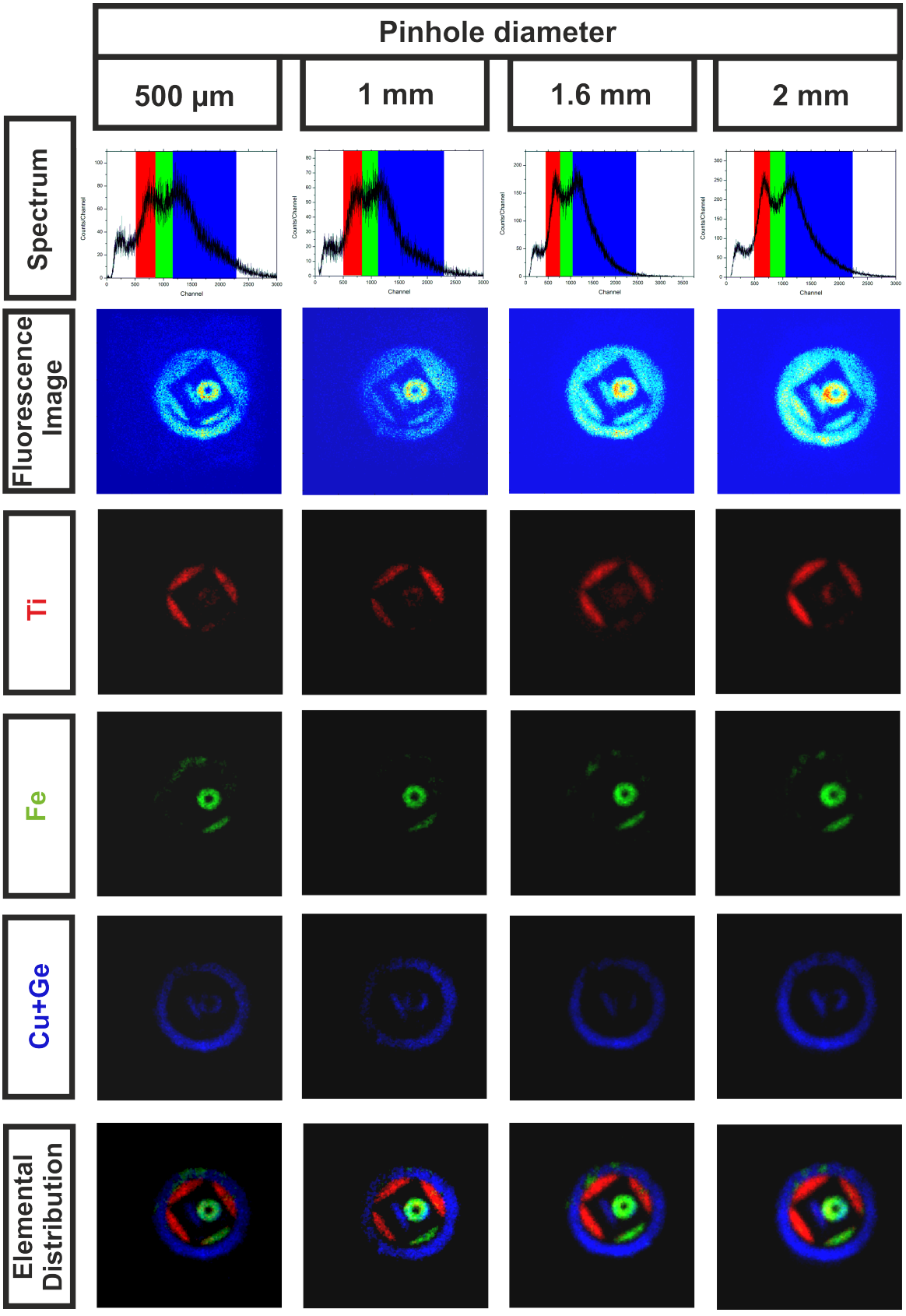

Figure 3.33: Image results for different lead pinhole diameters. The images were acquired by using the EDXRF imaging system based on the 2D-THCOBRA detector developed in this work (section 4.2).

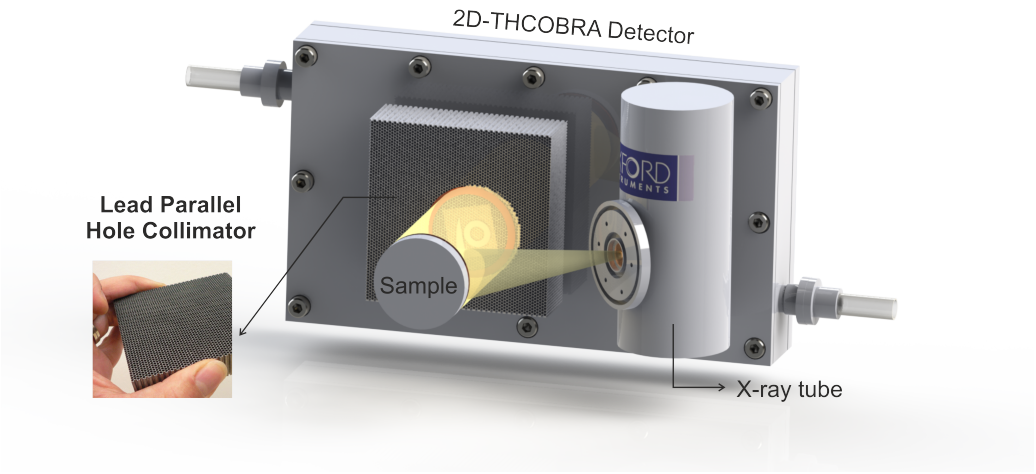

Figure 3.34: Illustration of an EDXRF imaging system based on a 2D-THCOBRA detector working with a lead parallel hole collimator instead of the pinhole camera.

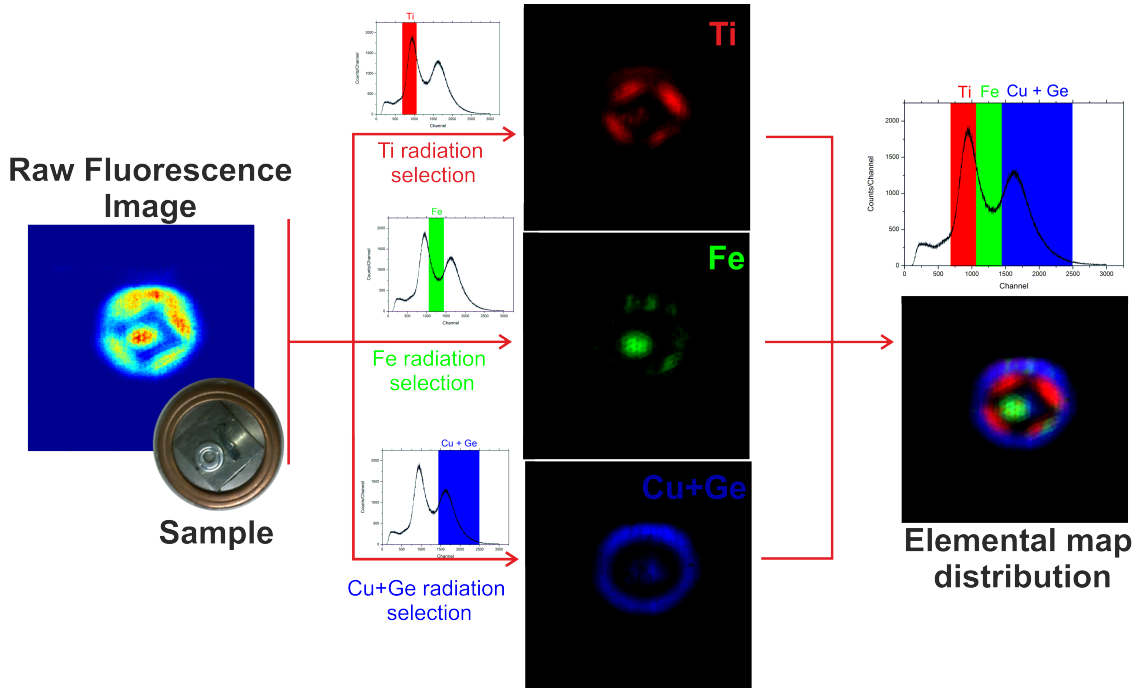

Figure 3.35: Parallel hole collimator system results. The raw X-ray fluorescence image and the individual elemental images combining the several selected energy regions of interest obtained irradiating a sample consisting of five different elements: Ti, Fe, Cu, Ge and Zr, is presented.

position resolution obtained is mainly due to the bigger size of the holes of the parallel hole collimator used, which is of 2 mm in diameter. In the images acquired, it is visible the shape

of the collimator holes. Therefore, we can conclude that this kind of parallel hole collimators could be an interesting solution for these applications, however, the hole size needs to be much smaller (< 1 mm).

CHAPTER 4

EDXRF IMAGING SYSTEM APPLICATIONS AND ANALYSIS

This chapter presents the results achieved with the EDXRF systems developed and presented in the previous chapter. It is structured in two main sections. The first one describes the performance of the MHSP based imaging system for applications in the cultural heritage and biomedical field. The second one aims to describe the capability of the 2D-THCOBRA based system for EDXRF imaging studies.

With basis on the results presented, a comparative and detailed discussion of the two developed EDXRF imaging developed systems will be done in the last part of this chapter.

4.1 2D-MHSP based system

As introduced before in chapter 3, the FF-XRF system based on the 2D-MHSP includes three main components: a low power X-ray excitation tube[4] (maximum voltage of 50 keV and current of 1 mA) with a molybdenum anode, tungsten pinholes of a 200 or 100 μm aperture diameter, depending on the analysed sample, and the 2D-MHSP based detector, geometrically disposed as shown in Figure 4.1. The whole system is supported by an aluminium base used to keep them in fixed positions during the acquisitions. The pinhole is supported by a stainless steel telescopic tube (Figure 4.1) that avoids the detection of undesirable X-ray photons that do not come directly from the sample through the pinhole and allows changing the distance between the pinhole and the detector and thus, varying the magnification of the obtained image. The X-rays emitted by the tube irradiate the sample with an angle close to 45° and excite its elements, which emit characteristic fluorescence X-ray photons. The emitted distribution is imaged onto the detector via pinhole optics and then detected in the 2D-MHSP detector (chapter 3).

Since the detector system is able to measure the interaction position of each incident X-ray photon as well as its energy information, a map of the element spatial distribution in the sample can be accessed, which can be seen as the ultimate goal of the application of this system.

This section is dedicated to the various applications made and results obtained with the EDXRF imaging system based on the 2D-MHSP detector, in different fields.

A Portuguese glazed tile from the XVII century was analysed in a cultural heritage application.

The 2D-MHSP based system was also used in more complex studies evolving biological samples. A study was also done based on the analysis of human teeth treated by dental amalgam. The goal of the analysis was to evaluate the system capabilities in the biomedical field by studying the drift of the major constituents of a dental amalgam, Zn and Hg, throughout the tooth structures.

[4]Oxford Instruments® - series 5000 Apogee- URL: http://www.oxford-instruments.com/.

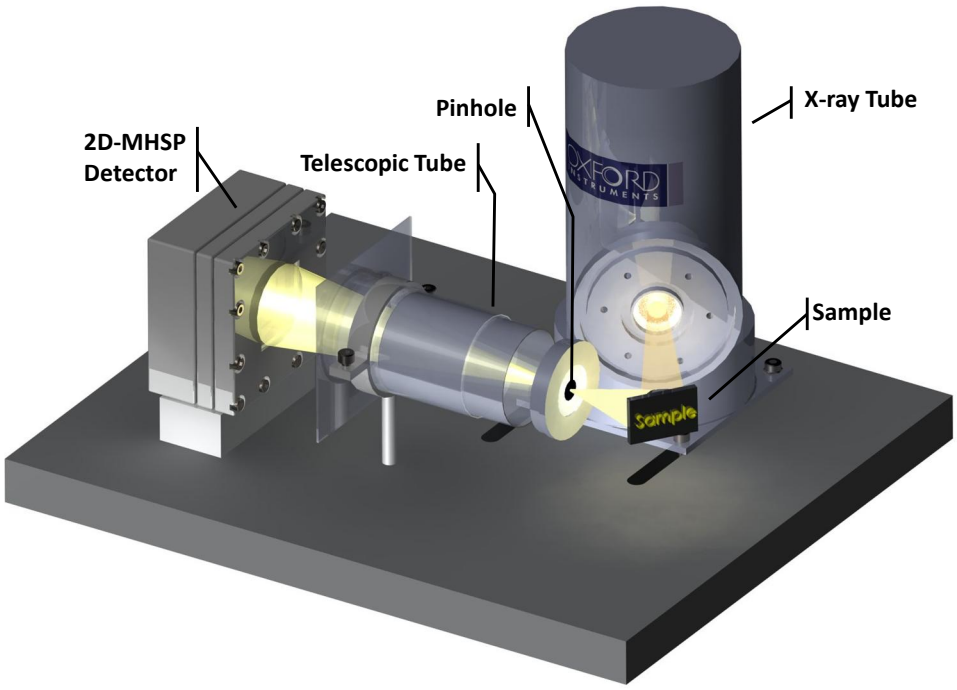

Figure 4.1: EDXRF imaging system based on the 2D-MHSP detector.

4.1.1 Cultural Heritage - Ceramic analysis

After using some samples with known compositions to validate the system operation [83, 98], the first application in the cultural heritage field of the EDXRF system based in the 2D-MHSP detector was done before [83], to study lead depth distributions in eighteenth-century Portuguese faiences from the Santa Clara-a-Velha monastery, Coimbra.

The ceramic pieces were analysed by examining a 2D image of a cross-section of the ceramic sample. The results can be found in ref. [98].

Thus, the first implementation of the system in the cultural heritage field has demonstrated its applicability, since it enabled the identification of different elements and revealed their spatial distributions in the irradiated sample. With this system, it was possible to perform an assessment of the Pb distribution in the glazed ceramics, such as its depth penetration.

The Portuguese glazed tiles (*azulejos*) have an important impact in the cultural heritage of the country, largely due to its use as ornaments in buildings. They are truly inspiring due to their different colours, textures or patterns.

Usually square in shape and not very thick, tiles are composed of a ceramic support over which a vitreous glaze is deposited by further processing, thus giving rise to an impermeable glassy and brilliant surface. The surface decoration is usually composed by colorants, usually

based in transition metals, which are incorporated to obtain the nicely decorated glazed surfaces of the tiles.

This type of cultural heritage ceramic pieces are very well studied in an art history point of view. Plenty of studies can be found in the literature related with their characterization most of them related with elemental and compound information [99–102].

Studies based in X-ray fluorescence techniques have shown to be essential to the knowledge and information about the historical background of such ceramic objects, concerning their manufacturing products involved in the glazing and surface decoration as well as their centre of production provenance in Portugal [99–101].

Investigations in a Portuguese surface decorated glazed tile were performed with the 2D-MHSP based EDXRF system. The main goal of the study was to evaluate the capability of the imaging system to get images of the spatial distribution of the elements (mainly pigment's elements) in the *azulejo* surface decoration. The glazed tile analysed belongs to the XVII century and was originally from the Odivelas Convent, Lisboa, Portugal.

Analysis and discussion

The photo of the analysed sample is shown in Figure 4.2. During the experiments, two different regions, marked with a red rectangle in the figure, were irradiated on the *azulejo* surface, which were decided to be called: *dragon head* region (Figure 4.2 a)) and *non-glazed* region (Figure 4.2 b)). The X-ray tube operated at 28 kV and 1 mA and a 100 μm diameter pinhole was used.

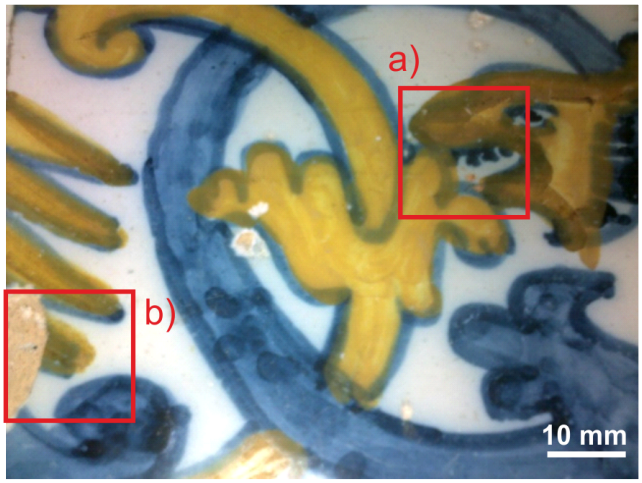

Figure 4.2: Photo of the ceramic tile surface analysed. The red rectangles in the image show the regions were the acquisitions were performed: a) *dragon head* region and b) *non-glazed* region.

By naked eye inspection, there are several characteristics about the analysed glazed tile, that we can extract immediately, such as the color palette used for the surface decoration, among others. We can retain that the decoration was done mainly using blue and yellow tones. The presence of coloration in an object with such cultural heritage importance is definitely the thing that create more impact in our perception. Portuguese decorative ceramics were mainly manufactured with a marked preference in the bluish and yellowish glazes [99, 100].

The glaze of the tile sample used is mainly composed by SiO_2, PbO and SnO_2 and is usually pointed out as a tin-lead opacified glaze ('white' glaze) [99]. An extensive review of the components and production of the glaze is not the essential purpose of this study. Thus, for additional information on this subject the reader should consult ref. [100].

Concerning the colours employment on the pieces, usually based on metallic oxides, they have been used and applied in a *frit* form, to the base glaze. The *frit* mixture is obtained by a pre-melting of the pigment with other elements such as Pb, Na or Sn for making it more opaque. In this way, this pigment composition mixture is then milled and turned into a powder which will be easier to apply over the base glaze [99, 100].

The elements associated with the blue colour, known as 'Egyptian Blue' are the Fe, Ni, Co and As, with the Co being the main and expensive element in the pigment. For that reason it is usually known as the blue pigment fingerprint [99, 100].

Concerning the yellow pigment, it is based on the 'Naples Yellow' composite ($Pb_2Sb_2O_7$). Also additional elements as Fe, Mn and Sn, are present in the yellow colour mixture [100].

The acquired EDXRF images of the sample are shown in Figures 4.3 and 4.4 corresponding to a magnification of $\times 1.2$. The first thing that stands out is the uniform distribution of lead, corresponding to the glaze, throughout the irradiated area.

The green image refers to the distribution of Fe and Co in the irradiated area. The K-lines of the two elements are indistinguishable in the spectrum due to the limited energy resolution of the system, which makes their separation quite difficult. Therefore, it was determined to be appropriate to consider both K-lines of Co and Fe, creating an image of the spatial distribution of both elements in the *dragon region* of the irradiated sample. Comparing that image with the sample photo, two issues come to mind. The first concerns to the detailed outlines of the painted objects. The contours are more densely coloured zones evidencing an increase in the element constituent of the pigment. Moreover, and secondly, the yellow pigment used for the contour of the dragon's head appears to be completely unprotected by glaze. In that case, it will be much easier to detect photons coming from the surface of the yellow pigment, for those who were deeper in it and protected by the lead glaze. This is why we cannot see the flower (painted in yellow with blue contours) bellow the dragon head well. Although we do still have photons from Co and Fe corresponding to the flower we cannot see them in the image, because when compared with the contour of the dragon head, they will be represented in the image with much less intensity and most of them will be eliminated

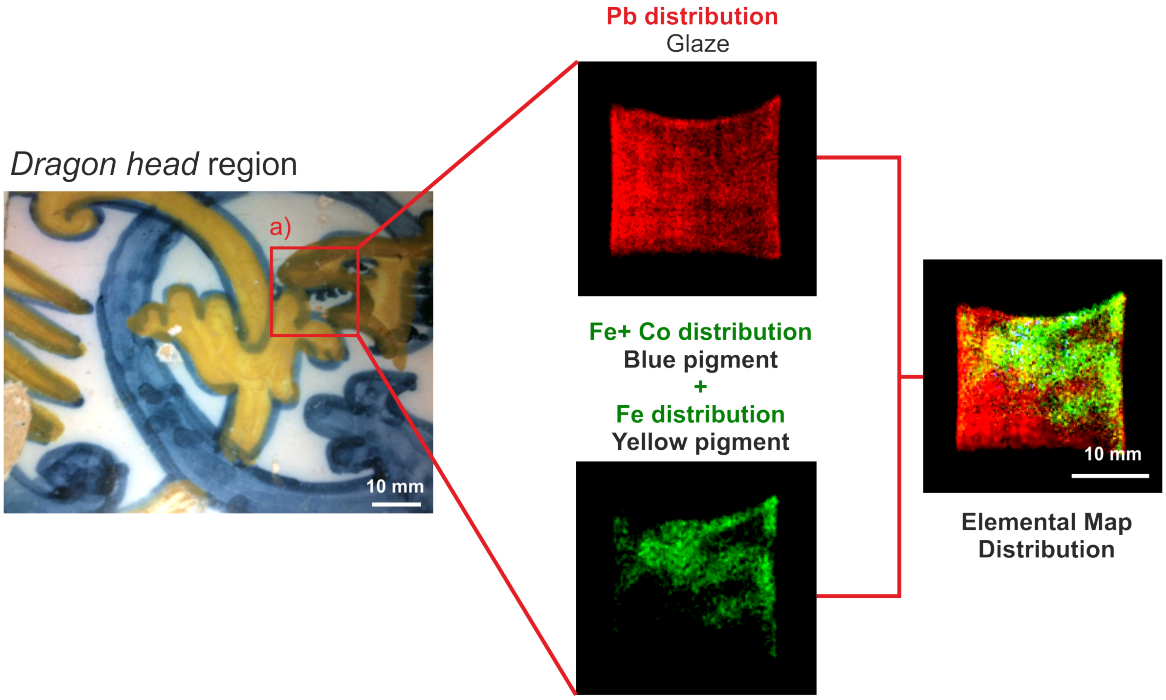

Figure 4.3: *Dragon head* region analysis. Pb (from the glaze) and Fe+Co (from the blue and yellow pigment) elemental spatial distribution images, together with the total elemental map distribution of the analysed region in the Portuguese tile from the XVII century.

upon application of a smoothing filter on the image.

The ability of the pigments to disseminate in the glaze is closely related to the composition of the glaze, however and according to ref. [100], the blue pigments have more ability to diffuse through the glaze than the yellow pigment, mainly due to the size of the molecules of the pigments.

Regarding the obtained results in the *non-glazed region*, Figure 4.4, the main differences to the *dragon's head* region are: first, the existence of a small region devoid of glassy matrix, which is perfectly correlated with the lead distribution image (red image); second, it was possible to obtain the Sb L-lines spatial distribution, from the yellow pigment. The Sb spatial distribution is not well distinguishable in the final map since the total number of Sb events is low when compared to the other images. This is not only because of the L-lines are much less intense than the K-lines, but also because of the low detection efficiency of our 2D-MHSP detector for those energies, 3.6 and 3.8 keV, L_α and L_β lines, respectively, as seen in section 3.1.1.1.

Regarding the distribution of Fe and Co, the image obtained is as expected. The Fe must be distributed over the yellow painted decorative motifs while the Co concerns to the blue zone in the lower right corner of the image. Note also that in the region without glaze there are a lot of visible events corresponding to the distribution of Fe on that region, because Fe

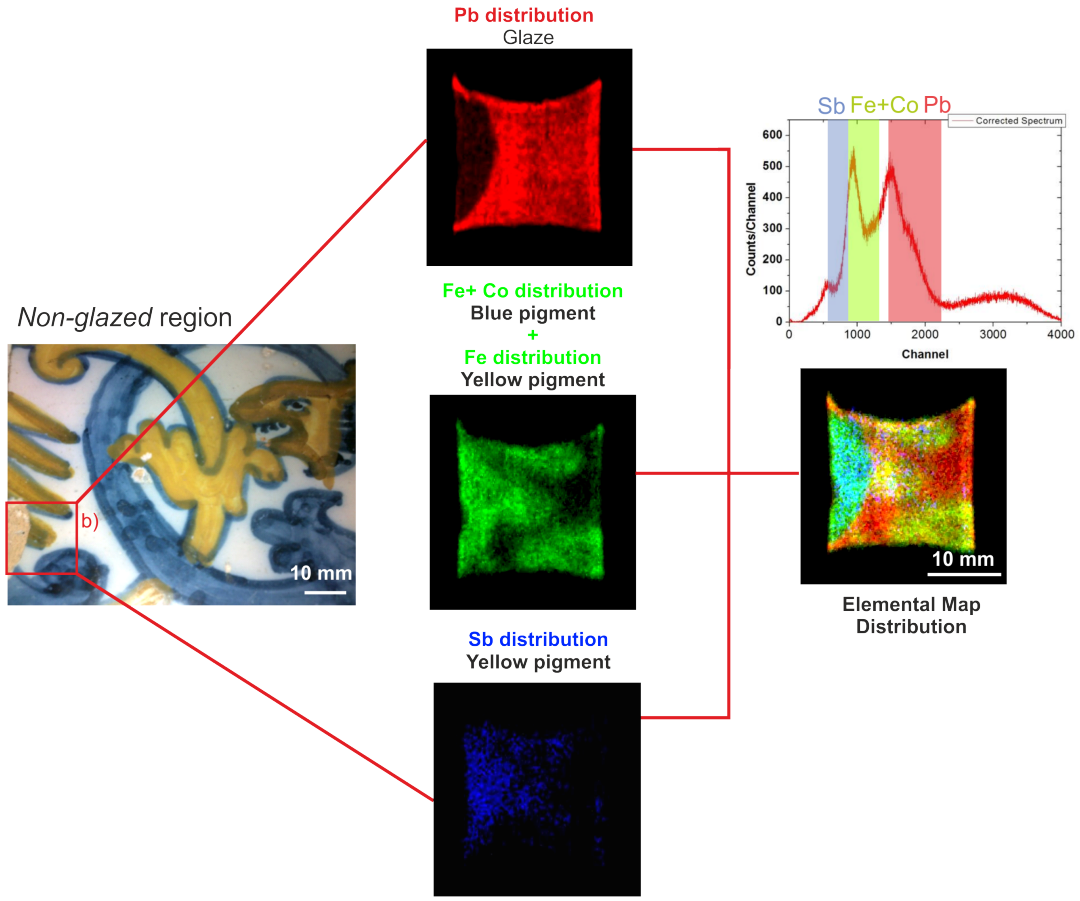

Figure 4.4: *Non-glazed* region analysis: Pb L-lines (from the glaze), Fe+Co K-lines (from the blue and yellow pigment) and Sb L-lines elemental spatial distribution images, together with the total elemental map distribution of the analysed region in the Portuguese tile from the XVII century.

is also one of the constituents of the ceramic body of the tile [100].

4.1.2 Biomedical - Human Teeth analysis

The knowledge of the spatial distribution of specific elements in biological tissues, especially in the human teeth, can provide much information about environmental influence in human organism [103, 104], contamination by metallic amalgams used as restorative materials [105, 106] and dietary habits [104, 107, 108]. The growing use of artificial materials in our modern world leads to an increasing exposition of the humans to substances liberated from these materials. The use of a dental amalgam as restorative tooth material is an example of that. Although the toxicity of the elements used in amalgams, such as Hg, are well known, it is not well clarified whether amalgam components are absorbed and drifted through teeth material. The release of some trace elements, especially Hg, from metallic amalgam filling and its long-term exposure on human health has been a controversial matter for several

decades [104, 106, 109–111]. During the present study and analysis, the spatial sensitivity of the EDXRF imaging system was evaluated by studying local variations in the elemental distribution of Ca, Zn and Hg over the axial cross-section of two restored and one healthy human teeth.

Non-destructive analyses of the major and trace elements present in biological samples are of great importance [112, 113]. The EDXRF technique allows obtaining material elemental composition and is distinguished by its ability to perform non-destructive analysis of the studied object. This technique have been widely employed in dentistry to study the non-homogeneity in elemental composition especially in cases of dental caries treated by dental amalgam[105, 109–111] or environmental contamination [104, 114].

During the measurements the X-ray tube of the imaging system operated at 27.5 kV and 1 mA for all the acquisitions. For the present analysis the 100 μm tungsten pinhole was used.

The samples

Human tooth is like a complex system of specialized tissues: enamel, dentine and pulp [105, 108, 114]. Each tooth is basically made up of two main parts: the crown and the root. Enamel serves to protect the underlying tooth and is considered the hardest and densest material in the human body. It is essentially composed of calcium hydroxyapatite crystals. The bulk of a tooth, both its root and inner aspects, is composed of another calcified tissue. It is called dentine and contains minerals, including hydroxyapatite, but not in as high concentration. Only about two thirds of its makeup is mineral which means that it is not as hard as enamel. The hydroxyapatite crystals from dentine are organized in a shaped tubules structure that runs from the enamel outer layer to the central pulp space of the tooth. This tubular structure makes dentine permeable, allowing to form a pathway for the spread of decay and allowing drugs and chemicals used in dental materials to diffuse into the pulp. The dental pulp or root channel is the central part of the tooth filled with soft connective tissue. This tissue contains blood vessels and nerves that continue down each root through the channels of the tooth [105, 108, 114]. A diagram of a molar tooth showing the different tissues is illustrated in Figure 4.5.

The analysed samples consisted of two molars treated by dental amalgam (sample A and B) and one healthy incisor (sample C).

Each tooth was cross-sectioned along the vertical median plane in several slices. These slices were polished along the whole tooth in order to obtain a smooth and flat surface of about 1 mm thick. Thus, the dental hard tissues enamel, dentine and their junctions were easily distinguished by eye. For more details about the sample's preparation, please see ref. [115].

For the present analysis it was only analysed one slice of each tooth.

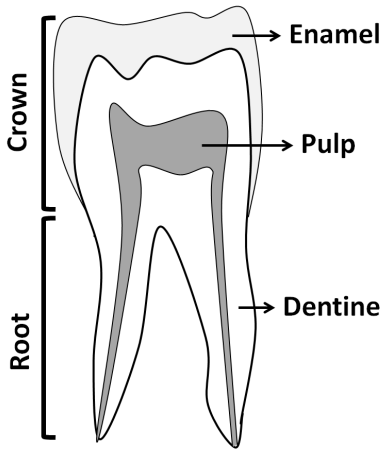

Figure 4.5: Diagram of a molar tooth [115].

EDXRF spectrometer

Parallel to the analysis performed with the EDXRF imaging system, it was also used an EDXRF spectrometer in order to acquire some spectra in selected regions of the teeth samples (region surrounding amalgam, root, dentine, etc) assessing the elemental composition of the samples and validating the results obtained with the 2D-MHSP spectrometer. The spectrometer consists of an X-ray tube equipped with a changeable secondary target, molybdenum. With this arrangement it is possible to obtain a monochromatic source. The selection of the secondary target may be chosen in order to get the best ionization conditions for a specific sample.

The X-ray tube, the secondary target and the sample are disposed in a geometry [107] called triaxial geometry due to the three orthogonal directions of the primary beam path, secondary-target beam path, and path from sample to detector. Taking advantage of the polarization effect of the incident X-ray beam from the tube, this arrangement will decrease the background and also improve the detection limits. The detector used was a Si(Li) detector, with an active area of about 30 mm^2, a 8 μm-thick beryllium window and an energy resolution of about 135 eV at 6.4 keV. The acquisition system was a Nucleus PCA card [107]. The X-ray generator was operated at 50 kV and 20 mA and a typical acquisition time of 1000 s was used.

Analysis and discussion

Three samples were imaged showing the local distribution of Ca, Zn and Hg: an healthy incisor (sample A), and two molar teeth treated by dental amalgam (samples B and C), as can be seen in Figure 4.6, 4.7 and 4.8, respectively. The present study was centred in the analysis

of the elemental distribution for Ca, Zn and Hg along the dental regions of the restored and healthy teeth.

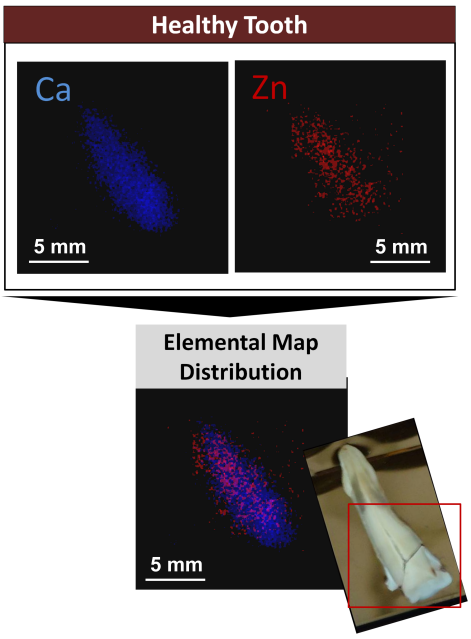

Figure 4.6: Sample A: Individual elemental images (Ca and Zn) and the elemental map distribution of the healthy tooth [115].

The main study is dedicated to the distribution of toxic elements, as Hg, due to the amalgam treatment, on the analysed carious teeth. Due to teeth restoration, the enamel is practically absent.

The first remark in the present results is the presence of Hg in the restored teeth and not on the healthy tooth, especially in the region surrounding the amalgam, which is in agreement with other studies in the literature [110, 111]. Although different elemental diffusion patterns were found in the two teeth, the presence of Hg, for both, at the closest points to the caries cavity may be related with amalgam contamination of the surrounding tissues [105, 109–111]. By using the 2D-MHSP based EDXF spectrometer, the elemental variation as a function of position as well as the local distribution of Ca, Zn and Hg, for a selected region of each analysed human teeth, from the root to the enamel, were obtained and are presented in Figure 4.9. The relative fluorescence intensities were normalized using the maximum value found for each element.

The spatial distribution of Ca showed that there are nonsignicant Ca levels changes at the dentine region. This behaviour was similar for all the analysed samples, independently of the analysed tooth [111].

Although the statistics were not very high in this case, the Zn content suggests a more or less uniform distribution along the whole healthy tooth. The same result was reported in the

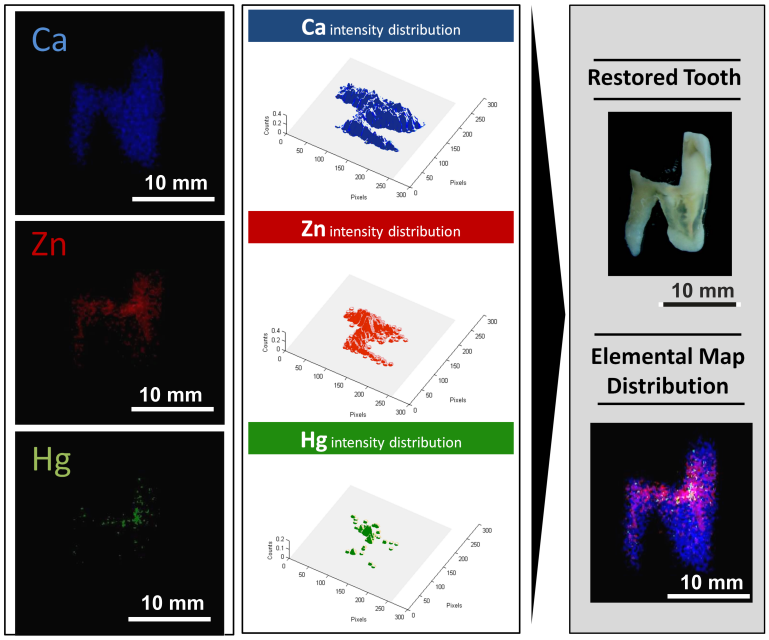

Figure 4.7: Sample B: 2D individual elemental images (Ca, Zn and Hg) and 3D elemental images, showing the intensity distribution of each element in the sample. Photo of the sample B. Resulting image combining the several selected elements (Elemental Map distribution) [115].

ref. [109] for healthy teeth. As expected, higher contents of Zn are present in restored teeth, especially in the dentine region, which can be due to the chemical affinity of this element to substitute Ca and Pb in the hydroxyapatite, facilitating the allocation of Zn atoms into the crystalline lattice [116]. This effect is more evident in the sample C, as will be further discussed. In the case of the restored teeth, Hg and Zn, shows a very similar diffusion pattern throughout the region selected. It is evident that a drift of these elements occur from the amalgam to the dentine, and to the radicular dentine regions. Sample C has shown an irregular diffusion pattern of Zn and Hg towards the tooth. As expected, high intensity peaks appear in the region surrounding the amalgam, probably due to amalgam contamination. In the median region of the tooth they exhibit also some intensity peaks suggesting a non-uniform drift toward the sample. As explained later in the ref. [110], this may be due to occasional hydroxyapatite network lattice defects. This irregular diffusion was also favoured by the fact that the restoration was deep and large, placing the metallic amalgam very near to the dentine and to the pulp of the tooth. It was observed that, for sample C, there is some Hg in the root of the tooth that suggests a higher and deeper diffusion of this element toward the sample. By using the EDXRF spectrometer, a fluorescence spectrum from the region surrounding amalgam and another one from the root of the sample C were acquired, in order to confirm the existence, although in small quantities, of this element in the root of the tooth. As can

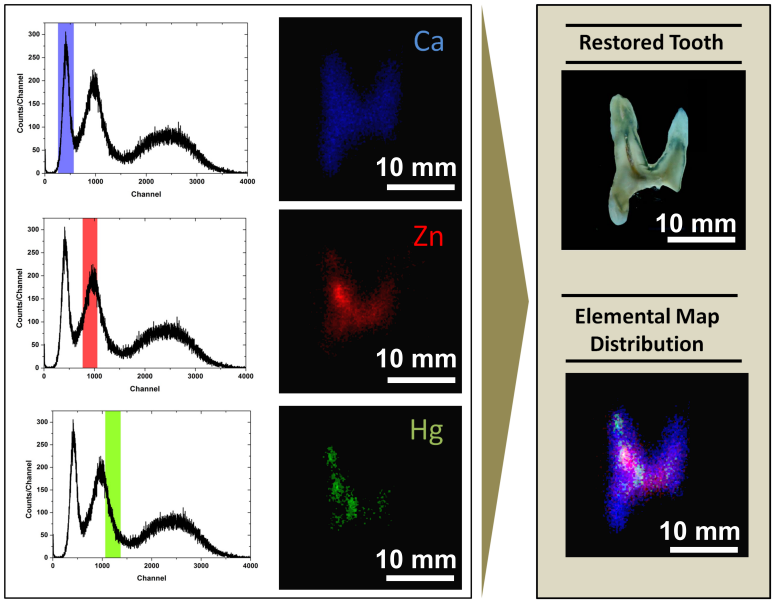

Figure 4.8: Sample C: Total pulse-height corrected spectra with different ROI selected depending on the element to be mapped and the corresponding individual elemental images (Ca, Zn and Hg). Photo of the sample C. Resulting image combining the several selected elements are also shown [115].

be seen in Figure 4.10, these analysis validate the results obtained by the 2D-MHSP based EDXRF spectrometer. Similar results for other restored teeth was reported in literature in the ref. [110].

In the case of the sample B, a different elemental diffusion pattern was found. The Hg is distributed in the region surrounding amalgam, as expected [105, 109, 110], but doesn't exist in the root region, which may suggest that there wasn't a deeper diffusion of this element toward the tooth. The Zn appears with higher concentration near the carious cavity [111], as well as the Hg, although Zn still exists with larger concentration in the dentine region of the tooth (Figure 4.7). The variability of the results found for the restored teeth can be due to some inhomogeneities in the hidroxyapatite crystals from enamel and dentine [112]. Other factors can contribute to these differences that were not taken into account, such as: caries extension, number of amalgam fillings [106], and the age of restoration.

4.2 2D-THCOBRA based system

The EDXRF imaging system based in the 2D-THCOBRA detector is composed by the X-ray tube, a lead pinhole of 0.5, 1, 1.6 or 2 mm, depending on the applications and on the spatial resolution required, and by the 2D-THCOBRA detector, whose characteristics were previously discussed in chapter 3.

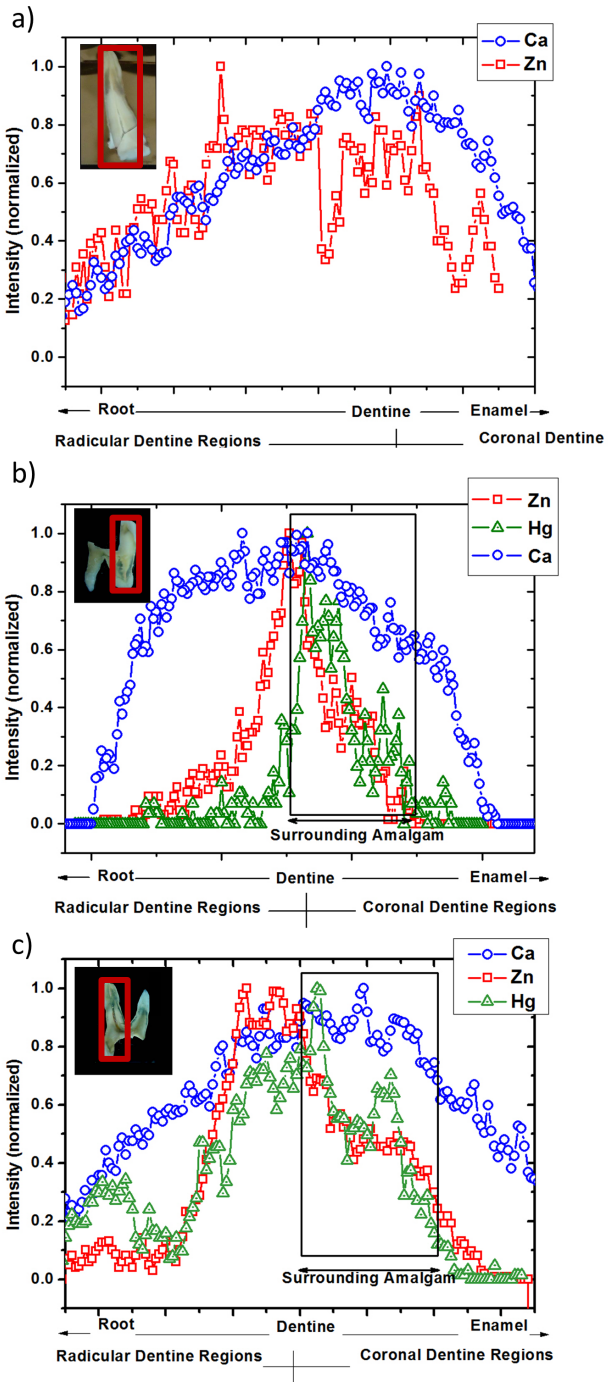

Figure 4.9: Local distribution of Ca, Zn and Hg in all analysed samples: Ca, Zn and Hg in all analysed samples: (a) Sample A; (b) Sample B: (c) Sample C [115].

These components are arranged in a appropriate and well-defined position setting to perform the measurements. The system components configuration is shown in Figure 4.11. The X-ray tube irradiate the sample with a 45° angle as shown in the same Figure.

The pinhole is incorporated in a 1.5 mm lead foil which was patterned to obtain a trapezoid

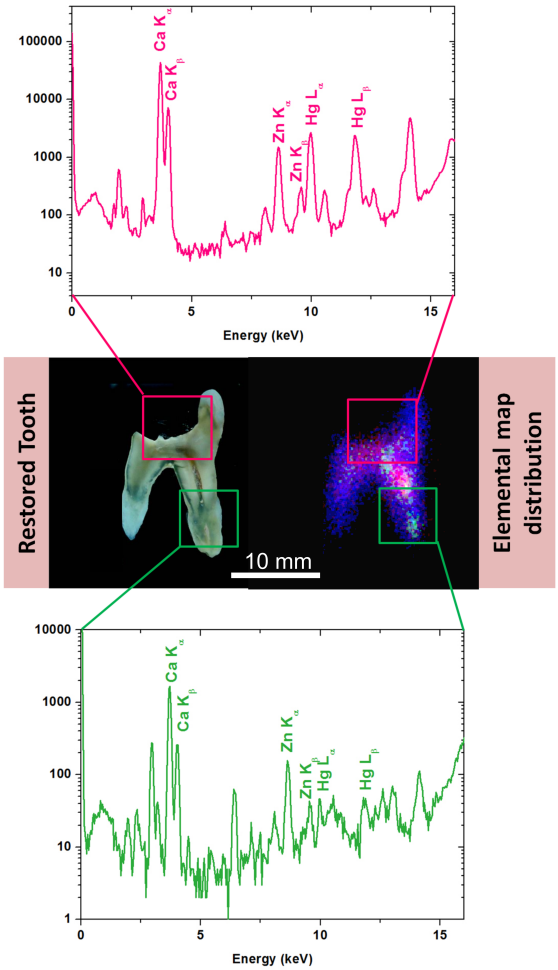

Figure 4.10: Fluorescent spectra obtained for the region surrounding the amalgam and the root region of a restored tooth (Sample C) [115].

shape. The lead foil is thick and big enough to avoid the detection of scattering photons that do not pass via pinhole optics onto the detector .

Since the lead is a easy to mold material, it is possible, if needed, taking the proper safety precautions, shape the lead foil to vary the pinhole-to-detector distance, and thus easily vary the magnification of the image obtained. If more adequate, the magnification can be also altered by changing the object-to-pinhole distance.

The main goal of this section is to study the performance of the EDXRF imaging system based in the 2D-THCOBRA for different samples. In a first approach, the system was used to study known samples in an attempt to validate it usage for EDXRF imaging applications. Then, some images of an illuminated parchment from the 15th- 16th century were acquired as a first application of the system in the art history field.

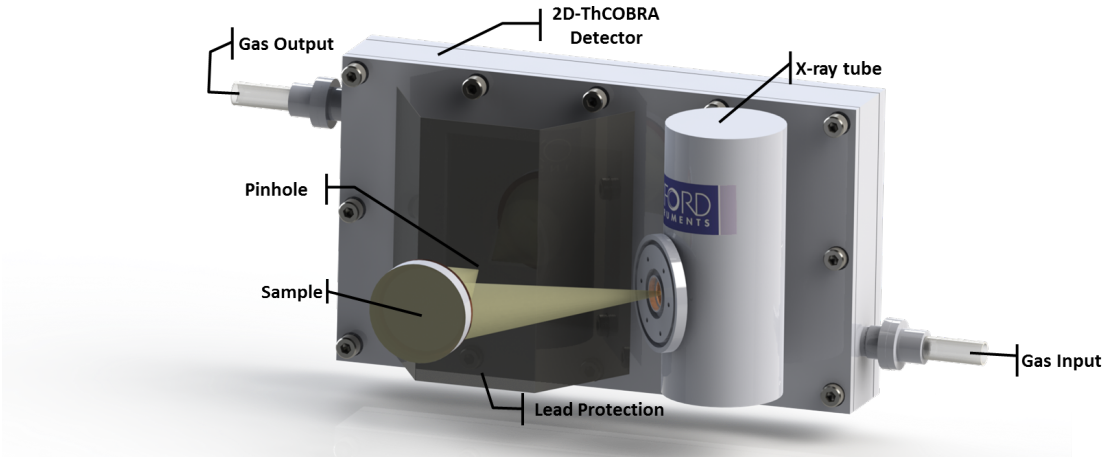

Figure 4.11: Experimental setup based on the 2D-THCOBRA detector.

4.2.1 Known samples

The first acquisition with the 2D-THCOBRA based system was conducted with a stainless steel gasket and a small piece of Ge, placed on a Perspex support. The stainless steel gasket and the small piece of Ge were used together with other elemental composition objects to study the influence of the size of the pinhole in the position resolution of the system, as presented before in section 3.24.

A fluorescence image of the sample was acquired. The raw X-ray fluorescence image, the individual elemental images obtained by selecting the respective energy ROI in the energy spectrum and an image combining the several selected elements are presented in Figure 4.12. A pinhole of about 1 mm diameter was used and the pinhole-to-detector and sample-to-pinhole distances were set to promote a magnification of about $\times 3$. An X-ray tube voltage of 22 kV and an anode current of 1 mA were used in this case. Good elemental identification is well visible as well as its distribution along the sample. Although in general tube voltages are higher in order to excite as many elements as possible for one measurement, in our experiments we have used a reduced tube voltage to excite more efficiently the elements that we know to be present in our sample.

The system sensitivity and spatial resolution capability was evaluated by considering only the fluorescence image after selecting an ROI correspondent only to the Fe K-fluorescence peak. Using the spatial resolution determination method through the ESF, explained in section 3.24, the spatial resolution corresponding to the Fe individual elemental distribution was measured. Figure 4.13 shows the image of the Fe spatial distribution and the correspondent ESF, LSF and MTF. As can be seen, a LSF FWHM of about 550 μm was obtained together a resolution of 1.95 lp/mm at a MTF amplitude of 3%, which in principle means, that for X-ray photon energies near 6 keV, spatial features above 550 μm, can be well resolved. Of course we have to take into account that in this case the magnification used is

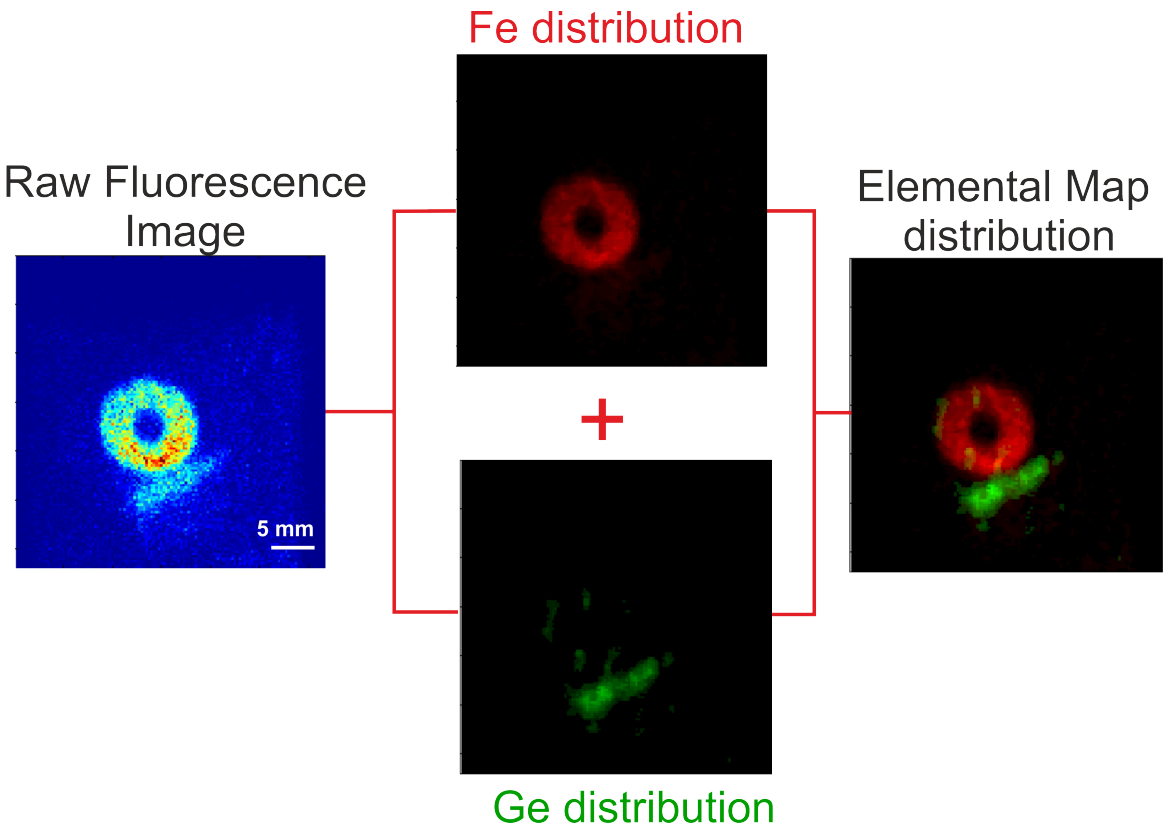

Figure 4.12: Raw X-ray fluorescence image, the individual elemental images corresponding to the Fe and Ge distribution and the final elemental map distribution obtained. A pinhole magnification of 3 was used.

quite large, which results on a spatial resolution improvement of about 45% when compared to the spatial resolution obtained for a magnification $\times 1$ (FWHM of the LSF), as seen in section 3.24.

In addition, since the image used for the study is not the fluorescence raw image, but, instead, it is a image originated after a ROI selection in the spectrum, we do not have the contribution of the background events from the raw image in the Fe distribution indivivual one, which usually leads to a deterioration on the position resolution achieved.

Known samples were used to evaluate the influence of the pinhole diameter in the system spatial resolution. Details concerning analysis in samples composed by five different elements are presented in section 3.24

The analysis performed over the known samples allowed to conclude that the system based on the 2D-THCOBRA detector, allow efficient elemental identification and position detection of fluorescence X-rays from multielemental samples.

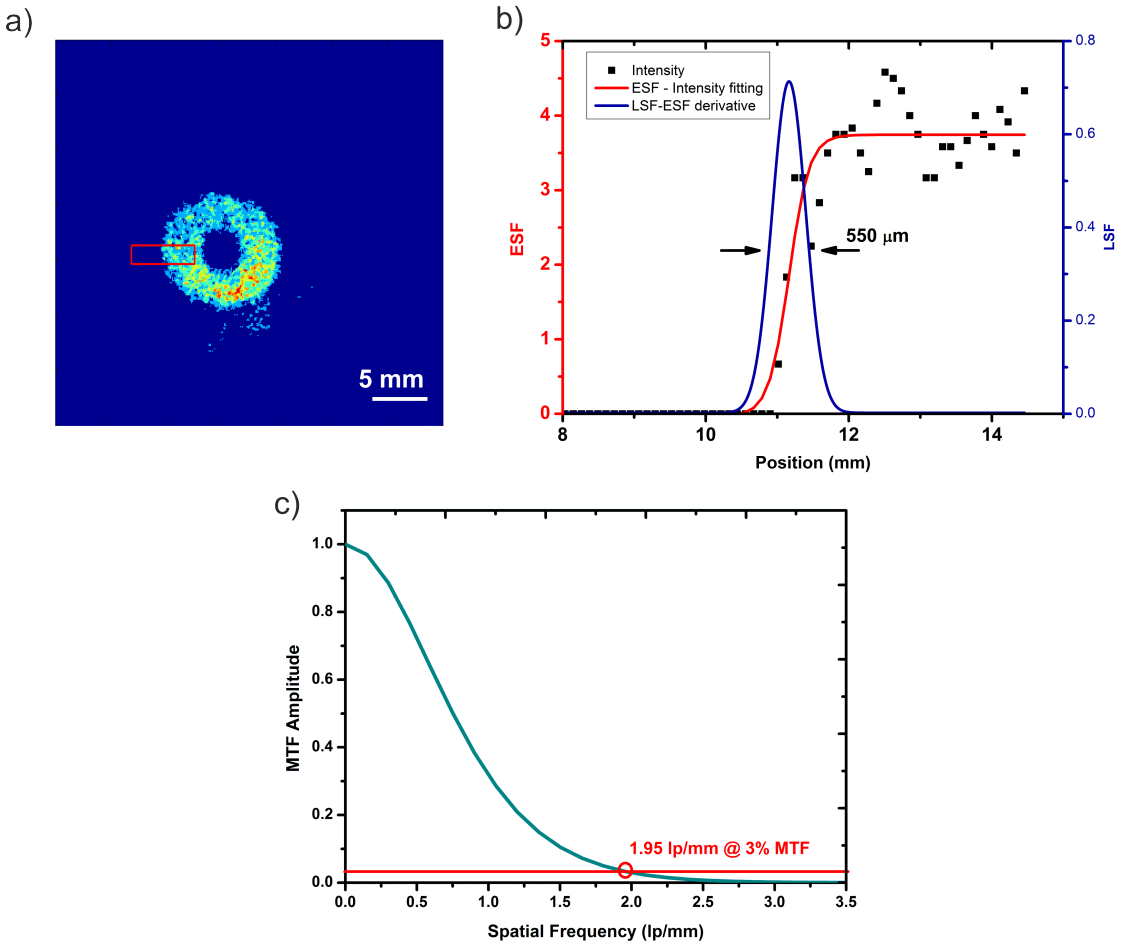

Figure 4.13: a) Fluorescence image of the stainless steel gasket with a magnification of ×3. The selected region for spatial resolution calculations is delimited with a red rectangle. b) ESF and LSF used to determine the position resolution of the image in a); c) MTF corresponding the LSF shown in b).

4.2.2 Cultural Heritage - Illuminated Manuscript

Historically, an illuminated manuscript is a document which includes ornamental borders, illustrations, and other decoration motifs besides the text itself.

The word *manuscript* typically refers to any document produced manually, through handwriting, whereas the *illumination* term is related with the frequent incorporation of gold or sometimes silver onto the manuscript. The brilliant colours based on these elements gives often the impression that the manuscript is being light up, i.e., illuminated.

Over the years the scientific community has been increasingly interested in the preservation of cultural heritage objects. The application of various spectroscopic techniques, combined with the efforts of scientists, restorers and conservators, contributed a lot for this goal, namely in the study of illuminated manuscripts, which are very important subjects

within cultural heritage mainly due to their historical and artistic importance, as is easily checked by highly varied existing literature in the area [117–119].

The study of the pigments that make up a particular manuscript is usually the aim of the research concerning the illuminated manuscripts. Through them it is often possible to identify the method used by the artist during the elaboration of the document as well as the identification of it age, which can be useful during the process of restoration, cleaning and conservation, if needed.

The XRF is the more popular diagnostic technique for the conservation of works of art since it is a well-established technique for elemental analysis. It can identify many elements in an efficient way, depending on the system used and is non-destructive in nature [117, 118].

By using the EDXRF imaging system based on the 2D-THCOBRA device, fluorescence images of an excerpt from an illuminated, book of tides, from the 15th-16th century, were acquired.

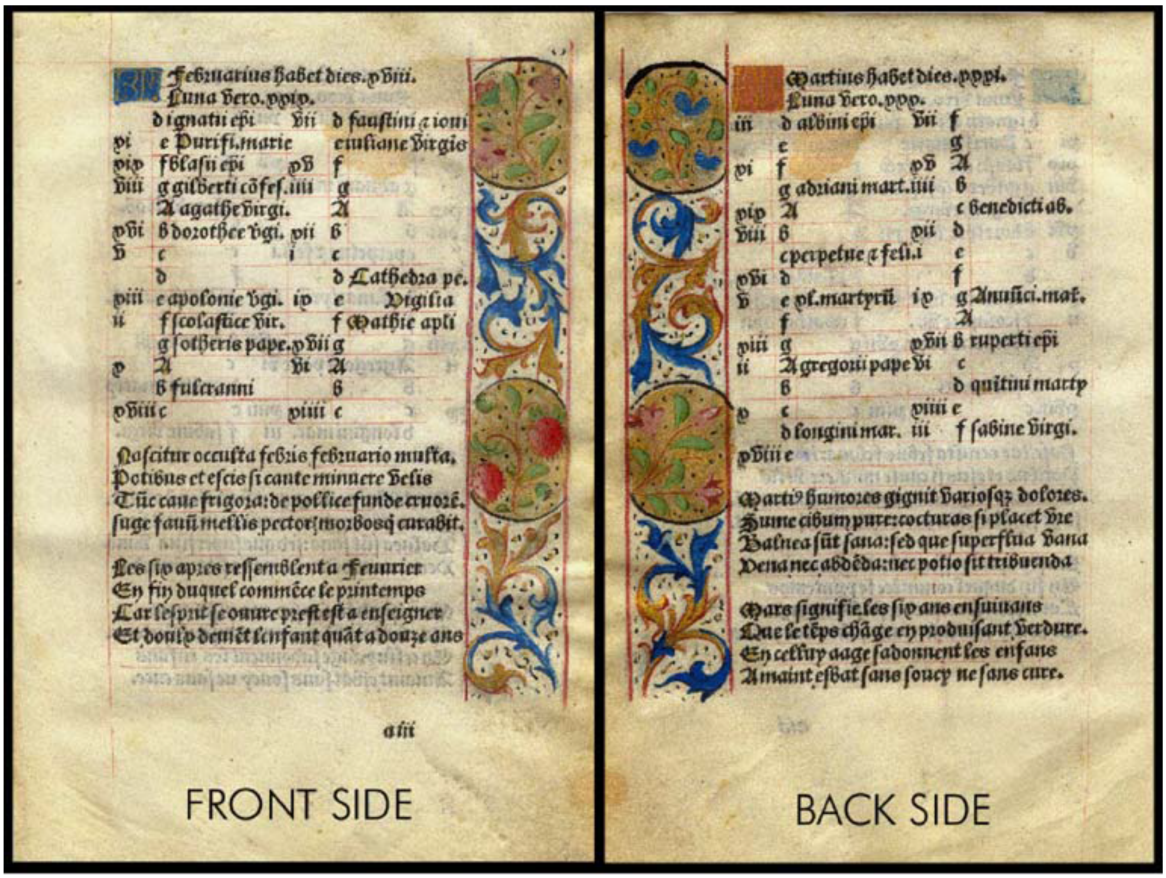

Figure 4.14: Photo of the front and back side of illuminated manuscript analysed [117].

The sample

Figure 4.14 shows a photo of the analysed sample. It consists of a sheet of parchment written and painted on both sides. The text, first written in Latin and translated in French, exhibits a black colour. Some red/pink marks, which seem to serve as rulers to write in alignment, are visible along the manuscript.

On the right margin of the front side and on the left margin of the back side of the parchment some illuminations depict some rural/pastoral motives, like strawberries and floral motifs inside gilded circles. Between the gilded circles, some scroll works are drawn in blue and gilded ink.

These illuminated paintings are confined to a region between two red/pink trace lines, similar to the rules.

Analysis and Discussion

The X-rays used to irradiate the sample were first generated with the low power Mo-tube introduced before, from Oxford Instruments®. The X-rays emitted by the illuminated parchment were focused by the 1 mm pinhole camera which is part of the developed system, as mentioned in section 4.2. The spectra and the images acquired were collected by the 2D-THCOBRA detector.

Prior to the analysis of the parchment some studies were done using μ-Raman spectroscopy, μXRF and μ-X-ray diffraction, by Van Der Snickt, *et al.*, in 2008 [117], which facilitate the interpretation of the obtained results. For details concerning these analysis, please see ref. [117].

The first image obtained with the experimental setup described above, is depicted in Figure 4.15 and was acquired with a magnification of about $\times 2.5$. The acquisition was performed with the X-ray tube operating at 25 kV and 1 mA, and the acquisition time was of about 15 min. The spectrum (Figure 4.15 b)) shows a Ca peak, which can be attributed to the chalk used during the preparation of the parchment [117]. Selecting in the spectrum a ROI corresponding to the characteristic energies of Ca, we can obtain an image of it spatial distribution in the irradiated area of the parchment. The distribution of Ca is depicted in 4.15 c). As can be seen, this element is almost uniformly distributed along the irradiated area, noticing only slightly more strength in the area where it has been painted. This is because chalk was often used as a filler in paint, as mentioned in ref. [117].

By selecting in the spectrum another ROI corresponding to the second peak in the spectrum (Figure 4.15 b)), an image showing part of the scroll works appear (Figure 4.15 d)). If we look carefully to the picture, we can see that the region of these scroll works painted with blue ink appears to be more intense that the region corresponding to the gilded one. According to ref. [117], the blue ink is composed by azurite, which is a basic copper(II)

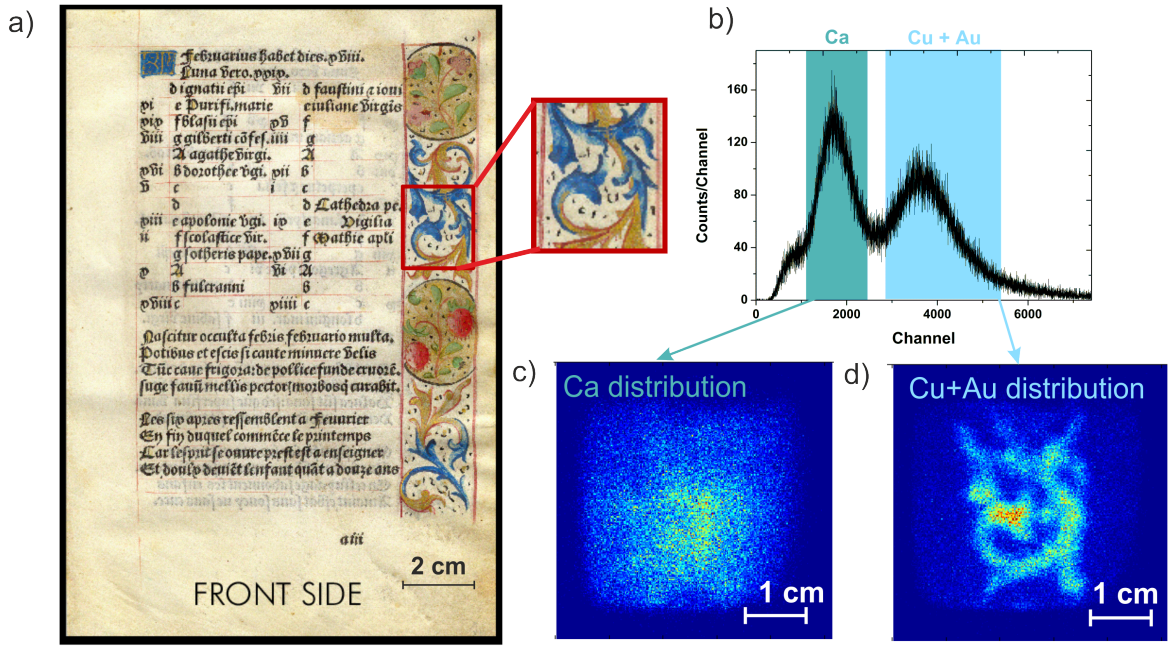

Figure 4.15: a) Photo of the front side of the illuminated parchment with a detailed view on the analysed region. b) Total pulse-height spectra with different ROI selected depending on the elements to be mapped and the corresponding individual elemental images of c) Ca and d) Cu and Au spatial distributions.

carbonate, one of the important blue pigments in European painting until the eighteenth century. Concerning the gilded region, we should expect to see in the spectrum the L-lines of Au. However, in that case it was not possible to distinguish the characteristic K-lines of Cu (8 keV) from the characteristic L-lines of Au (10 keV), mainly due to the energy resolution of the detector at that time. Concerning the difference in the Cu/Au intensities observed in the image, this is because in the case of Au we are detecting the L-lines, which are much less intense than the K-lines of Cu.

In an attempt to increase the flux of photons reaching the detector per second without changing the diameter of the pinhole, it was used a high power X-ray tube[5](with 50 kV and 60 mA maximum voltage and current, respectively). The results are shown in Figure 4.16. The acquisition time for this measurement was of about 60 min. Although we initially expected a much shorter acquisition time than the one achieved with the low power tube, we found that the acquisition time was not much different to obtain images with the same number of events registered. This is because the high power tube is much bigger than the previous one which makes it difficult to place near the sample and the detector. Besides that, the focal spot of the tube is also smaller than the low power one, which force one to put it at a certain distance of the sample to be possible to irradiate the whole region of the sample that we intend to analyse. Thus, the greater the tube-to-sample distance the lower the efficiency of

[5]PW 1830 X-ray generator, from Philips®. The X-ray tube can operate with a maximum power of 3kW.

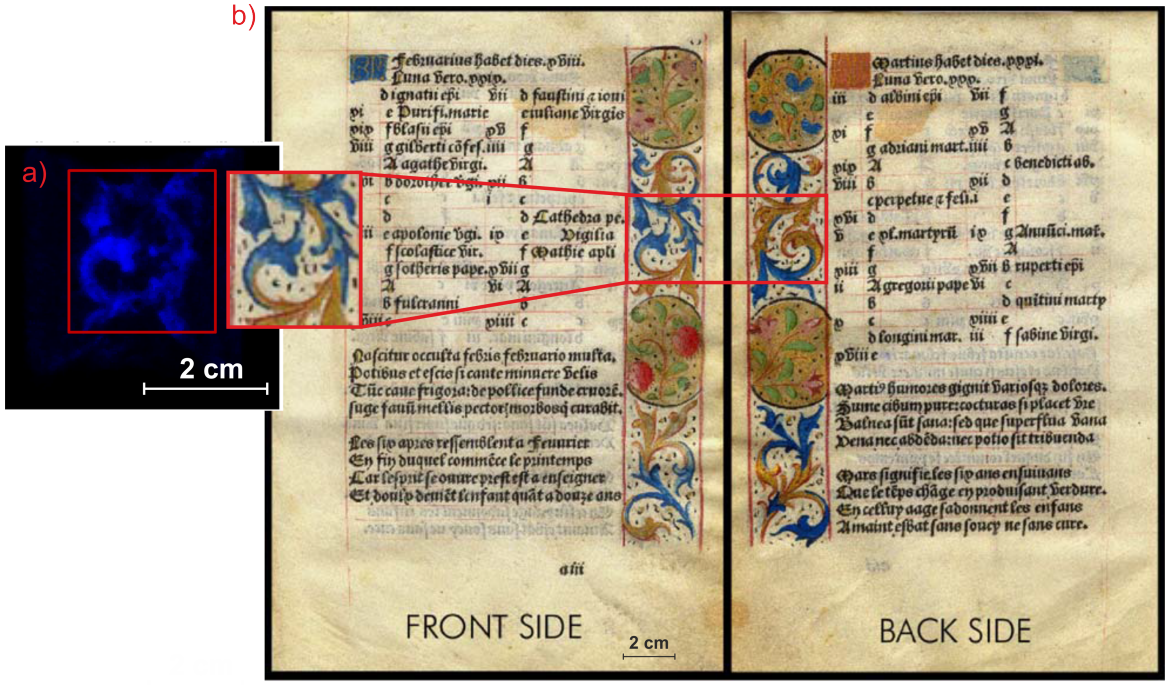

Figure 4.16: a)Acquired image with a detail of the parchment irradiated area. b) Photo of the front and back side of the illuminated parchment, showing that when in the front we have a gilded area, on the back side it is painted with blue paint.

excitation of the sample elements will be, greatly due to absorption in the air, which, at the end, will also limit the flow of photons that reach the detector.

Figure 4.16 shows the image obtained with the EDXRF imaging system based on the 2D-THCOBRA detector working with the high power X-ray tube. The measurements were done with the X-ray tube operating at 30 kV and 40 mA. The tube was placed about 30 cm away from the sample.

The image obtained was acquired with a magnification of about $\times 2.7$ and corresponds to the same analysed region as before (Figure 4.16 a)). Similarly to what happened at that time, it is still not possible to distinguish the distribution of Cu, separately from the distribution of Au, thus we have decided to represent the distribution of both elements together. The energy resolution is not enough to resolve the characteristic energies of both elements. Nevertheless, there is another issue which does not allow to obtain different images for Cu and Au elements. As you can see in the figure, the margins of the front and back side of the parchment are complementary with respect to the pigments. The shape of the motifs is the same both front and back but, when these are blue on one side, are gilded on the other, and vice versa.

This means that when we expect to have Au peaks in the spectrum, correspondent to the gilding, we will also have a significant Cu peak from the back of the parchment, in the spectrum. Concerning the image with the spatial distribution of Cu, we will see always the Cu from the front and the back of the parchment, and the same will happen for the Au

elemental map distribution. Thus, both images will have always the same appearance. This is due to the penetration depth of the X-rays through the parchment sheet, which can lead to some interpretation problems.

4.3 Discussion - MHSP vs. THCOBRA based system

Both EDXRF imaging systems developed and discussed during this work consist of some basic functional components, the X-ray excitation source, the sample, the detector and the pinhole camera. The properties and performances of the systems presented differ mainly upon the intrinsic characteristics from the detector used in each case as well as the characteristics resulting from the operation of the complete system.

The selective determination of elements in samples, using X-ray spectrometry depends upon resolving the spectral lines emitted by the various elements into separate components. This process requires a energy dispersive device. The biggest difference in the results obtained with the two systems proposed relies on the detector used in each case.

Both detectors are energy dispersive and based upon the ability of the detector to create signals proportional to the incident X-ray photon energy, however they present a lot of different characteristics, as was shown in chapter 3 which will have a great importance on the obtained results.

It is known that the better the energy resolution of the detector, the better the accuracy of the results will be, obtained during the XRF analysis, which will lead to a more accurate mapping of the elements in the sample. The energy resolution offered by gaseous detectors is rather limited by their physical operation principle, as described and explained in section 3.1.1.2. However, some of them may be better than others, thus, an important thing to do is to compare the energy resolution obtained with the two detectors used. This comparison will be done based on the results presented in sections 3.1.1.2 and 3.1.2.2, corresponding respectively to the 2D-MHSP and 2D-THCOBRA detector.

Concerning the discussion and results obtained previously for the energy resolution of both detectors, it is known that, in both cases, it is limited due to fluctuations in the formation of the primary electron cloud and due to fluctuations in the avalanche process. These fluctuations assume greater or lesser importance in the intrinsic energy resolution of the detector, depending on the filling gas used in the detector. Thus, it was found that the energy resolution values obtained in the case of the 2D-MHSP, filled with Xe, were much better than the ones achieved for the 2D-THCOBRA detector, filled with Ne/5%CH_4. By using the equations 3.12 and 3.22 the energy resolution for 5.9 keV was determined and was achieved to be 17 % and 22 %, for the 2D-MHSP and 2D-THCOBRA detectors, respectively.

The energy resolution of the developed systems is until now their major drawback for the EDXRF imaging applications. However, they can positively compete with other FF-XRF imaging systems based on pixel detectors introduced in the **State of the Art of EDXRF Imaging systems** (chapter 1, section 1.2.2), such as: the XRF imaging system based on the Medipix2/Timepix detector and the FF-XRF imaging system based on PILATUS detector, as shown in Table 1.2.

After performing the measurements with the system, spectrum evaluation deserves our greatest attention, since it will be critical to choose the ROI which will be used to obtain the images of the spatial distribution of elements in the sample. In EDXRF, the characteristic radiation of a particular line can be described by a Gaussian function. When the peaks do not overlap in the spectrum, the choice of a ROI in the spectrum seems to be the best and the simplest way to identify the characteristic energy of an element present in the sample. The selected ROI must correspond to the characteristic energy of the particular element which we want to see and evaluate it distribution in the sample. This method proved to be sufficient in the analysis of some analysed samples, however in cases such as the analysis of the tile (with the 2D-MHSP based system) and the illuminated manuscript (2D-THCOBRA based system), it proved not to be the most suitable choice. This is because, in these cases, the wanted element peaks overlapping is such, that they become virtually indistinguishable in the spectrum. In such cases, fitting methods can be applied to the spectral data in order to fit theoretical profiles at the measured spectra and find the area of the individual profiles [8].

Another important feature of the system is related with their spatial resolution. In the chapter 3, some studies concerning the spatial resolution of both systems were presented. It was found that the position resolution of the imaging systems proposed in this work depends mainly on the intrinsic resolution of the detectors and also on the pinhole diameter and magnification used during acquisitions. The studies presented in chapter 3, show that the intrinsic position resolution of the 2D-THCOBRA detector is not so good as the one achieved with the Ne/5%CH_4, since it is strongly limited by the photoelectron range in the Ne mixture. Concerning the EDXRF imaging systems spatial resolution, the pinhole used was much bigger in the case of the 2D-THCOBRA based system than the one used in the system based on the MHSP. This was mainly because of the difference in the active area of the detectors. In the case of the 2D-THCOBRA it was necessary to use a bigger pinhole since it was mandatory to increase the photon flux passing through the pinhole to reach the detector, for that active area.

The position resolution obtained in the two systems is not comparable, because they are much different in what concerns to the MPGD structure dimension and granularity, filling gas and active area, as well as in the size of the pinhole used. Also, the spatial resolution obtained with both systems are not so good as the spatial resolution obtained with the systems listed in Table 1.2, however, what matters here is that the use of one system or another, is appropriate

or not, depending on the sample, not only with respect to its composition but also on its size and required acquisition time.

Because of the simplicity of an X-ray tube instrument together with the availability of a high photon output flux by using direct tube excitation, it was chosen to equip our systems with an X-ray tube, which has the aim of work as a direct excitation source. The drawback associated with the use of the X-ray tube as the excitation source is related with the less flexible selection of the excitation energy, however by using an appropriate filter between tube and sample, one can obtain an optimal excitation. With direct tube excitation, low powered X-ray tubes can be used. They are usually easily to work with, most of the times are air cooled, very compact and less expensive than the high power X-ray tubes.

Almost all analyses and acquisitions shown in this work were carried out exciting the sample with a low power X-ray tube. There was only one acquisition performed with the high powered tube to icrease the photons flux arriving at the detector.

A common way to avoid the intense Bremsstrahlung continuum from the X-ray tube and optimize the excitation conditions is to use secondary target excitation. The secondary target is placed between the tube and the sample. Thus, it is possible to efficiently excite the elements of the sample by selecting a secondary target which has characteristic lines just above the absorption edges of the elements of interest in the sample. Thus it has some obvious advantages over direct tube excitation, the excitation energy can be chosen, which means that one can get an optimized and near monochromatic excitation, providing a better selectivity and an improved sensitivity to the system. In that case, to compensate the intensity losses, a high power tube must be used.

Neither a filter or a secondary target were used during this work to optimize the excitation process of the elements with more interest in the samples. However, the use of one of those methods, depending on the sample to be analysed, should be considered as one of the next steps to improve the results obtained with the proposed systems.

CHAPTER 5

CONCLUSIONS AND FUTURE WORK

5.1 Conclusions

In this work, two EDXRF imaging systems based on two different concepts of position sensitive Micropattern Gas Detectors were developed, the 2D-MHSP and the 2D-THCOBRA detectors. Applications of these systems to EDXRF imaging were studied and explored, during the course of the work. Although they are based on different detector concepts, they both use resistive lines charge divider as the position readout system. This resistive lines implementation was done, in the MPGDs based structures, in two orthogonal directions, in order to get 2D detection.

Taking advantage of the photon counting capability of these detectors, where position and energy response are stored, application studies using imaging capability of the devices together with EDXRF technique were done.

The major difference between both systems is related with the based production material, detection areas and granularity of the structures 2D-MHSP and 2D-THCOBRA. They present, respectively, active areas of about 9 cm^2 and 100 cm^2, being the first produced in a 50 μm Kapton foil with a copper coating in both sides and the second in standard printed circuit board (PCB) technology. Although with limited granularity, these structures, based on PCB board technology, are more robust and easy to produce in large size.

Similarly to the most imaging systems developed for X-ray fluorescence applications, those presented and proposed in this work are essentially constituted by an X-ray tube, a pinhole and an energy and position sensitive detector. Most of the characteristics associated with the performance of such systems are closely related to the detectors used: their detection efficiency, energy resolution and linearity, gain performance and intrinsic spatial resolution.

Concerning those characteristics it was found that the Xe gas, used to fill the 2D-MHSP detector, is a better choice for this kind of applications, when compared to the Ne/5%CH_4 used in the 2D-THCOBRA detector. Not only because it allows for a higher detection efficiency for the range of energies used, but also because it has shown better results for both the energy resolution and intrinsic position resolution.

The detectors have shown energy resolutions of about 17 % and 22 % for 5.9 keV X-ray photons, for the 2D-MHSP and for the 2D-THCOBRA, respectively.

Regarding the position resolution for the 2D-MHSP detector, the intrinsic spatial resolution is of about 130 μm for the X dimension and about 250 μm for the Y dimension, for 8 keV X-rays, as reported in [63]. In the case of the position resolution of the 2D-THCOBRA detector, it was limited to about 2.3 mm for the X dimension and 2.7 for the X dimension, due to the high photoelectron range in the used mixture (Ne/5%CH_4) produced by X-ray photons with higher energies.

Although these resolution values are important and contribute a lot to the final system performance, they do not correspond to the position resolution obtained when the whole

system is used. This is because we have to consider the contribution of the pinhole to the spatial resolution as well as the magnification factor. During the development of this work it was found that the diameter of the pinhole used has a strong influence on the photons flux reaching the detector per unit of time, but also in the position resolution obtained. The larger the diameter of the pinhole the worse is the resolution of the system. The spatial resolution of the system was also determined as a function of image magnification due to the use of pinhole optics. As expected, the increase of image magnification improves the spatial resolution since the contribution of the position resolution of the detector is smaller. The study was performed with the 2D-MHSP based system. The spatial resolution (FWHM of the LSF) of the experimental system varied between 900 and 400 μm for image magnifications between 1 and 4. The contribution of oblique penetration of X-ray photons was also studied and was found to be negligible for high values of magnification.

After evaluating independently the system's components it was time to apply them by analysing some samples. The samples first used had known composition which allowed and helped to validate the system's performance. The response of the system was evaluated based on the results that were expected to obtain by knowing the sample.

The results obtained from the first implementation of both systems using known samples have demonstrated their applicability, since it enabled the identification of the different elements presented and elucidated their spatial distributions in the irradiated sample.

After system's validation, different and more complex samples were analysed. Some of them had some relevant cultural heritage importance, such as: the XVII century glazed tile from the Odivelas Conventry, at Lisboa, analysed with the 2D-MHSP based system, and the illuminated parchment from the 15th-16th century, analysed using the 2D-THCOBRA based system.

The energy resolution offered by both systems have shown some limitations when analysing the cultural heritage samples. This was because some of the elements from the samples, which correspond largely to the constituents of the pigments used in the object's decoration, have very close characteristic energies, which makes difficult to obtain the image with the spatial distribution of each element separately.

However, in the case of the glazed tile, the 2D-THCOBRA based system allow to perform the Pb distribution in the glazed tile, and also to see the distribution of Fe (from the yellow pigment) together with the distribution of Co (from the blue pigment). It was also possible to identify, in one of the analysed regions of the sample, the distribution of the L-lines of Sb, which are the fingerprint of the yellow pigment.

Furthermore, in the case of the illuminated parchment analysis, performed with the 2D-THCOBRA based system it was possible to identify the presence of Ca, corresponding to the parchment and the Cu K-lines and Au L-lines distribution.

The most successful implementation of the EDXRF system based on the MHSP was the

study concerning the analysis of human teeth treated with dental amalgam. The results obtained from the implementation of the system have demonstrate its applicability since it was possible to identify chemical elements in the composition of the samples, such as Ca, Zn and Hg and image their spatial distribution on the samples. The studied samples have shown different elemental diffusion patterns along the tooth. Hg element is present in treated teeth, especially in the regions immediate surrounding the carious cavity that was in contact with the metallic amalgam. It was observed in one of the treated teeth (sample C) that the Hg drifts throughout the tooth to the root region, which might be due to hydroxyapatite crystal defects along the tooth. A higher content of Zn was found in the inner region and along the nerve canal, for the restored teeth, and in the region surrounding amalgam, possibly due to amalgam contamination. In the healthy tooth, the content of Ca and Zn was found to be more or less uniformly distributed. It was also verified in this work that exists a drift mechanism of Hg and Zn from the amalgam to the teeth tissues exists. The results show an increase of Zn and Hg contents for the dentine surrounding regions. This diffusion can be more or less relevant and deep, especially in the case of Hg diffusion, if there were some defects over the hydroxyapatite crystals that compose the teeth tissues.

The major advantages of the proposed systems are the high sensitive area (which can eventually reach later to 50×50 cm^2) and with the low cost of the detectors used. The cost associated with the prototypes of microstructures is valued at about 3€/cm^2, which makes it tremendously competitive against most of the energy dispersive detectors, even with the readout electronic needed. We should keep in mind that this cost can be further decreased for large production by an industrialized process. Thus, even against systems with a better resolution, the proposed systems can be competitive, offering a larger detection area at a lower price.

5.2 Future Work

This work has intended to propose a new solution for large area EDXRF imaging. First studies were performed and presented demonstrating its applicability. Nevertheless there are many issues to be studied in order to improve the different proposed systems performance.

Future work will aim at improving the results obtained with both EDXRF imaging systems proposed based on MPGDs.

There are a plenty of things that we can do to further improve and optimize the systems in which respects to both system components and software dedicated to the acquisition, processing and visualization of the results.

The minimization of the fluorescence X-ray absorption between the sample and the detector is essential for soft X-rays detection. This can be made by filling this distance with He, since the attenuation coefficient for soft X-rays is largely smaller for He when compared

with air.

Optimization of the energy resolution is also crucial for that kind of applications, thus, for that reason, future work will also focus on the improvement of the gas purification system based on getters, in the case of the 2D-MHSP detector. Concerning the 2D-THCOBRA detector, we intend to modify it in order to be used as a sealed detector, bearing in mind that the materials therein should be as clean as possible. This is important if we want to use a higher Z filling gas as Xe or Kr, which are much more expensive than the Ne mixture used during this work. To keep the gas clean the implementation of a purification system based on getters to this detector, need to be done. The changing of the gas, in principle, improve significantly the intrinsic energy resolution of the 2D-THCOBRA detector as well as it detection efficiency and the intrinsic position resolution, making it more suitable for EDXRF imaging applications.

Another way to circumvent the not so good energy resolution offered by the systems is to use filters or secondary targets, between the X-ray tube and the sample, which will optimize the excitation energy for a given element in the sample. Moreover fitting methods can be applied to the spectral data in order to easily identify the characteristic energy of the individual elements in the sample in the spectrum.

The development of more portable and robust systems is also one of our future goals. Larger sensitive detection areas (up to 30×30 cm^2) are possible and will be considered for applications requiring large area analysis with the best acquisition time possible. This kind of systems can be an excellent choice, for instance, in the art history field to large area paintings analysis.

The possibility of developing a system for X-ray Fluorescence Computed Tomography imaging, based on these kind of energy dispersive and position sensitive detectors is also being studied.

More applications will be considered in order to further evaluate the performance of both systems in the analysis of different nature samples.

REFERENCES

[1] E. Bertin, "*Principles and Practice of X-ray Spectrometric Analysis*", Plenun Press, 1978.

[2] R. Jenkins and J. d. Vries, "*Pratical X-ray Spectrometry*", The Macmillan Press LTD, 1972.

[3] R. Jenkins, R. Gould and D. Gedcke, "*Quantitative X-ray spectrometry*", Marcel Dekker, Inc., 1995.

[4] K. Janssens, Chapter 4: X-ray based methods of analysis, Chapter 4, pp. 129-226, in *Non-destructive Microanalysis of Cultural Heritage Materials*, Elsevier, 2004.

[5] W. R. Leo, "*Techniques for Nuclear and Particle Physics Experiments: A How-to Approach*", Springer-Verlag, 1994.

[6] http://physics.nist.gov/PhysRefData/Xcom/Text/XCOM.html, XCOM: Photon Cross Sections Database. Access date: January, 2013.

[7] G. F. Knoll, "*Radiation detection and measurement*", John Wiley & Sons, 2010.

[8] R. E. V. Grieken and A. A. Markowicz, "*Hanbook of X-ray Spectrometry: Methods and Techniques*", Marcel Dekker, Inc., 1993.

[9] C. G. Barkla, "*Nobel Lecture: Characteristic Rontgen Radiation*", The Nobel Prize in Physics 1917, 1920.

[10] R. Tertian and F. Claisse, "*Principles of Quantitative X-ray Fluorescence Analysis*", Heyden & Son Ltd, 1982.

[11] M. Siegbahn, The Nobel Prize in Physics 1924, 1924.

[12] http://www.iupac.org/, IUPAC: International Union of Pure and Applied Chemistry. Access date: February, 2013.

[13] J. Hubbbel et al., "*A review, bibliography, and Tabulation of K, L and Higher atomic shell X-ray fluorescence Yields*", J. Phys. Chem., vol. 23, no. 2, 1994.

[14] M. G. Vasin et al., "*Energy-resolved x-ray imaging*", Spectrochimica Acta Part B-Atomic Spectroscopy, vol. 62, no. 6-7, pp. 648-653, 2007.

[15] M. Alfeld et al., "*The Use Of Full-Field XRF For Simultaneous Elemental Mapping*", X-Ray Optics and Microanalysis, Proceedings, vol. 1221, pp. 111-118, 2010.

[16] I. Ordavo et al., "*A new pnCCD-based color X-ray camera for fast spatial and energy-resolved measurements*", Nuclear Instruments & Methods in Physics Research Section a-Accelerators Spectrometers Detectors and Associated Equipment, vol. 654, no. 1, pp. 250-257, 2011.

[17] V. Tichy et al., "*X-ray fluorescence imaging with pixel detectors*", Nuclear Instruments & Methods in Physics Research Section a-Accelerators Spectrometers Detectors and Associated Equipment, vol. 591, no. 1, pp. 67-70, 2008.

[18] P. Kraft et al., "*Performance of single-photon-counting PILATUS detector modules*", Journal of Synchrotron Radiation, vol. 16, pp. 368-375, 2009.

[19] C. Broennimann et al., "*The PILATUS 1M detector*", Journal of Synchrotron Radiation, vol. 13, pp. 120-130, 2006.

[20] H. Toyokawa et al., "*Energy-resolved X-ray imaging method with a counting-type pixel detector*", Nuclear Instruments & Methods in Physics Research Section a-Accelerators Spectrometers Detectors and Associated Equipment, vol. 650, no. 1, pp. 84-87, 2011.

[21] H. P. Haberkorn, "*Basics, Possibilities and Limitations of the Microscopic X-Ray Fluorescence Analysis*", Microchimica Acta, vol. 133, no. 1-4, pp. 51-58, 2000.

[22] A. G. Revenko, "*Specific features of X-ray fluorescence analysis techniques using capillary lenses and synchrotron radiation*", Spectrochimica Acta Part B-Atomic Spectroscopy, vol. 62, no. 6-7, pp. 567-576, 2007.

[23] P. J. Sheilds et al., "*Overview of Policapillary X-ray optics*", X-ray Optical systems, 2002.

[24] F. Adams, K. Janssens and A. Snigirev, "*Microscopic X-ray fluorescence analysis and related methods with laboratory and synchrotron radiation sources*", Journal of Analytical Atomic Spectrometry, vol. 13, no. 5, pp. 319-331, 1998.

[25] K. Janssens et al., "*A micro-XRF spectrometer based on a rotating anode generator and capillary optics*", Spectrochimica Acta Part B-Atomic Spectroscopy, vol. 51, no. 13, pp. 1661–1678, 1996.

[26] S. Bichlmeier et al., "*Component selection for a compact micro-XRF spectrometer*", X-Ray Spectrometry, vol. 30, no. 1, pp. 8-14, 2001.

[27] http://www.speciation.net/Database/Instruments/Edax-Inc/Eagle-III-Probe-;i1560, Instrument database: Edax inc. - Eagle III μprobe, EVISA. Access date: February, 2013.

[28] H. Bronk et al., "*ArtTAX-a new mobile spectrometer for energy-dispersive micro X-ray fluorescence spectrometry on art and archaeological objects.*", Fresenius J Anal Chem, vol. 371, no. 3, pp. 307-16, 2001.

[29] G. Vittiglio et al., "*A compact μ-XRF spectrometer for (in situ) analyses of cultural heritage and forensic materials*", Nuclear Instruments & Methods in Physics Research Section B-Beam Interactions with Materials and Atoms, vol. 213, pp. 693-698, 2004.

[30] R. Alberti et al., "*Elemental mapping by means of an ultra-fast XRF spectrometer based on a novel high-performance monolithic array of Silicon Drift Detectors*", Nuclear Instruments & Methods in Physics Research Section a-Accelerators Spectrometers Detectors and Associated Equipment, vol. 580, no. 2, pp. 1004-1007, 2007.

[31] R. G. Figueroa et al., "*Characteristics of a low cost and portable large area X-ray fluorescence imaging system*", Submitted to Spectrochimica Acta Part B-Atomic Spectroscopy, 2012.

[32] O. Scharf et al., "*Compact pnCCD-Based X-ray Camera with High Spatial and Energy Resolution: A Color X-ray Camera*", Analytical Chemistry, vol. 83, no. 7, pp. 2532-2538, 2011.

[33] J. Uher, G. Harvey and J. Jakubek, "*X-Ray Fluorescence Imaging With the Medipix2 Single-Photon Counting Detector*", Ieee Transactions on Nuclear Science, vol. 59, no. 1, pp. 54-61, 2012.

[34] http://aladdin.utef.cvut.cz/ofat/methods/TimePixCalibration/index.htm, J. Jakubek, IEAP. Acess date: June, 2013.

[35] M. Alfeld et al., "*Application of a PILATUS detector as camera for Full-Field-(FF)XRF Imaging*", Poster Comunication presented in the Conference Synchrotron Radiation in Art and Archaeology (SR2A), 2012.

[36] N. Ishida et al., "*Fano Factor in Xenon*", Physical Review A, vol. 46, no. 3, pp. 1676-1679, 1992.

[37] http://consult.cern.ch/writeup/magboltz/, S. Biagi, MIP program, Access date: March, 2013.

[38] U. Fano, "*Ionization Yield of Radiations. II. The Fluctuations of the Number of Ions*", Physical Review A, vol. 72, no. 1, pp. 26, 1947.

[39] I. G. Ferreira, J. G. Herrera and L. Villaseñor, "*The Drift Chambers Handbook, introductory laboratory course (based on, and adapted from, A H Walenta's course notes)*", Journal of Physics: Conference Series, vol. 18, pp. 346361, 2005.

[40] G. Charpak et al., "*Use of Multiwire Proportional Counters to Select and Localize Charged Particles*", Nuclear Instruments & Methods, vol. 62, no. 3, pp. 262, 1968.

[41] L. Shekhtman, "*Novel position-sensitive gaseous detectors for X-ray imaging*", Nuclear Instruments & Methods in Physics Research Section a-Accelerators Spectrometers Detectors and Associated Equipment, vol. 522, no. 1-2, pp. 85-92, 2004.

[42] F. Sauli and A. Sharma, "*Micropattern gaseous detectors*", Annual Review of Nuclear and Particle Science, vol. 49, pp. 341-388, 1999.

[43] A. Oed, "*Micro pattern structures for gas detectors*", Nuclear Instruments & Methods in Physics Research Section a-Accelerators Spectrometers Detectors and Associated Equipment, vol. 471, no. 1-2, pp. 109-114, 2001.

[44] L. Shekhtman, "*Micro-pattern gaseous detectors*", Nuclear Instruments & Methods in Physics Research Section a-Accelerators Spectrometers Detectors and Associated Equipment, vol. 494, no. 1-3, pp. 128-141, 2002.

[45] A. Oed, "*Position-Sensitive Detector with Microstrip Anode for Electron Multiplication with Gases*", Nuclear Instruments & Methods in Physics Research Section a-Accelerators Spectrometers Detectors and Associated Equipment, vol. 263, no. 2-3, pp. 351-359, 1988.

[46] J. F. C. A. Veloso et al., "*Application of a microstrip gas counter in energy-dispersive x-ray fluorescence analysis*", X-Ray Spectrometry, vol. 26, no. 4, pp. 237-243, 1997.

[47] J. E. Bateman et al., "*A gas microstrip detector for X-ray imaging with readout of the anode by resistive division*", Nucl. Instr. Meth. A, vol. 477, no. 1-3, pp. 29-36, 2002.

[48] F. Sauli, "*GEM: a new concept for electron amplication in gas detectors*", Nucl. Instr. Meth. A, vol. 386, no. 531-534, 1997.

[49] G. P. Guedes et al., "*Two-dimensional GEM imaging detector with delay-line readout*", Nucl. Instr. Meth. A, vol. 513, no. 3, pp. 473-483, 2003.

[50] A. Bressan et al., "*Two-dimensional readout of GEM detectors*", Nucl. Instr. Meth. A, vol. 425, no. 1-2, pp. 254-261, 1999.

[51] C. A. B. Oliveira et al., "*Simulation of VUV electroluminescence in micropattern gaseous detectors: the case of GEM and MHSP*", Journal of Instrumentation, vol. 7, 2012.

[52] A. Bondar, A. Buzulutskov and L. Shekhtman, "*High pressure operation of the triple-GEM detector in pure Ne, Ar and Xe*", Nucl. Instr. Meth. A, vol. 481, pp. 200 - 203, 2002.

[53] A. Buzulutskov et al., "*Further studies of the GEM photomultiplier*", Nucl. Instr. Meth. A, vol. 442, no. 1-3, pp. 68-73, 2000.

[54] F. Sauli, "*Progress with the gas electron multiplier*", Nucl. Instr. Meth. A, vol. 522, no. 1-2, pp. 93-98, 2004.

[55] B. Ketzer et al., "*Performance of triple GEM tracking detectors in the COMPASS experiment*", Nucl. Instr. Meth. A, vol. 535, no. 1-2, pp. 314-318, 2004.

[56] S. Lami et al., "*A triple-GEM telescope for the TOTEM experiment*", Nuclear Physics B-Proceedings Supplements, vol. 172, pp. 231-233, 2007.

[57] J. F. C. A. Veloso, J. M. F. Santos and C. A. N. Conde, "*A proposed new microstructure for gas radiation detectors: The microhole and strip plate*", Review of Scientific Instruments, vol. 71, no. 6, pp. 2371-2376, 2000.

[58] J. F. C. A. Veloso et al., "*High-rate operation of the Micro-Hole and Strip Plate gas detector*", Nucl. Instr. Meth. A, vol. 580, no. 1, pp. 362-365, 2007.

[59] H. N. Luz et al., "*MHSP operation in pure xenon*", Nucl. Instr. Meth. A, vol. 552, no. 3, pp. 259-262, 2005.

[60] J. F. C. A. Veloso et al., "*Application of the microhole and strip plate detector for neutron detection*", Ieee Transactions on Nuclear Science, vol. 51, no. 5, pp. 2104-2109, 2004.

[61] H. N. Luz et al., "*Micro-hole and strip plate (MHSP) operation in CF4*", Nucl. Instr. Meth. A, vol. 580, no. 1, pp. 286-288, 2007.

[62] H. N. Luz et al., "*A simple X-ray position detection system based on a MHSP*", Nucl. Instr. Meth. A, vol. 580, no. 2, pp. 1083-1086, 2007.

[63] H. N. Luz et al., "*MHSP with position detection capability*", Nucl. Instr. Meth. A, vol. 573, no. 1-2, pp. 191-194, 2007.

[64] H. N. Luz et al., "*Single Photon Counting X-Ray Imaging System Using a Micro Hole and Strip Plate*", Ieee Transactions on Nuclear Science, vol. 55, no. 4, pp. 2341-2345, 2008.

[65] A. L. M. Silva et al., "*EDXRF imaging of Pb in glazed ceramics using a micropattern gas detector*", Analytical and Bioanalytical Chemistry, vol. 395, no. 7, pp. 2073-2080, 2009.

[66] R. Chechik et al., "*Thick GEM-like hole multipliers: properties and possible applications*", Nuclear Instruments & Methods in Physics Research Section a-Accelerators Spectrometers Detectors and Associated Equipment, vol. 535, no. 1-2, pp. 303-308, 2004.

[67] A. Breskin et al., "*A concise review on THGEM detectors*", Nucl. Instr. Meth. A, vol. 598, no. 1, pp. 107-111, 2009.

[68] M. Alexeev et al., "*The quest for a third generation of gaseous photon detectors for Cherenkov imaging counters*", Nucl. Instr. Meth. A, vol. 610, no. 1, pp. 174-177, 2009.

[69] R. Alon et al., "*Operation of a thick gas electron multiplier (THGEM) in Ar, Xe and Ar-Xe*", Journal of Instrumentation, vol. 3, 2008.

[70] C. Shalem et al., "*Advances in Thick GEM-like gaseous electron multipliers - Part I: atmospheric pressure operation*", Nucl. Instr. Meth. A, vol. 558, no. 2, pp. 475-489, 2006.

[71] J. Miyamoto, A. Breskin and V. Peskov, "*Gain limits of a Thick GEM in high-purity Ne, Ar and Xe*", Journal of Instrumentation, vol. 5, 2010.

[72] M. Cortesi et al., "*THGEM operation in Ne and Ne/CH4*", Journal of Instrumentation, 2009.

[73] V. Peskov et al., "*Further evaluation of a THGEM UV-photon detector for RICH - comparison with MWPC*", Journal of Instrumentation, vol. 5, 2010.

[74] F. D. Amaro et al., "*The Thick-COBRA: a new gaseous electron multiplier for radiation detectors*", Journal of Instrumentation, vol. 5, 2010.

[75] M. Li, M. S. Dixit and P. C. Johns, "*Photon-counting digital radiography using high-pressure xenon filled detectors*", Nucl. Instr. Meth. A, vol. 471, no. 1-2, pp. 215-221, 2001.

[76] S. Bachmann et al., "*High rate X-ray imaging using multi-GEM detectors with a novel readout design*", Nucl. Instr. Meth. A, vol. 478, no. 1-2, pp. 104-108, 2002.

[77] D. Pacella, R. Bellazzini and M. Finkenthal, "*Energy resolved two-dimensional soft x-ray radiography with a micropattern gas detector*", Review of Scientific Instruments, vol. 77, no. 4, 2006.

[78] A. L. M. Silva et al., "*X-ray imaging detector based on a position sensitive THCOBRA with resistive line*", Journal of Instrumentation, vol. 8, 2013.

[79] H. N. Luz, "*Development of neutron and X-ray imaging detectors based on MHSP*", PhD Thesis, Departamento de Física da Universidade de Aveiro, Aveiro, Portugal, 2009.

[80] B. Henke, E. Gullikson and J. Davis, "*X-ray interactions: photoabsorption, scattering, transmission, and reflection at E=50-30000 eV, Z=1-92*", Atomic Data and Nuclear Data Tables, vol. 54, pp. 181-342, 1993.

[81] J. Miyamoto and G. F. Knoll, "*The statistics of avalanche electrons in microstrip and micro-gap gas chambers*", Nucl. Instr. Meth. A, vol. 399, pp. 85-93, 1997.

[82] A. L. M. Silva et al., "*Characterization of an energy dispersive X-ray fluorescence imaging system based on a Micropattern Gaseous Detector*", Spectrochimica Acta Part B-Atomic Spectroscopy, vol. 66, no. 5, pp. 308-313, 2011.

[83] A. L. M. Silva, "*Aplicação de um MPGD em imagiologia por fluorescência de raios X*", MSc Thesis, Departamento de Física da Universidade de Aveiro, Aveiro, Portugal, 2009.

[84] J. F. C. A. Veloso et al., "*Energy resolved X-ray fluorescence imaging based on a micropattern gas detector*", Spectrochimica Acta Part B-Atomic Spectroscopy, vol. 65, no. 3, pp. 241-247, 2010.

[85] A. Pullia et al., "*Resistive or capacitive charge-division readout for position-sensitive detectors*", Ieee Transactions on Nuclear Science, vol. 49, no. 6, pp. 3269-3277, 2002.

[86] V. T. Jordanov and G. F. Knoll, "*Digital Synthesis of Pulse Shapes in Real-Time for High-Resolution Radiation Spectroscopy*", Nucl. Instr. Meth. A, vol. 345, no. 2, pp. 337-345, 1994.

[87] J. P. Cussonneau et al., "*2D localization using resistive strips associated to the Micromegas structure*", Nucl. Instr. Meth. A, vol. 492, no. 1-2, pp. 26-34, 2002.

[88] G. C. Smith, J. Fischer and V. Radeka, "*Photoelectron Range Limitations to the Spatial-Resolution for X-Rays in Gas Proportional Chambers*", Ieee Transactions on Nuclear Science, vol. 31, no. 1, pp. 111-115, 1984.

[89] J. Fisher, V. Radeka and G. C. Smith, "*X-ray position detection in the region of 6 μm rms with wire proportional chamber*", In *Wire Chamber Conference, Vienna, Austria, 1986*, .

[90] http://consult.cern.ch/writeup/magboltz/, S. Biagi, Degrad program. Access date: May, 2013.

[91] C. A. B. Oliveira, "*Monte Carlo study of electroluminescence in gaseous detectors*", PhD Thesis, 2011.

[92] H. Klein, H. J. Brede and B. R. L. Siebert, "*Energy and Angle Straggling Effects in a D(D,N) He-3 Neutron Source Using a Gas-Target*", Nucl. Instr. Meth. A, vol. 193, no. 3, pp. 635-644, 1982.

[93] T. Lopes et al., "*Position sensitive VUV gaseous photomultiplier based on Thick-multipliers with resistive line readout*", To be published at Journal of Instrumentation, 2013.

[94] J. R. Mallard and M. . J. Myers, "*The Performance of a Gamma Camera for the Visualization of Radioactive Isotopes in vivo*", Phys. Med. Biol., vol. 8, no. 2, pp. 165-182, 1963.

[95] R. A. Metzler and S. D., "*Analytic Determination of the Resolution-Equivalent Effective Diameter of a Pinhole Collimator*", IEEE Transactions on Medical Imaging, vol. 23, and references therein, no. 6, 2004.

[96] S. W. Smith, Special Imaging Techniques, pp. 423-499, in *The Scientist and Engineer's Guide to Digital Signal Processing*, 1999.

[97] X. H. Wang, J. L. Wu and J. B. Li, "*Simulation study of the parallax effect of gaseous detectors*", Chinese Physics C, vol. 36, no. 11, pp. 1106-1110, 2012.

[98] A. L. M. Silva et al., "*EDXRF imaging of Pb in glazed ceramics using a micropattern gas detector*", Analytical and Bioanalytical Chemistry, vol. 395, no. 7, pp. 2073-2080, 2009.

[99] A. Guilherme et al., "*Micro energy dispersive X-ray fluorescence analysis of polychrome lead-glazed Portuguese faiences*", Spectrochimica Acta Part B-Atomic Spectroscopy, vol. 65, no. 4, pp. 328-333, 2010.

[100] A. Guilherme et al., "*X-ray fluorescence (conventional and 3D) and scanning electron microscopy for the investigation of Portuguese polychrome glazed ceramics: Advances in the knowledge of the manufacturing techniques*", Spectrochimica Acta Part B-Atomic Spectroscopy, vol. 66, no. 5, pp. 297-307, 2011.

[101] A. Guilherme et al., "*Micro-XRF for characterization of Moroccan glazed ceramics and Portuguese tiles*", Journal of Instrumentation, vol. 8, no. 02, pp. C02055, 2013.

[102] A. P. Carvalho et al., "*Characterisation of ceramic pastes of Portuguese ancient tiles*", Advanced Materials Forum Iii, Pts 1 and 2, vol. 514-516, pp. 1648-1652, 2006.

[103] M. L. Carvalho et al., "*Human teeth elemental profiles measured by synchrotron x-ray fluorescence: dietary habits and environmental influence*", X-Ray Spectrometry, vol. 30, no. 3, pp. 190-193, 2001.

[104] T. Pinheiro et al., "*Microprobe analysis of teeth by synchrotron radiation: environmental contamination*", Nuclear Instruments and Methods in Physics Research Section B: Beam Interactions with Materials and Atoms, vol. 158, no. 14, pp. 393-398, 1999.

[105] M. J. Anjos et al., "*Elemental mapping of teeth using μSRXRF*", Nuclear Instruments and Methods in Physics Research Section B: Beam Interactions with Materials and Atoms, vol. 213, pp. 569-573, 2004.

[106] M. Saber-Tehrani, M. H. Givianrad and P. Kahkashan, "*Assessment of some elements in human permanent healthy teeth, their dependence on number of metallic amalgam fillings, and interelements relationships*", Biological Trace Element Research, vol. 116, no. 2, pp. 155-169, 2007.

[107] M. L. Carvalho et al., "*Analysis of human teeth and bones from the chalcolithic period by X-ray spectrometry*", Nuclear Instruments and Methods in Physics Research Section B: Beam Interactions with Materials and Atoms, vol. 168, no. 4, pp. 559-565, 2000.

[108] M. L. Carvalho et al., "*Evaluation of the diffusion of Mn, Fe, Ba and Pb in Middle Ages human teeth by synchrotron microprobe X-ray fluorescence*", Spectrochimica Acta Part B: Atomic Spectroscopy, vol. 62, no. 67, pp. 702-706, 2007.

[109] M. L. Carvalho et al., "*Hg, Bi, Cu and Zn distribution in human teeth treated by dental amalgam measured by synchrotron microprobe*", Nuclear Instruments and Methods in Physics Research Section B: Beam Interactions with Materials and Atoms, vol. 196, no. 12, pp. 148-154, 2002.

[110] M. L. Carvalho et al., "*Amalgam components drift in teeth-toxicity risks: A preliminary approach*", Nuclear Instruments and Methods in Physics Research Section B: Beam Interactions with Materials and Atoms, vol. 136138, no. 0, pp. 913-918, 1998.

[111] H. H. Harris et al., "*A link between copper and dental caries in human teeth identified by X-ray fluorescence elemental mapping*", Journal of Biological Inorganic Chemistry, vol. 13, no. 2, pp. 303-306, 2008.

[112] J. Abraham et al., "*Spectrochemical analysis of dental calculus by synchrotron radiation X-ray fluorescence*", Analytical Chemistry, vol. 74, no. 2, pp. 324-329, 2004.

[113] C. Oprea et al., "*XRF detection limits for dental tissues of human teeth*", Vacuum, vol. 83, Supplement 1, no. 0, pp. S166-S168, 2009.

[114] A. F. Marques et al., "*X-ray microprobe synchroton radiation X-ray fluorescence application on human teeth of renal insufficiency patients*", Spectrochimica Acta Part B: Atomic Spectroscopy, vol. 59, no. 1011, pp. 1675-1680, 2004.

[115] A. L. M. Silva et al., "*Performance of a gaseous detector based energy dispersive X-ray fluorescence imaging system: Analysis of human teeth treated with dental amalgam*", Spectrochimica Acta Part B: Atomic Spectroscopy, 2013.

[116] J. Abraham et al., "*Spectrochemical analysis of dental calculus by synchrotron radiation X-ray fluorescence*", Anal. Chem., vol. 74, pp. 324-329, 2002.

[117] G. Van Der Snickt et al., "*μ-XRF/μ-RS vs. SR μ-XRD for pigment identification in illuminated manuscripts*", Applied Physics a-Materials Science and Processing, vol. 92, no. 1, pp. 59-68, 2008.

[118] S. Pessanha, M. Manso and M. L. Carvalho, "*Application of spectroscopic techniques to the study of illuminated manuscripts: A survey*", Spectrochimica Acta Part B: Atomic Spectroscopy, vol. 7172, no. 0, pp. 54-61, 2012.

[119] A. Duran et al., "*Characterization of illuminated manuscripts by laboratory-made portable XRD and micro-XRD systems*", Analytical and Bioanalytical Chemistry, vol. 395, no. 7, pp. 1997-2004, 2009.